

CORE- TO LOG-SCALE ANALYSIS OF THE WOLFCAMP FORMATION IN THE
THUNDER C20-13 #2H CORE, DELAWARE BASIN, REEVES COUNTY, TEXAS

by

Sywei Vicky Yeap

A thesis submitted to the Faculty and the Board of Trustees of the Colorado School of Mines in partial fulfillment of the requirements for the degree of Master of Science (Geology).

Golden, Colorado

Date _____

Signed: _____
Sywei Vicky Yeap

Signed: _____
Dr. Stephen A. Sonnenberg
Thesis Advisor

Golden, Colorado

Date _____

Signed: _____
Dr. Wendy Bohrson
Professor and Department Head
Department of Geology and Geological Engineering

ABSTRACT

The Pennsylvanian-Permian Wolfcamp Formation of the Permian Basin in West Texas and New Mexico is currently one of the most pursued unconventional plays in the world. In most areas, the Wolfcamp is over 2,000 ft thick and contains multiple stacked pay intervals. A 2018 United States Geological Survey (USGS) assessment evaluated the potential of technically recoverable and undiscovered resources of the Wolfcamp Formation in the Delaware Basin to contain 29,476 MMbbl of oil, 220,824 Bscf of gas, and 14,907 MMbbl of natural gas liquids (NGLs). The vast opportunities available have sparked interest in understanding the complexity and heterogeneity of the Wolfcamp strata to their implications on reservoir performance.

The Wolfcamp Formation records deepwater deposition of organic-rich mudstones interbedded with calcareous mudstones, calcareous siltstones, carbonates, and argillaceous mudstones that were deposited within mixed carbonate-siliciclastic fan systems. These fan systems resided in a semi-restricted basin with sediment originating from multiple sources. The Wolfcamp Formation is informally subdivided into four intervals, from youngest to oldest, as Wolfcamp A, B, C, and D. Understanding the geological processes and characteristics that comprise each member is critical for exploration and in selecting the best landing zones. The Wolfcamp Formation is comprised of mass movement and sediment gravity flow deposits separated by background hemipelagic sedimentation. While the Wolfcamp Formation has been widely correlated using wireline logs, Wolfcamp event beds and the facies that make up these event beds are often below log resolution.

The objective of this study involves using core, core associated data, and well logs sourced from the Wolfcamp play to investigate the vertical variability seen in the Wolfcamp intervals. The dataset used in this study is from the Cimarex Energy Thunder C20-13 #2H well located in Reeves County, Texas. The total length of the core used is 738.4 ft and includes the following: Wolfcamp A (215.5 ft), Wolfcamp B (175.9 ft), Wolfcamp C (310.3 ft), and Wolfcamp D (36.7 ft). Integration of detailed core description, X-ray Diffraction (XRD), X-ray Fluorescence (XRF), Routine Core Analysis (RCA),

Source Rock Analysis (SRA), geomechanical analysis, and well logs were used in this study to identify facies, facies characteristics, and associated reservoir properties.

Four facies groups and nine lithofacies were identified based on mineral composition, grain size, grain shape, sorting, color, and sedimentary structures. From these facies, porosity ranges from 4.5 to 12.1 percent and permeability from 0.1 to 340.0 nD. Total organic carbon (TOC) was observed to be highest in siliceous mudstones, with TOC up to 6.3 wt.%. Unconfined compressive strength (UCS), a method to assess rock strength from core, was measured using an Equotip Bambino micro-rebound hammer. Carbonate-rich lithofacies were found to have higher rock strength compared to clay-rich facies. The skeletal packstone has the highest average rock strength of 65 MPa. The lowest rock strength was observed in the argillaceous mudstone with an average UCS of 45 MPa. The distribution of Wolfcamp lithofacies is highly stratified. However, cyclicity is seen in both carbonate and siliciclastic event beds. Each event bed ranges from less than an inch to tens of feet in total thickness. Source rock analysis was used to examine the quantity of organic matter, hydrocarbon generative potential, the extent of thermal maturity, and kerogen type. The reservoir properties of each lithofacies were evaluated to identify reservoir prone and nonreservoir prone facies. Detailed core analyses were compared to a normal log suite to determine the controls of rock and fluid properties on well log responses.

TABLE OF CONTENTS

ABSTRACT	ii
LIST OF FIGURES	vii
LIST OF TABLES	xvii
ACKNOWLEDGEMENTS	xviii
CHAPTER 1: INTRODUCTION	1
1.1 Background	1
1.2 Research Objective, Dataset, and Methods	6
1.3 Regional Setting	11
1.4 Previous Work.....	17
CHAPTER 2: CORE ANALYSIS	20
2.1 Compositional Analysis.....	21
2.2 Lithofacies	24
2.2.1 Siliceous Mudstone.....	25
2.2.2 Bioturbated Siliceous Mudstone.....	30
2.2.3 Carbonate-rich Siliceous Mudstone.....	31
2.2.4 Mixed Calcareous Silty Mudstone.....	32
2.2.5 Calcareous Siltstone.....	32
2.2.6 Skeletal Packstone	33
2.2.7 Dolostone	34
2.2.8 Wackestone.....	34
2.2.9 Argillaceous Mudstone	35
2.3 Facies Distribution	35
2.3.1 Wolfcamp A	37
2.3.2 Wolfcamp B.....	39

2.3.3	Wolfcamp C	41
2.3.4	Wolfcamp D	43
2.4	Depositional Processes	45
2.4.1	Hemipelagic/Background Sedimentation	46
2.4.2	Debris Flows	48
2.4.3	Hybrid Event Beds (HEBs)	50
2.4.4	Fine-grained, Low-density Turbidity Flows	53
CHAPTER 3: ELEMENTAL GEOCHEMISTRY		55
3.1	Mineral Model	55
3.2	Principal Component Analysis (PCA)	59
3.3	Chemofacies	61
3.4	Synthetic Gamma Ray	63
3.5	Terrestrial (Detrital) Indicators	66
3.6	Carbonate Indicators	72
3.7	Redox-Sensitive Trace Elements	76
CHAPTER 4: RESERVOIR CHARACTERIZATION		82
4.1	Source Rock Analysis	82
4.1.1	Quantity of Organic Matter	85
4.1.2	Kerogen Type and Thermal Maturity	90
4.2	Geomechanics	93
4.2.1	Unconfined Compressive Strength (UCS)	94
4.2.2	Brittleness	102
4.2.3	Natural Fractures	103
4.3	Reservoir Properties (Porosity, Permeability, and Fluid Saturations)	106
4.4	Reservoir and Nonreservoir Rocks	108

4.5	Core Analyses to Log Scale	109
4.5.1	Wolfcamp A	113
4.5.2	Wolfcamp B.....	118
4.5.3	Wolfcamp C.....	120
4.5.4	Wolfcamp D	122
CHAPTER 5: CONCLUSIONS AND RECOMMENDATIONS		124
5.1	Conclusions	124
5.2	Recommendations	126
REFERENCES		128
APPENDIX		138

LIST OF FIGURES

Figure 1.1	Map showing the extent of Wolfcamp Assessment Units (AUs) in the Delaware Basin. The star shows the approximate location of the core used in this study (Modified from Gaswirth et al., 2018).....	3
Figure 1.2	Permian Basin major structural components with the yellow star showing the location of the core used in this study (Based on Silver and Todd, 1969; Ruppel and Ward, 2013).....	4
Figure 1.3	Regional cross section (top) and stratigraphic column (bottom) of the greater Permian Basin showing the Wolfcamp in the deeper Delaware Basin to the west and Midland Basin to the east separated by the Central Basin Platform (Engle et al., 2016 modified from Matchus and Jones, 1984; U.S. Energy Information Administration, 2018).....	5
Figure 1.4	Well log of the Cimarex Energy Thunder C20-13 #2H pilot (left) with cored interval shown in the pink rectangles. A summary of the dataset used to meet research objectives (right) includes core, core associated data, and well logs.....	7
Figure 1.5	Blakey palaeogeographical maps modified from the Colorado Plateau Geosystems, Inc. (2019) for the time of Wolfcamp deposition. The two time sequences shown are (A) Early Wolfcampian 295 Ma, and (B) Late Wolfcampian time 285 Ma. The yellow star shows the approximate location of the well used in this study.....	16
Figure 2.1	Mineral compositions from X-ray Diffraction (XRD) analyzed for Wolfcamp A, B, C, and D. Tectosilicates, such as quartz, potassium feldspars, and plagioclase, are shown in yellow, orange, and red. Carbonate minerals, primarily calcite and dolomite, are shown in blue. Clays are shown in brown and gray. Chlorite is abundant locally in Wolfcamp B, C, and D.....	22
Figure 2.2	Scatter plots of elemental XRF data versus mineralogical data from XRD for 22 samples from the Thunder C20-13#2H Core. The dashed line represents the best fit linear trendline.....	23

Figure 2.3	Ternary diagram with end members of the three key mineral groups—quartz, feldspars, and micas (QFM), carbonates (CARB), and clays. Samples with XRD (n=67) are first used to define facies groups based on mineral components, then subdivided into lithofacies based on elements captured from core description.....	26
Figure 2.4	Summary of the Argillaceous Facies Group and Siliceous Facies Group lithofacies. The Argillaceous Facies Group consists of the Argillaceous Mudstone. The Siliceous Facies Group includes the Siliceous Mudstone, Bioturbated Siliceous Mudstone, and Carbonate-rich Siliceous Mudstone. For each lithofacies, the top section consists of two core images and average reservoir properties, including total organic carbon (TOC), porosity, and permeability. The bottom consists of X-ray Diffraction (XRD) compositional data. The pie chart shows the average weight percentages of QFM (yellow), clays (brown), carbonates (blue), and other minerals (gray). The call-out boxes show average mineral constituents for each mineral group.....	27
Figure 2.5	Summary of the Mixed Facies Group and Calcareous Facies Group lithofacies. The Mixed Facies Group consists of the Mixed Calcareous Silty Mudstone. The Calcareous Facies Group includes the Calcareous Siltstone, Dolostone, Skeletal Packstone, and Wackestone. For each lithofacies, the top section consists of two core images and average reservoir properties, including total organic carbon (TOC), porosity, and permeability. The bottom consists of X-ray Diffraction (XRD) compositional data. The pie chart shows the average weight percentages of QFM (yellow), clays (brown), carbonates (blue), and other minerals (gray). The call-out boxes show average mineral constituents for each mineral group.....	28
Figure 2.6	Facies distribution for the cored intervals of Wolfcamp A, B, C, and D. On the left, a normal well log suite of the Thunder C20-13 #2H is shown with the cored intervals noted as (1) and (2) in the pink rectangles. Facies distribution is shown to the right showing core depth, facies group, and lithofacies.....	36

- Figure 2.7 Wolfcamp A facies distribution and example of cored interval
Spanning 20 ft. The core depth, facies group, and lithofacies can be found on the left. The blue box is the cored example shown. Wolfcamp A is composed of the calcareous, siliceous, and mixed facies groups. Lithofacies associated Wolfcamp A are primarily the result of carbonate sediment gravity flows, predominantly hybrid event beds (HEBs). An example of one HEB deposit seen in the red arrow. The base of the HEB is a packstone bed (coarsest grain size, highest carbonate content) that fines upwards to a calcareous siltstone, mixed calcareous silty mudstone, and carbonate-rich siliceous mudstone. Wolfcamp A shows cyclic stacking of these fining upward sequences.....38
- Figure 2.8 Wolfcamp B facies distribution and example of cored interval spanning 20 ft. The core depth, facies group, and lithofacies can be found on the left. Pie charts of the facies group and lithofacies distributions are seen below. The red box is the cored example shown. An example of one carbonate sediment gravity flow deposit is shown in the red arrow. The yellow arrows represent individual fine-grained turbidites associated with the argillaceous mudstone lithofacies. The brown star shows RCA location for argillaceous mudstone at 11,118 ft (LECO TOC 0.81 wt.%, porosity 10.0%, permeability 1.63 nD, and water saturation 74.9%). The yellow star shows RCA location for siliceous mudstone at 11,131 ft (LECO TOC 2.33 wt.%, porosity 9.3%, permeability 52.5 nD, and water saturation 55.5%).....40
- Figure 2.9 Wolfcamp C facies distribution and examples of core from Upper Wolfcamp C and Lower Wolfcamp C, spanning 10 ft each. The core depth, facies group, and lithofacies can be found on the left. An example of one carbonate sediment gravity flow deposit is shown in the red arrow from the Lower Wolfcamp C. The yellow arrows represent individual fine-grained turbidites associated with the argillaceous mudstone lithofacies from Upper Wolfcamp C. The brown star shows RCA location for argillaceous mudstone at 11,440.5 ft (LECO TOC 0.16 wt.%, porosity 11.5%, permeability 0.7 nD, and water saturation 86.4%). The yellow star shows RCA location for carbonate-rich siliceous mudstone at 11,665 ft (LECO TOC 2.15 wt.%, porosity 7.9%, permeability 71.9 nD, and water saturation 32.6%).....42

Figure 2.10	Wolfcamp D facies distribution and example of two cored intervals, spanning 10 ft each. The core depth, facies group, and lithofacies can be found on the left. The top 36.7 ft of Wolfcamp D was cored and examined for this study. The Wolfcamp D cored interval shows both siliciclastic- and carbonate-dominated lithofacies.....	44
Figure 2.11	Core photo illustrating a hemipelagic facies association illustrating facies stacking pattern of a bioturbated siliceous mudstone with an overlying siliceous mudstone from 10,906 ft. The bioturbated mudstone marks the end of an underlying sediment gravity flow event into a period of lower energy, slow sediment accumulation rate.....	47
Figure 2.12	Core photo of a debris flow deposit from 11,578 ft illustrating key architectural elements including (1) sharp basal contact, (2) chaotically arranged intraclasts, (3) subangular, poorly sorted grains, and (4) clast protrusion. The dark gray mudstone that overlies the debrite is interpreted to be the equivalent of a Te bed, likely background sedimentation or sediment from a distant, waning flow.....	49
Figure 2.13	Idealized Wolfcamp hybrid event bed (Kvale et al., 2020).....	51
Figure 2.14	Core photo (from 10,896 to 10,900 ft) with annotations for a single flow, fining upwards hybrid event bed (HEB) deposit. Illustrated are the lithofacies and corresponding HEB division based on the HEB components described by Kvale and others (2020).....	52
Figure 2.15	Core photo (from 11,450 to 11,451 ft) showing cyclic, low-density turbidite deposits. The enlarged core photo to the right shows a single fine-grained, low-density, turbidite deposit. The basal Tc is a ripple laminated fine-grained siltstone. The Td bed is a laminated to massive argillaceous mudstone. The Te division is the mud cap comprised of a massive, siliceous mudstone. Mud caps are very thin, often 0.04 inches (1 mm) or less.....	54
Figure 3.1	Lithology logs showing (1) facies group from core description, (2) lithofacies from core description, (3) XRD normalized abundances of total QFM, carbonates (CARB), and clays (CLY), and (4) XRF mineral model calculated abundances for normalized quartz (Qtz), calcite (CAL), and illite (I).....	58

Figure 3.2	Principal component analysis (PCA) for the Wolfcamp A elemental dataset from XRF showing interpreted clusters of elements in circles.....	60
Figure 3.3	Principal component analysis (PCA) for the Wolfcamp B elemental dataset from XRF showing interpreted clusters of elements in circles.....	61
Figure 3.4	Bar graphs showing four chemofacies defined based on elemental signatures of enrichments and depletions. Elemental enrichments are shown in green and depletions in red.....	62
Figure 3.5	Comparison between wireline log gamma ray (GR) to core-derived synthetic gamma ray (GRsyn) calculated from XRF data. Wireline logs seen to the left show the following tracks (1) total GR, (2) resistivity curves, (3) porosity curves, and (4) photoelectric factor (PEF). Core-derived curves are seen to the right, showing the following tracks: (1) GRsyn, (2) XRF thorium concentration, (3) XRF uranium concentration, (4) XRF potassium concentration, and (5) lithofacies from core description. The red arrow indicates the location of the up-close example seen in Figure 3.6.....	65
Figure 3.6	Comparison between wireline log gamma ray (GR) and core-derived synthetic GR (GRsyn) for an eight-foot section with the associated core interval. Wireline captures the overall change in lithology and thick beds. For thin carbonate beds (indicated by the black arrow), wireline captures the signal but the signal is not fully developed.....	66
Figure 3.7	Figure 3.7—Crossplots of terrigenous influx proxies vs. aluminum (Al). Positive trends were observed in elements K, Rb, Ti, Zr, and Cr, suggesting that these elements are associated with terrestrial (detrital) input.....	68

Figure 3.8	Crossplot of Al vs. Si to investigate the origin of silica in the Wolfcamp A and B. A positive trend indicates silica is detrital in origin. A negative trend, or deviation from the positive trend, suggests authigenic or biogenic influences. The crossplots include A) Si vs. Al for Wolfcamp A. B) Si vs. Al for Wolfcamp B. C) Si vs. Al for both Wolfcamp A (blue) and Wolfcamp B (red). D) Si vs. Al by chemofacies. Chemofacies 1 shown in blue ($R^2=0.31$, positive trend), Chemofacies 2 in light blue ($R^2=0.32$, positive trend), Chemofacies 3 in yellow ($R^2=0.01$, no trend), and Chemofacies 4 in green ($R^2=0.27$, negative trend).....	70
Figure 3.9	Elemental profiles for terrestrial indicators. Track 1: GRsyn. Track 2 through 8 show terrestrial indicators, from left to right, silicon (Si), aluminum (Al), potassium (K), rubidium (Rb), zirconium (Zr), titanium (Ti), and chromium (Cr). Track 9: lithofacies from core description. Track 10: chemofacies from cluster analysis.....	71
Figure 3.10	Elemental profiles for carbonate indicators. Track 1: GRsyn. Track 2 through 4 show carbonate indicators, from left to right, calcium (Ca), strontium (Sr), and magnesium (Mg). Track 5: lithofacies from core description. Track 6: chemofacies from cluster analysis.....	73
Figure 3.11	Crossplots of Ca vs. Al to determine the origin of Ca. A) Ca vs. Al for Wolfcamp A (blue) and Wolfcamp B (red). B) Ca vs. Al by chemofacies with Chemofacies 1 (blue), Chemofacies 2 (light blue), Chemofacies 3 (yellow), and Chemofacies 4 (green). The overall negative trend implies Ca does not have a detrital source and is either biogenic or authigenic in origin.....	74
Figure 3.12	Crossplot of Ca vs. Sr for Wolfcamp A (blue) and Wolfcamp B (red). A strong positive correlation is seen in both Wolfcamp intervals.....	74
Figure 3.13	Crossplot of Ca vs. Mg showing A) Ca vs. Mg for Wolfcamp A (blue) and Wolfcamp B (red). B) Ca vs. Mg by chemofacies with Chemofacies 1 (blue), Chemofacies 2 (light blue), Chemofacies 3 (yellow), and Chemofacies 4 (green).....	75

Figure 3.14	Crossplots of redox-sensitive trace elements vs. core TOC. The strongest relationship to TOC was seen for the element Ni ($R^2=0.79$). Moderate correlations were observed for U ($R^2=0.40$), Cu ($R^2=0.35$), and Mo ($R^2=0.28$). Low correlations were established for S ($R^2=0.18$), As ($R^2=0.16$), Fe ($R^2=0.10$), and Zn ($R^2=0.01$).....	77
Figure 3.15	Calculated TOC from redox-sensitive elements that have strong to moderate correlations to core-measured TOC. Track 1: GRsyn. Track 2 through 5 show calculated TOC curves, from left to right, TOC_{Ni} , TOC_U , TOC_{Cu} , and TOC_{Mo} . Red dots indicate LECO TOC from core analysis. Track 6: lithofacies from core description. Track 7: chemofacies from cluster analysis.....	78
Figure 3.16	Elemental profiles of paleoredox-sensitive indicators. Track 1: GRsyn. Track 2 through 11 show paleoredox-sensitive indicators, from left to right, molybdenum (Mo), uranium (U), chromium (Cr), zirconium (Zr), arsenic (As), niobium (Nb), sulfur (S), iron (Fe), nickel (Ni), and copper (Cu). Track 12: TOC calculated from Ni $R^2=0.79$. Red dots indicate LECO TOC from core analysis. Track 13: lithofacies from core description. Track 14: chemofacies from cluster analysis. The red and orange arrows show examples of core associated with elevated paleoredox-sensitive elements seen in Figure 3.17.....	80
Figure 3.17	Core locations with high enrichments in paleoredox-sensitive elements found associated with the Siliceous Mudstone lithofacies. The core depths are indicated in arrows in Figure 3.16.....	81
Figure 4.1	Source Rock Analysis (SRA) data for the Wolfcamp A, B, C, and D. TOC classification based on Law (1999) proposed for assessing source rock generative potential. Jarvie and others (2001) classification used for thermal maturity indicators Tmax and Ro.....	84
Figure 4.2	Crossplots investigating the relationship between LECO TOC from core vs. wireline GR. A) Total GR vs. TOC. B) Spectral GR from potassium (K) vs. TOC. C) Spectral GR from thorium (Th) vs. TOC. D) Spectral GR from uranium (U) vs. TOC.....	86

Figure 4.3	Indirect methods to approximate TOC on log-scale using spectral gamma ray from uranium (SGRU). Track 1: GRKT and GR, shaded in orange, is the contribution of uranium to total GR as a proxy for TOC. Track 2: resistivity curves. Track 3: porosity curves. Track 4: photoelectric factor (PEF). Track 5: TOC_{SGRU} calculated from the equation derived from $SGRU$ to core TOC (Fig. 4.2.D).....	87
Figure 4.4	Crossplot of S2 vs. TOC showing that most siliceous mudstone, carbonate-rich siliceous mudstone, and mixed calcareous silty mudstone lithofacies have TOC values ranging from good to excellent. Calcareous siltstone, dolostone, bioturbated siliceous mudstone, and argillaceous mudstone are more organic-lean facies with TOC that ranked poor to fair. Most samples show poor hydrocarbon generating potential. Classification for TOC is based on Law (1999) proposed for assessing source rocks. Classification for hydrocarbon generating potential after Dembicki (2009).....	89
Figure 4.5	Modified van Krevelen diagram for hydrogen index (HI) vs. oxygen index (OI) showing the evolution pathways by kerogen type.....	91
Figure 4.6	Crossplot of HI vs. Tmax showing that most SRA samples from the Thunder C20-13 #2H fall within the condensate wet gas window. Looking at the Delaware Basin gas-oil ratio (GOR) trend (modified from Mancos and Perez, 2018), the Thunder is situated in the middle of the condensate gas trend.....	92
Figure 4.7	Calculated values for unconfined compressive strength (UCS in MPa) shown throughout a 10 ft core section with corresponding lithofacies. The red arrow indicates a single hybrid event bed (HEB) deposit showing decreasing rock strength as the HEB deposit fines upwards.....	98
Figure 4.8	Box diagram of calculated unconfined compressive strength (UCS) based on lithofacies. Rock strength is highest in carbonate-dominated lithofacies and lowest in clay-dominated lithofacies.....	99

Figure 4.9	Unconfined compressive strength (UCS) calculated from core displayed stratigraphically as a function of depth for the Wolfcamp A, B, C, and D. UCS track ranges from 30 to 70 MPa. UCS curve is colored based on associated lithofacies from core description. The enlarged section from the Wolfcamp D shows subtle facies changes with contrasting high and low rock strength.....	101
Figure 4.10	Crossplots of calculated mineral-based brittleness index (MBI) as a function of composition (clays, carbonates, and QFM).....	103
Figure 4.11	Types of natural fractures and microfaults observed in Wolfcamp core. A) vertical fracture through calcareous siltstone and mudstone facies, terminating at the base of a bed (top) and within a bed (bottom). B) Microfaults (shown in red), primarily found associated with the argillaceous mudstone. C) Horizontal “beef” fracture found in siliceous mudstone; small vertical fracture can be seen potentially propagating from beef fracture. D) Quartz-filled fracture in thin section from the siliceous mudstone (Wolfcamp) in Ward County.....	105
Figure 4.12	Summary of the average reservoir properties for the Wolfcamp lithofacies and interpreted reservoir/nonreservoir designation.....	108
Figure 4.13	Integrated core analyses (including core description, XRD, XRF, RCA, UCS, and reservoir/nonreservoir designation) to associated well log curves for the Wolfcamp A and B.....	114
Figure 4.14	Integrated core analyses (including core description, XRD, RCA, UCS, and reservoir/nonreservoir designation) to associated well log curves for the Wolfcamp C and D.....	115
Figure 4.15	Figure 4.15—Pie chart of reservoir vs. nonreservoir prone rocks based on reservoir properties for the Wolfcamp A cored interval. The Wolfcamp A is comprised of 61.3% reservoir prone rock. Nonreservoir prone rock only includes nonreservoir (carbonate) rocks that represent 38.7% of the interval.....	117

- Figure 4.16 Pie chart of reservoir vs. nonreservoir prone rocks based on reservoir properties for the Wolfcamp B cored interval. The Wolfcamp B is comprised of 68.4% reservoir prone rock. Nonreservoir prone rocks encountered in the Wolfcamp B include nonreservoir (argillaceous) and nonreservoir (carbonate) rocks.....119
- Figure 4.17 Pie charts of reservoir vs. nonreservoir prone rocks based on reservoir properties for the Upper Wolfcamp C and Lower Wolfcamp C cored interval. The Upper Wolfcamp C is composed of 36.7% reservoir prone rock. Primary nonreservoir rock in the Upper Wolfcamp C is nonreservoir (argillaceous) that makes up 52.5% of the cored interval. Nonreservoir (carbonate) rocks represent 10.8% of the interval. Reservoir potential is more favorable in the Lower Wolfcamp C. The Lower Wolfcamp C is comprised of 75.9% reservoir rock. Nonreservoir rock makes up 24% of the Lower Wolfcamp C. The primary type of nonreservoir rock in the Lower Wolfcamp C are carbonates that make up 21.3% of the Wolfcamp C.....122

LIST OF TABLES

Table 1.1 Total undiscovered resources for the six continuous Assessment Units (AUs) of the Wolfcamp Formation in the Delaware Basin, Permian Basin Province, New Mexico, and Texas (Modified from Gaswirth et al., 2018).....2

Table 4.1 Example calculation illustrating the workflow to calculate UCS. For each depth, 10 measurements taken with an Equotip Bambino micro-rebound hammer are recorded in Leeb Hardness (HLD). From the trimmed dataset (taking out the minimum and maximum values), the trimmed mean is used to calculate UCS (psi and MPa).....97

Table 4.2 Values for unconfined compressive strength (UCS) from core based on lithofacies.....100

Table 4.3 Average mineral constituents and reservoir properties for the Wolfcamp lithofacies analyzed from X-ray Diffraction (XRD) and Routine Core Analysis (RCA).....107

ACKNOWLEDGEMENTS

I am truly, very grateful to the people who have helped play a role in the completion of this thesis. I would first like to thank my advisor, Dr. Steve Sonnenberg. Thank you for showing your passion for petroleum geology that has instilled in me my own. You are an inspiration to me and many of your students. You have been an integral part of why this is “our favorite school.” Thank you to my committee members, Dr. Donna Anderson and Dr. Marsha French, for being wonderful professors and guiding me through my research. Thank you for taking the time to review my work, writing, and presentations along the way.

I would like to thank Cimarex Energy for providing this robust dataset that has made this entire project possible. In particular, I would like to thank Dr. Mark Sonnenfeld, Mark Holland, Dave Witter, Tom Jorden, Mark Hanson, Kathy McDonald, Jason McClain, Tiffany Hopkins, Jason Asmus, Doug Klepacki, Emily Swanson, Rick Willis, and others. There are many at Cimarex who have challenged and taught me to be a better geologist. Thank you to those at Core Laboratories (Denver) for allowing me to use your facilities to view the Thunder C20-13 #2H core.

Of course, I cannot forget the friends and faculty from the Mudrocks and Tight Oil Characterization (MUDTOC) Consortium, the Colorado School of Mines Geology Department, and the AAPG student chapter. What a great group of people and memorable times at Berthoud Hall (and our secondary office at GCB).

A special thank you to Jeffery Kok, Ian Johnson, Tracy Mosness, Wing On Chu (Bsc. Geological Engineering '70), and Jason Pinto (Bsc. Petroleum Engineering '96) who have been role models that I have looked up to in the industry and beyond. Thank you always.

Last, but definitely not least—words cannot express how grateful I am for my family. My parents, Teong Khoon Yeap and Kim Kee Cheah, thank you for your unwavering love, encouragement, and support. My brother, Jher Qin Yeap, who sends me food from halfway around the world while I work on writing this thesis. I am so, so blessed. Reggie Vair, not sure you will read this, but I am very grateful for you and always will be. Thank you for your love and support through this chapter and I am excited for our next one together.

CHAPTER 1: INTRODUCTION

1.1 Background

The Permian Basin is one of the oldest and most well-known hydrocarbon producing regions in the world. The discovery well that sparked interest in oil and gas for the Permian Basin was the Santa Rita #1, completed on May 27, 1923, that produced 100 to 150 bbl/day (Dancy, 2018). Exploration efforts and production have proceeded since then. Early production in the Permian focused on conventional, shallow, vertical wells targeting the Grayburg, San Andreas, and Clear Fork on the Central Basin Platform. During this time, Permian Basin production accounted for 10 to 20 percent of oil and gas production in the United States (Enverus, 2020). Peak production in the Permian first occurred in the early 1970s. It declined steadily for several decades until advancements in horizontal drilling, hydraulic fracturing, and better completion methods were introduced during the late 2000s. Hydraulic fracturing was first implemented in conventional resource plays to increase recovery factors and improve well performance. Subsequent breakthroughs in hydraulic fracturing were used in unconventional plays that began with the Barnett Shale. Advancements in technology allowed operators to produce from previously unattainable resources in organic-rich, low permeability mudrocks. By the early 2010s, the “Shale Revolution” brought record oil and gas production to the Permian Basin once again (Sieminski, 2014).

Today, the Permian Basin of West Texas and southeast New Mexico is the largest oil and gas producing basin in North America and the second-largest in the world. As of January 2021, the Permian Basin produces 4.3 MMbbl/day and 16,365 MMscf/day of oil and gas, respectively. Production is estimated to increase to 5.4 MMbbl/day by 2023 (EIA, 2021). A significant portion of production today comes from alternating siliciclastic and carbonate beds from Permian Leonardian and Wolfcampian strata in the Delaware Basin (Kvale et al., 2020). In 2018, the United States Geological Survey (USGS) investigated the undiscovered continuous resource potential for the Wolfcamp Formation in the Delaware Basin. The assessment divided the Wolfcamp into six continuous assessment units (AU’s) of Wolfcamp A (Oil), Wolfcamp B Upper (Oil), Wolfcamp B Lower (Oil), Wolfcamp C

(Oil), Wolfcamp C (Gas), and Wolfcamp D (Gas) as seen in Figure 1.1. The mean of the total undiscovered resources for the mentioned assessment units are 29,476 MMbbl of oil, 220,824 Bscf of gas, and 14,907 MMbbl of NGL’s remaining, as seen in Table 1.1.

Table 1.1—Total undiscovered resources for the six continuous Assessment Units (AUs) of the Wolfcamp Formation in the Delaware Basin, Permian Basin Province, New Mexico and Texas (Modified from Gaswirth et al., 2018).

Total Petroleum System and Assessment Units	Accumulation Type	Total Undiscovered Resources											
		Oil (MMbbl)				Gas (Bscf)				NGL (MMbbl)			
		F95	F50	F5	Mean	F95	F50	F5	Mean	F95	F50	F5	Mean
Delaware Basin Wolfcamp D Continuous Gas AU	Gas					22,718	72,821	124,966	72,920	850	2,794	5,405	2,917
Delaware Basin Wolfcamp C Continuous Gas AU	Gas					11,757	37,793	67,845	38,510	438	1,455	2,924	1,539
Delaware Basin Wolfcamp C Continuous Oil AU	Oil	382	1,467	3,477	1,635	5,585	21,685	54,927	24,486	404	1,667	4,517	1,961
Delaware Basin Wolfcamp B Lower Continuous Oil AU	Oil	2,642	5,297	8,838	5,458	9,519	20,616	38,280	21,815	869	2,011	4,078	2,181
Delaware Basin Wolfcamp B Upper Continuous Oil AU	Oil	4,606	8,861	14,657	9,154	16,524	34,608	63,189	36,601	1,486	3,382	6,799	3,661
Delaware Basin Wolfcamp A Continuous Oil AU	Oil	8,406	12,791	19,556	13,229	14,297	25,219	42,988	26,492	1,259	2,476	4,626	2,648
Total Undiscovered Continuous Resources		16,036	28,416	26,973	29,476	80,400	212,742	390,195	220,824	5,306	13,785	28,349	14,907

The Permian Basin (Fig. 1.2) is an asymmetrical foreland basin containing subbasins that are separated by intraforeland uplifts (Yang and Dorobek, 1995). The greater Permian Basin extends over an area of approximately 82,000 square miles (Robinson, 1988; Schenk, 2007). The cross section view of the Permian Basin (Fig. 1.3) shows the deeper Delaware Basin to the west and the shallower Midland Basin to the east. The Midland and Delaware subbasins are separated by the uplifted Central Basin Platform. The Delaware Basin is the western subbasin of the Permian Basin covering an area of around 15,000 square miles and is filled to a maximum depth of 24,000 ft with Phanerozoic sedimentary rocks (Adams, 1965; Hills, 1984). It includes Culberson, Reeves, Loving, and Ward counties in Texas and Eddy and Lea counties in New Mexico. The Delaware Basin is bounded by the Matador Uplift to the north, the Marathon-Ouachita Fold Belt to the south, Bend Arch to the east, and the Diablo Platform to the west. It is connected to the Midland Basin to the east by the San Simon Channel to the north and Sheffield Channels to the south (Hennenfent et al., 2015; Kvale and Rahman, 2016). The subbasin dips towards the Central Basin Platform as a result of post-depositional structural deformation. The Delaware Basin is deepest in the east and shallows to the west. The primary unconventional targets in the Delaware Basin are the organic-rich intervals within the Wolfcamp and Bone Spring formations.

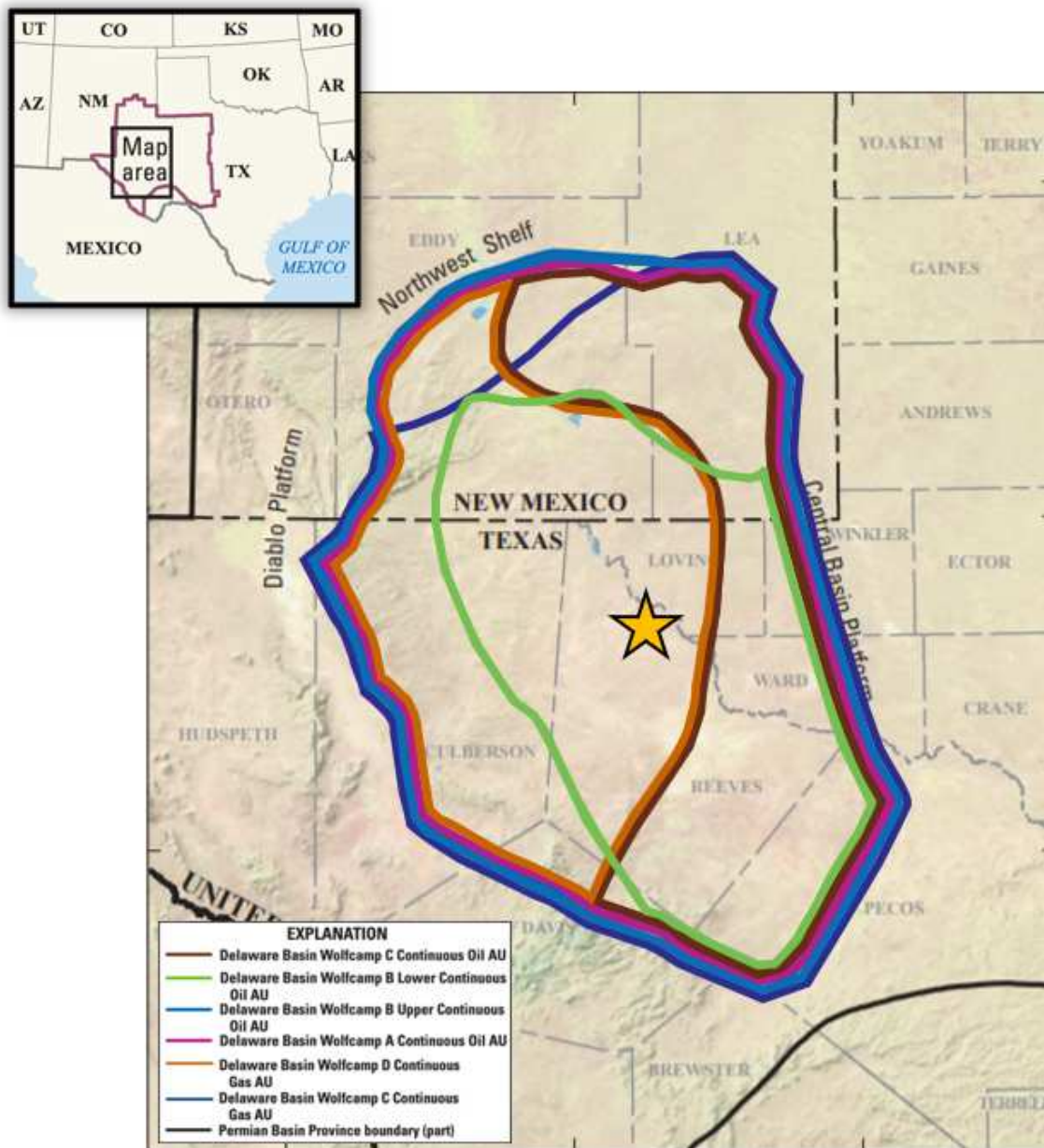


Figure 1.1—Map showing the extent of Wolfcamp Assessment Units (AUs) in the Delaware Basin. The star shows the approximate location of the core used in this study (Modified from Gaswirth et al., 2018).

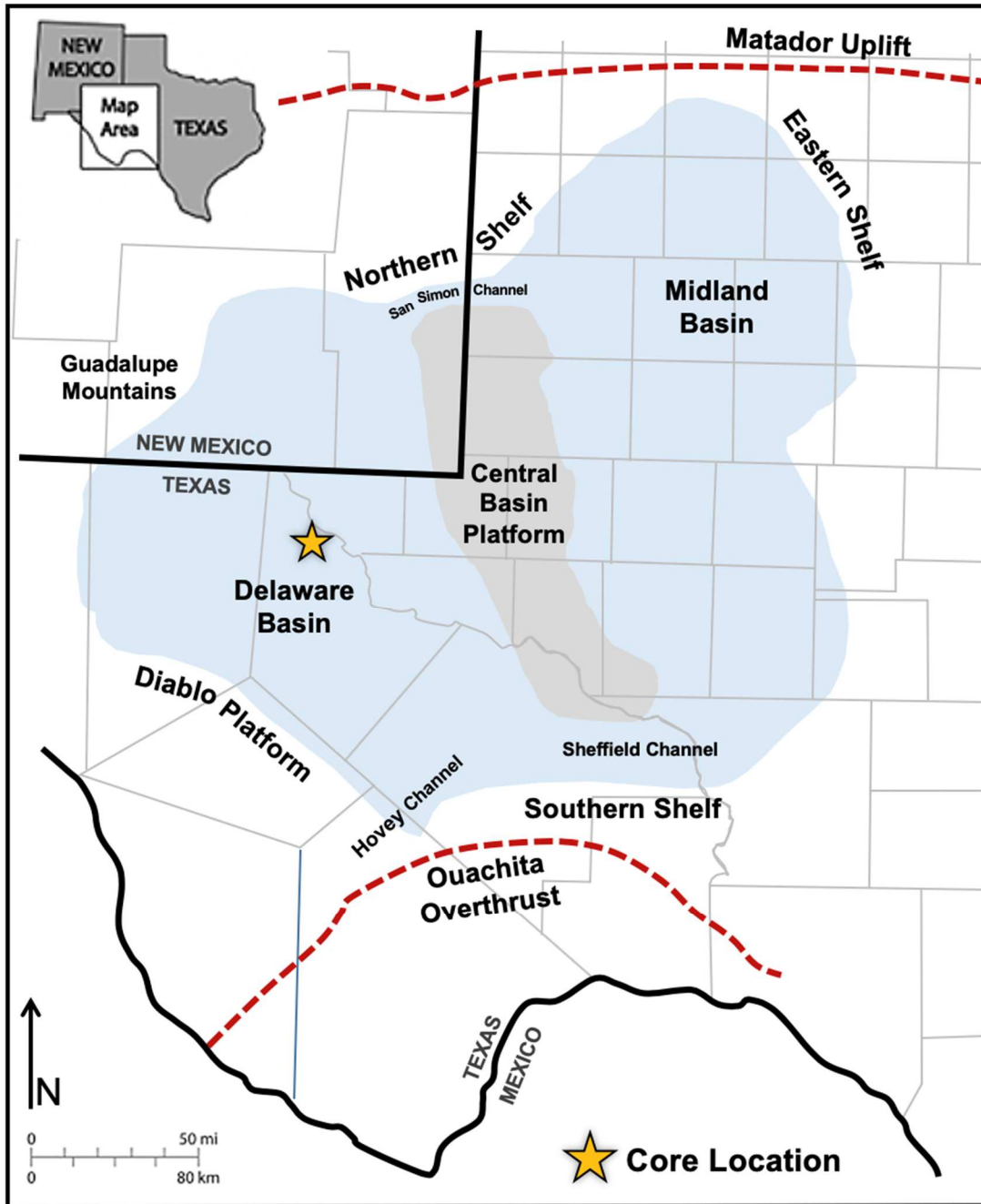


Figure 1.2—Permian Basin major structural components with the yellow star showing the location of the core used in this study (Based on Silver and Todd, 1969; Ruppel and Ward, 2013).

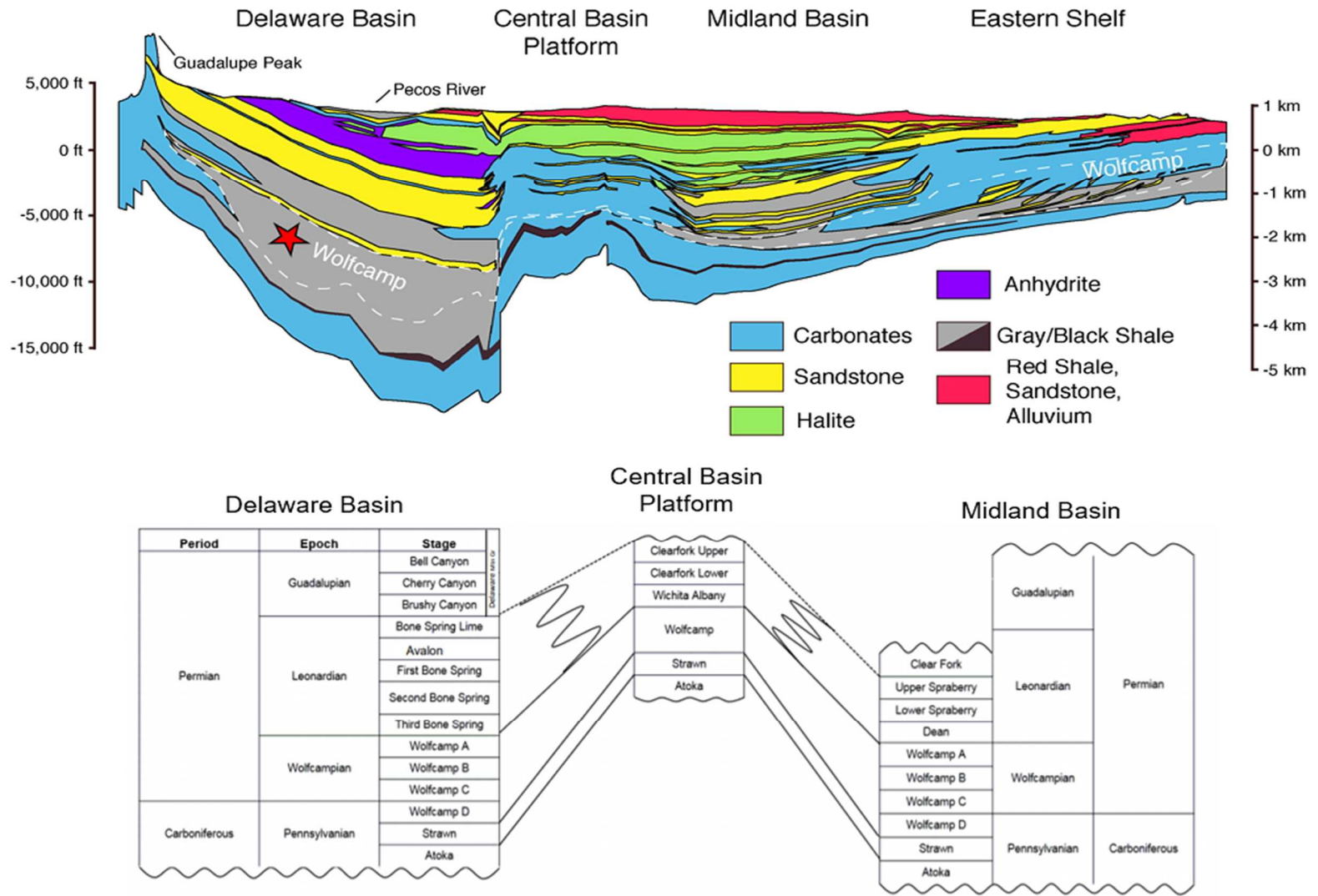


Figure 1.3—Regional cross section (top) and stratigraphic column (bottom) of the greater Permian Basin showing the Wolfcamp in the deeper Delaware Basin to the west and Midland Basin to the east separated by the Central Basin Platform (Engle et al., 2016 modified from Matchus and Jones, 1984; U.S. Energy Information Administration, 2018).

1.2 Research Objective, Dataset, and Methods

The objective of this study is to use core, core associated data, and wireline logs to investigate the vertical variability of lithofacies and reservoir quality in the Wolfcamp A, B, C, and D using the Thunder C20-13 #2H core from Reeves County, Texas. Goals for this study include the following: 1) using core and core analyses to describe lithofacies and facies distribution for the Wolfcamp intervals; 2) discuss key depositional processes of Wolfcamp deposits; 3) elemental analysis using high-resolution X-ray Fluorescence (XRF) data available for Wolfcamp A and B; 4) Source Rock Analysis (SRA) to assess the extent of thermal maturity, kerogen type, and hydrocarbon generative potential; 5) evaluate reservoir properties such as total organic carbon (TOC), porosity, permeability, rock strength, and fluid saturations by lithofacies and Wolfcamp intervals; and 6) investigate the controls of rock and fluid properties to associated well log responses in a normal well log suite.

To evaluate the Wolfcamp intervals for variations in lithofacies and reservoir quality, a core with coverage of the four intervals was used for this study. The core used is from the Thunder C20-13 #2H well, provided by Cimarex Energy. The well is located in the Phantom field in northeast Reeves County, Texas. Thunder C20-13 #2H was spud on November 17, 2014 and completed on March 28, 2015. The pilot hole was drilled first, followed by a sidetrack lateral well. In the pilot hole, the well was cored and wireline logs ran. A sidetrack well was used for production. From the first production in March 2015 to February 2021, the well has cumulatively produced 250,500 bbl of oil, 2,582 MMscf of gas, and 3.18 MMbbl of water. The well was perforated from 11,490 to 11,564 ft true vertical depth (TVD)—equivalent to 11,815 to 17,485 ft measured depth (MD) over a 5670 ft gross perforated interval in Wolfcamp C. A well test performed on April 4, 2015, submitted to the Railroad Commission of Texas, showed a gas-oil ratio (GOR) of 3600 and 48.0 API oil gravity. Figure 1.4 shows the well log suite of the Thunder C20-13 #2H pilot well, the cored intervals, and a summary of the dataset used to meet research objectives. The dataset and methods used in this study are discussed in further detail in the subsequent sections.

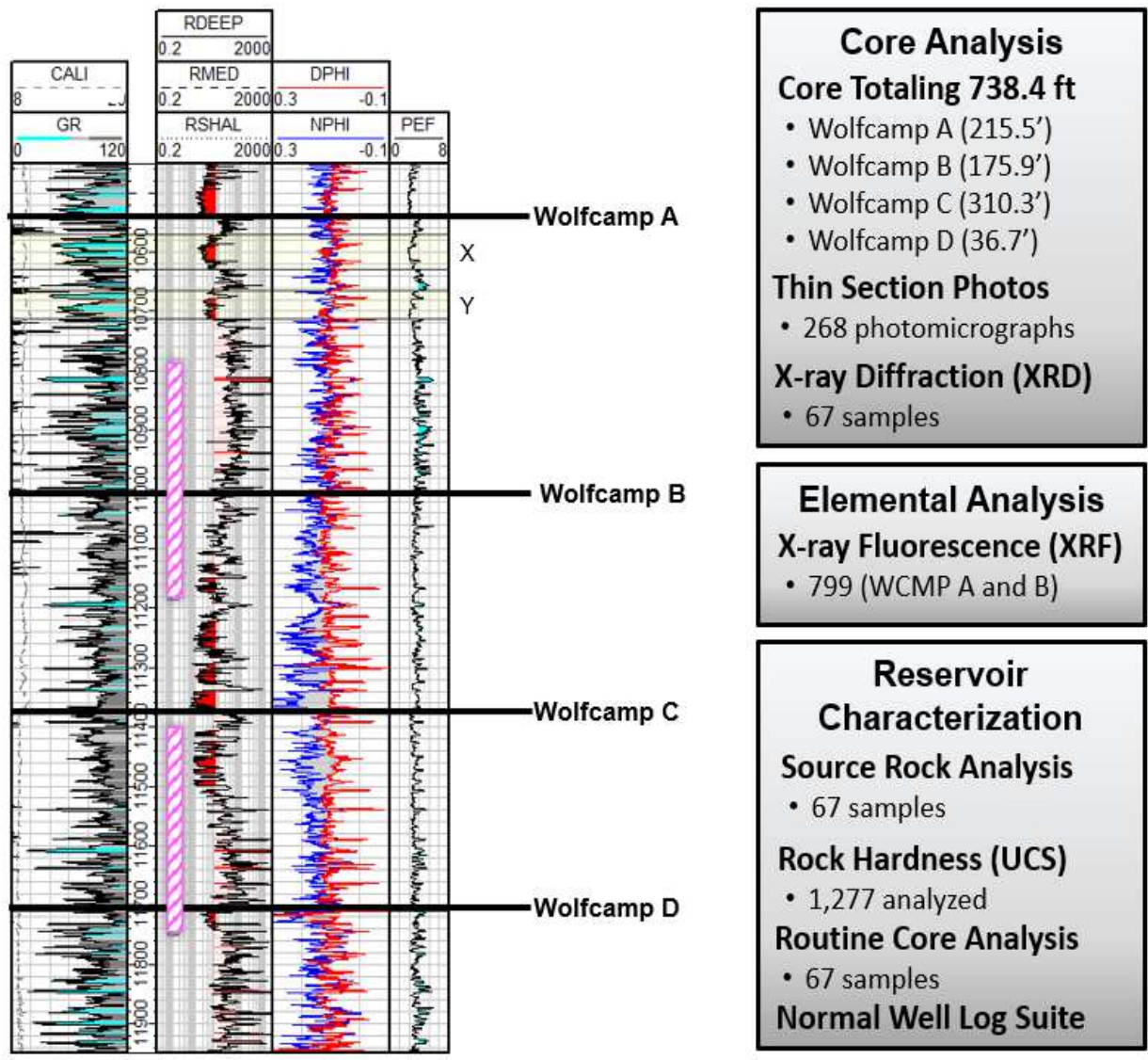


Figure 1.4—Well log of the Cimarex Energy Thunder C20-13 #2H pilot (left) with cored interval shown in the pink rectangles. A summary of the dataset used to meet research objectives (right) includes core, core associated data, and well logs.

Core Description

The available cored intervals examined in this study include (1) 10,780.0 to 11,173.2 ft from Wolfcamp A and B, and (2) 11,390.2 to 11,737.5 ft from Wolfcamp C and D. Excluding minor breaks in core, the total length of core examined was 738.4 ft. The core available for each interval is as follows: Wolfcamp A (215.5 ft), Wolfcamp B (175.9 ft), Wolfcamp C (310.3 ft), and Wolfcamp D (36.7 ft).

The core was described at millimeter- to centimeter-scale, capturing elements such as lithology, grain size, grain composition, color, sedimentary features, and type of contacts. The combination of these attributes provides critical information for defining lithofacies. Biogenic sedimentary structures, including microfossil varieties and bioturbation were noted. Microfossil assemblages provide information regarding the sediment source for carbonate-rich rocks. Trace fossils indicate the presence of organisms living within the sediment and provide environmental indicators for the time of deposition. This includes insights into water depth, current energy, and oxygen levels. The degree of bioturbation was noted from 0 to 5 using the bioturbation index proposed by Lazar and others (2015). Carbonates were described using the Dunham classification (1962). Core description was documented on Microsoft Excel and digitized using the software Strater to evaluate facies distribution. In addition to core description, 268 thin section photomicrographs were evaluated. However, the photomicrographs are confidential property of the Core Laboratory Core Consortium and images could not be republished for this study.

X-ray Diffraction (XRD)

X-ray Diffraction (XRD) is an analytical technique used to identify mineral components of core plug samples. A total of 67 XRD samples were analyzed at approximately 10 ft intervals for this study. The samples were prepared by Core Laboratories. XRD data provides essential bulk mineralogy data used to understand and interpret facies. For each sample, mineral constituents are reported in weight percent (wt.%) for the following minerals: anhydrite, ankerite, apatite, barite, chert, calcite, Fe-calcite, Mg-calcite, dolomite, Fe-dolomite, fluorapatite, gypsum, halite, K-feldspar, marcasite, plagioclase,

pyrite, quartz, siderite, sphalerite, and clays (chlorite, kaolinite, illite, smectite, and mixed layer illite-smectite).

X-ray Fluorescence (XRF)

X-ray Fluorescence (XRF) elemental data was sampled at 0.3 to 0.5 ft increments by Core Laboratories for a total of 799 measurements. The XRF dataset was available for the 391.4 ft cored section of Wolfcamp A and B. XRF provides elemental data in parts per million (ppm). The elemental concentrations for 41 elements analyzed include the following: silver (Ag), aluminum (Al), arsenic (As), gold (Au), barium (Ba), boron aluminide (BAI), bismuth (Bi), calcium (Ca), cadmium (Cd), cerium (Ce), chlorine (Cl), cobalt (Co), chromium (Cr), copper (Cu), iron (Fe), potassium (K), lanthanum (La), magnesium (Mg), manganese (Mn), molybdenum (Mo), niobium (Nb), neodymium (Nd), nickel (Ni), phosphorus (P), lead (Pb), praseodymium (Pr), rubidium (Rb), sulfur (S), antimony (Sb), selenium (Se), silicon (Si), tin (Sn), strontium (Sr), thorium (Th), titanium (Ti), uranium (U), vanadium (V), tungsten (W), yttrium (Y), zinc (Zn), and zirconium (Zr).

The XRF elemental dataset was evaluated in several ways. First, XRF elemental abundances were compared to mineralogical data from XRD in order to understand if elemental data can be used as mineral proxies. This was completed by focusing on the three dominant minerals found in the Wolfcamp, which are quartz, calcite, and illite, determined by XRD. Using an element-to-mineral model proposed by Nance and Rowe (2015), XRF elemental data was used to approximate normalized proportions of quartz, calcite, and illite. Applying the mineral model to high-resolution XRF data allows a better understanding of mineralogical changes between XRD samples throughout the Wolfcamp A and B. XRF data was also used to calculate a synthetic gamma ray log using elements of K, Th, and U. The fine sampling resolution for XRF can capture changes in gamma ray signal under the resolution of downhole logging tools, providing a more precise gamma ray profile. Finally, the XRF elemental dataset was used in examining elemental indicators using chemostratigraphic methods. This provides insights into the terrigenous influx, carbonate influx, and paleoredox conditions at the time of deposition.

Source Rock Analysis

A total of 67 Source Rock Analysis (SRA) measurements were obtained throughout the Wolfcamp intervals by GeoMark in Houston, Texas. The provided SRA data includes LECO TOC (wt.%), Rock-Eval S1 (mg HC/g), Rock-Eval S2 (mg HC/g), Rock-Eval S3 (mg CO₂/g), Tmax (°C), Ro calculated from Tmax (%Ro), hydrogen index (HI), oxygen index (OI), S2/S3, S1/TOC, and production index (PI). In addition, seven vitrinite reflectance (Ro) measurements were available from the Wolfcamp A, B, and C. Raw pyrograms provided quality control of pyrolysis data, including low S2 shoulders. SRA data is used to evaluate source rock quality, kerogen type, and the extent of thermal maturity.

Geomechanics

For unconventional reservoirs, such as the Wolfcamp Formation, the assessment of geomechanical properties is critical for fracture stimulation. Geomechanical properties are considered essential geoscience parameters that are used to inform fracture stimulation and reservoir models. Using available core, this study focuses on obtaining core-derived rock mechanic properties, specifically on unconfined compressive strength (UCS) as a method to estimate and evaluate rock strength. This was completed using an Equotip Bambino micro-rebound hammer.

Measurements were taken at 2- to 6-inch intervals in the Wolfcamp A, B, C, and D, totaling 1,277 measurements. The Equotip Bambino micro-rebound hammer produces data in values of Leeb Hardness (HLD), which is then used to calculate UCS using an empirical relationship by Zahm and Enderlin (2010). High-resolution measurements of rock strength from the Wolfcamp core were used to (1) evaluate rock strength as a function of lithofacies and (2) populate high-density rock strength data to understand the mechanical profile of the Wolfcamp below log resolution. Mineral-based brittleness index (MBI) was calculated using mineralogical data from XRD to investigate brittleness as a function of mineral controls.

Reservoir Properties

Routine Core Analysis (RCA) was conducted on 67 crushed rock samples at roughly 10 ft increments in the Wolfcamp A, B, C, and D. Analyses were performed by Core Laboratories. The data provided by RCA includes the following: total porosity (%), gas-filled porosity (%), matrix permeability (mD), grain density (g/cm^3), bulk density (g/cm^3), water saturation (%), gas saturation (%), and oil saturation (%). RCA data was used to characterize rock and fluid properties for lithofacies. These measurements are critical in assessing reservoir quality and in delineating potential reservoir and nonreservoir rocks found in the Wolfcamp Formation. Reservoir properties were also evaluated as a function of depth for each Wolfcamp interval.

Well Logs

In addition to core and core-derived data, the normal well log suite was evaluated for this study. The logs available include the following: caliper (CALI), gamma ray (GR), spectral gamma ray for uranium concentration (SGR_U), spectral gamma ray for thorium concentration (SGR_{Th}), spectral gamma ray for potassium concentration (SGR_K), resistivity curves (RSHAL, RMED, RDEEP), bulk density (RHOB), density porosity (DPHI), neutron porosity (NPHI), and photoelectric factor (PEF). Wireline log data is the most commonly available tool used to prospect, assess lithology, and interpret rock and fluid properties of the subsurface. When integrated with the available core dataset, the controls of rock and fluid properties on their associated well log responses were investigated.

1.3 Regional Setting

Late Precambrian to Late Mississippian (Tabosa Basin Phase)

During the Late Precambrian through Cambrian, the southwestern United States, where the Permian Basin would reside, was primarily a passive margin. Cooling and shrinking of the underlying mantle and crust resulted in the collapse of the transcontinental arch. Subsidence at the time was too slow to produce a structural basin. The Late Precambrian Grenville orogeny was a widespread tectonic event that resulted in high-angle basement faults that created Proterozoic lines of weaknesses (Hills, 1984; Sinclair, 2007).

In the Early Ordovician, the northwest-trending Ellenburger sea slowly transgressed into the West Texas and New Mexico region. The deposition of the Ellenburger Group, a carbonate shelf platform sequence, consists of dolomites and dense limestone (Hills, 1984; Loucks, 2005). Minor evaporites occurred in areas with restricted circulation. Towards the end of the Early Ordovician, crustal warping divided the Early Ordovician shelf into a series of sags and arches (Adams, 1965).

In the Middle Ordovician, the ancestral Tobosa Basin was formed when the region welded onto the southwestern portion of the North American craton and sank to create a broad, shallow, and gently dipping basin (Horak, 1985). The depression caused the sea to flood into the 350-mile long basin. The Tobosa Basin phase occurred until the Middle Paleozoic. Overlying the Ellenburger Group is the Simpson Group, composed of sandstone, shale, and limestone. The Simpson Group accumulated in lower portions of the Tobosa Basin with a clastic sediment supply derived from the Texas arch in the north and northwest. Towards the south, clastics transition into a shelfal limestone approaching the edge of the Marathon trough (Adams, 1965). The Simpson Group includes the Joins, Oil Creek, McLish, Tulip Creek, and Bromide Limestone (Hills, 1984; Hill, 2006).

The Tobosa Basin during the Late Ordovician, Silurian, and Devonian was largely covered in deepwater highstand conditions. Periods of rapid subsidence caused changes in relative sea level with starved portions in the basin center. Along marginal carbonate shelves, dense limestone, dolomite, and chert were deposited while mudstones were deposited on talus slopes (Adams, 1965). The Late Ordovician Montoya Group unconformably overlies the Simpson Group. The Montoya Group is composed of light- to medium-gray crystalline dolomite interbedded with shale and dark gray limestone (Hill, 2006). The subsequent drop in relative sea level resulted in the deposition of the Fusselman Formation. The Fusselman Formation consists of light gray, medium- to coarse-grained dolomite that unconformably overlies the Montoya Group. During the Late Silurian highstand, the Wristen Formation composed of shale and dolomite was deposited. Slight uplifts in the Late Devonian resulted in basin tilting to the east, exposing Upper Ordovician, Silurian, and Devonian strata to be truncated (Adams, 1965). By the Early Devonian, shelf carbonates developed along the shallow basin margins of the Tobosa Basin, while

limestones, cherts, and black shale accumulated in deeper regions of the basin. Thick carbonate units were deposited during the Early to Middle Devonian of the Thirtyone Formation (Hills, 1984; Hill, 2006).

During the Late Devonian to Early Mississippian, the Woodford Shale was deposited. The organic-rich Woodford Shale can be found widespread in regions that were submerged at the time of deposition. The Woodford Shale is regarded as the primary source rock for pre-Mississippian reservoirs (Adams, 1965). By the Late Mississippian, over 7,000 ft of Paleozoic sediment had accumulated in the axis of the Tobosa Basin. The accumulation of these pre-Pennsylvanian sediments produced compressional stresses relieved along zones of weakness in the subsidence axis. These lines of weaknesses were derived from a north-northwest trending trough that was an aulacogen on the edge of the North American craton during the Grenvillian Orogeny (Hills, 1984). This relief formed an uplift in the form of a horst-block ridge during the Late Mississippian that continued to develop as basin subsidence progressed (Adams, 1965). This ancient Paleozoic mountain range was the root of the Central Basin Platform. The rise of the ridge divided the primary Tabosa Basin into secondary basins (Hills, 1984). During this time, thick accumulations of basinal, black, organic shale of the Helms Formation were deposited.

Early Pennsylvanian to Early Triassic (Permian Basin Phase)

During the Early Pennsylvanian, Pangea was formed through the paleocontinental collision of Laurasia and Gondwana, ending the Tobosa Basin phase. This event caused crustal flexure that resulted in the formation of the Marathon-Ouachita Fold Belt. Subsequently, the uplift of the Central Basin Platform, in contrast to rapid subsidence of the secondary subbasins, separated the Delaware Basin and Midland Basin into distinct structural units (Hills, 1984; Horak, 1985; Hill, 2006; Hennenfent et al., 2015). In the Early Pennsylvanian, rapid subsidence of the Delaware Basin caused a vast deepwater region in the central and southern part of the subbasin. Deltaic sediment was deposited in shallow areas of depression, with clastics sourced from the uplifts to the northwest in central New Mexico (Hills, 1984). The primary episode of subsidence within the Delaware, Midland, and Val Verde Basins occurred in the Middle to Late Pennsylvanian (Hills, 1963; Adams, 1965; Yang and Dorobek, 1995). Tectonic activity sharpened, compressed, and faulted the

folds of the area around the Central Basin Platform. During this time, central New Mexico became further uplifted.

Early Ordovician to Middle Pennsylvanian strata is relatively uniform in thickness in the Delaware Basin with slight stratigraphic thickening towards the basin center. However, from the Late Pennsylvanian to Early Permian Wolfcampian time, strata in the Delaware Basin became more variable in thickness and diverse in lateral facies (Yang and Dorobek, 1995). The growth of broad carbonate banks along the basin margin, beginning in the Atokan time, caused the basin to be starved (Hills, 1984). Clastic sediments sourced from the northeast highlands were trapped on the trough of shelves behind barrier reefs and carbonate banks along the basin margin (Hills, 1963). In addition, Early Permian turbidity flows likely eroded the thin shale deposits and underlying strata (Adams, 1965). The structural elements of the Pennsylvanian time created a structural framework that allowed for the complex Permian reef systems to develop.

During the Late Pennsylvanian through Early Permian Wolfcampian times, the rate of subsidence was greater than the deposition of siliciclastics and carbonates. As a result, a deep basin formed, with margins attached to carbonate-dominated platforms by structurally steepened ramps. In the Delaware Basin, the basin center-to-shelf margin depth was estimated to have increased from 1,000 ft in the Early Wolfcampian times to 1,500 ft gradually by the end of the Wolfcamp deposition with slope gradients of over 7 degrees (Hill, 1984; Playton and Kerans, 2002; Kvale et al., 2020). Subsidence progressed concurrently with several thousand feet of uplift in the Diablo arch to the west and Star Mountain arch that borders the Delaware Basin. Other features include pop-up fault blocks and ridges developed to compensate for the compressional stresses due to crustal shortening (Adams, 1965). Marginal shelves and platforms promoted the growth of flanking reefs. The basin floor was over a thousand feet below the shelf along the deeper, eastern portion of the Delaware Basin. The development of marginal shelves caused the basin to be semi-restricted yet was able to sustain normal salinity levels (Hills, 1963).

The Late Pennsylvanian to Early Permian Wolfcampian strata consists primarily of deepwater facies deposited as a result of sediment gravity flows combined with hemipelagic settling (Yang and Dorobek, 1995). The term “deepwater” refers to the deposition of sediment below the storm wave base in slope-to-basinal environments. Several studies (Thompson, 1954; Ross, 1963; Mazzullo and Reid, 1987; Wilde, 1990; Wahlman and Tasker, 2013) have dated the Wolfcamp Formation using the fossil genera of fusulinid (*Parafusulina*, *Schwagerina*, *Eoparafusulina linearis*, *Pseudoschwagerina*, *Triticites-schwagerina*, and *Triticites*), ammonoid (*Properrinites*), and brachiopod (*Parakeyserlinginna*). At the time of Wolfcamp deposition from the Early to Late Wolfcampian time (Fig. 1.5.A-B), high-frequency sea level fluctuations occurred. This was the result of building then melting continental glaciers, but in general relative sea level rose by the start of the Early Leonardian. Turbidity flows, prevalent in the Wolfcampian seas, caused agitation and mixing of the water column. Algae and other planktonic forms flourished on the surface water that was later preserved as organic matter. Photic zones led to significant growths of carbonate banks along shallow basin margins, particularly along the north, northeast, and northwest Delaware Basin (Adams, 1965; Hills, 1984; Ward, 2013).

During the Late Wolfcampian time, repeating platform failure events resulted in the transportation of carbonate detritus down structurally modified ramps through a combination of sediment gravity flows and mass transport processes (Playton and Kerans, 2002; Kvale et al., 2020). In addition, fine-grained, organic-rich sediments were deposited in the basin. Clastics were sourced from the uplifted mountains from the west, northwest, southwest, and the Ouachita-Marathon mountains to the south (Adams, 1965). As marine circulation became more restricted, bottom conditions became increasingly more favorable for organic matter preservation. In the Delaware Basin, the thickness of Wolfcamp strata is impacted by Late Paleozoic tectonic activity associated with steeply dipping strike-slip faults. The thickest sections are attributed to the downthrown side of the fault (Yang and Dorobek, 1995).

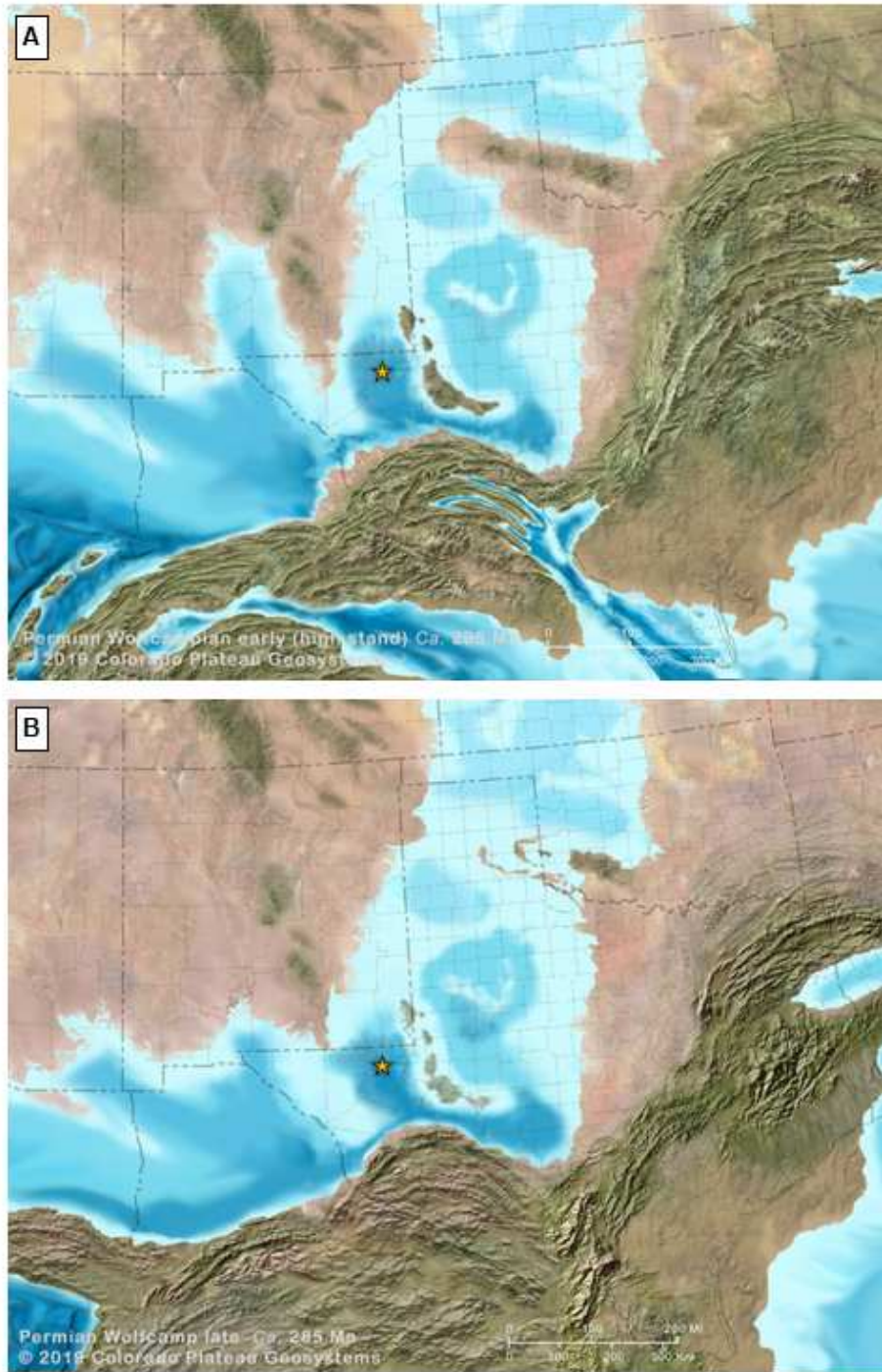


Figure 1.5—Blakey palaeogeographical maps modified from the Colorado Plateau Geosystems, Inc. (2019) for the time of Wolfcamp deposition. The two time sequences shown are (A) Early Wolfcampian 295 Ma, and (B) Late Wolfcampian time 285 Ma. The yellow star shows the approximate location of the well used in this study.

Sea Level Changes

During the Late Pennsylvanian to Early Permian time, the Gondwana subcontinent was in a period of continental glaciation (icehouse conditions). This time period was characterized by high-amplitude and high-frequency changes in eustatic sea level (Heckel, 1986; Fielding et al., 2008; Baumgardner et al., 2016). These fluctuations were caused by cyclic building and melting of ice sheets and continental glaciers (Heckel, 1986; Fielding et al., 2008). As a result, high-frequency cyclic marine sedimentation and complex stratigraphic architectures were developed (Wahlman and Tasker, 2013). The Wolfcampian time is subdivided into the lower Nealian stage and the upper Lenoxian stage (Ross and Ross, 1997). At the Pennsylvanian-Permian boundary, widespread ice sheets were interpreted to be at the maximum. The Nealian highstand was the last stage of icehouse conditions, in which sea levels were relatively low and rose progressively. The mid-Wolfcamp unconformity, separating the Nealian and Lenoxian stages, represents the most significant change in sea level during the Wolfcampian time (Ross, 1963).

During the middle Wolfcampian, a major fall in sea level (glacioeustatic lowstand) and tectonic pulses related to paleocontinental collision resulted in subaerially exposed shelves that were subsequently subjected to erosion (Wahlman and Tasker, 2013). The collapse of shelf-margin carbonates caused downslope mass movement of heterolithic, coarse-grained carbonates through mass transport processes, including debris flows and large slide blocks (Candelaria et al., 1992; Ruppel, 2001; Baumgardner et al., 2016). After the middle Wolfcampian during the Lenoxian stage, melting of ice sheets and waning continental glaciation resulted in a long-term overall rise in relative sea level that persisted into the Early Leonardian. The Early Leonardian was a period of transgression in which marginal shelves backstepped. During the Late Wolfcampian to Early Leonardian time, the amplitude and frequency of sea level changes also decreased (Wahlman and Tasker, 2013).

1.4 Previous Work

Comprehensive tectonic overviews of the Permian Basin and Delaware Basin have been published many times over the last sixty years (Hills, 1963; Adams, 1965; Shumaker, 1992; Yang and Dorobek, 1995; Ewing and Christensen, 2016). The Wolfcamp Formation was

first described by Udden and others (1916) based on outcrops found in the Glass Mountains that consist dominantly of shale and limestone, as well as some sandstone and conglomerates. The outcrops were subdivided into the following formations of Wolfcamp, Hess, Leonard, Word, Capitan, and Bissett formations. Candelaria and others (1992) later divided the Wolfcamp strata into Upper, Middle, and Lower Wolfcamp.

Most research up to the 1980s of the Permian Basin focused on stratigraphy and depositional processes of platform and slope carbonate deposits that were conventional hydrocarbon targets. Few works (Hobson et al., 1985a; Hobson et al., 1985b; Loucks et al., 1985) provided descriptions of Wolfcampian deepwater carbonate gravity flows for conventional carbonates exploration along basin margins. Hobson and others (1985b) described it as “the few frontiers remaining for carbonate exploration and research” in the Permian. However, the focus in literature began transitioning as production shifted basinward to the Wolfcamp and Bone Spring unconventional plays.

More recent papers (Kvale and Rahman, 2016; Thompson et al., 2018; Driskill et al., 2018; Kvale et al., 2020) have focused on Wolfcamp facies, facies associations, and depositional processes in the Delaware Basin. Deposits of the Wolfcamp Formation come from mixed carbonate-siliciclastic deepwater fan system with fans that can extend tens of kilometers in the Delaware Basin (Kvale et al., 2020). The depositional processes prevalent in the Wolfcamp are processes derived from suspension sedimentation, sediment gravity flows, and mass transport deposits that bring large volumes of shallow-water carbonate detritus into the deep basin (Driskill et al., 2018). Depositional models used to explain these Wolfcamp deposits have more or less used a combination of classical deepwater depositional models, such as the Bouma (1962) sequence for low-density turbidites and Lowe (1982) sequence for high-density turbidites. Another recently used depositional model, proposed by Haughton and others (2009), offers a siliciclastic hybrid event bed (HEB) classification that contains elements of both non-cohesive, turbulent flow and cohesive, laminar flow behavior in a single event bed. Kvale and others (2020) observed that carbonate HEBs seen in the Wolfcamp cores were very similar to the H-divisions seen in siliciclastic HEBs. Kvale and others (2020) published a study of Wolfcamp HEBs that included analysis of facies variations from core located in the distal fringe, off-axis, and

lateral fringe locations of a single mixed carbonate-siliciclastic deepwater fan in the Wolfcamp A.

Thompson and others (2018) identified eight lithofacies and four different cyclic packages that are related to the history of the basin infill processes of Wolfcamp A and B. The four different cyclic packages are the following: distal turbidites/hemipelagic, fine-grained turbidites, debrites, and calciturbidites. Driskill and others (2018) focused on utilizing X-ray Fluorescence (XRF) data for chemostratigraphy applications to understand geological controls on elemental content in high-resolution, sub-cm scale, focusing on the Bone Spring and Upper Wolfcamp intervals. Most literature on Wolfcamp deposits and depositional processes have focused on the Upper Wolfcamp (Wolfcamp A and B), which are the more common landing zones (Blomquist, 2016; Enverus, 2019). Hennenfent and others (2015) described the stratigraphy and log signatures of the various Wolfcamp intervals.

CHAPTER 2: CORE ANALYSIS

This chapter aims to combine core observations and mineralogical data to characterize the lithological changes that occur in the Wolfcamp intervals. Cored sections representing Wolfcamp A, B, C, and D were described and analyzed in this study. Core description aims to capture changes in lithology, sedimentary structures, bioturbation, and diagenetic features. Mineralogical data from X-ray Diffraction (XRD), in addition to elemental data from X-ray Fluorescence (XRF) were used for compositional analysis. The integration of these three techniques was combined to identify lithofacies, capture facies distribution, and evaluate the depositional processes that make up the stratigraphic section of the Wolfcamp Formation. A total of nine lithofacies were identified and described from Wolfcamp A, B, C, and D. The Wolfcamp Formation is composed of diverse lithologies, including organic-rich mudstones, calcareous mudstones, calcareous siltstones, carbonates, and argillaceous mudstones. Carbonates found in the Wolfcamp are more accurately termed calciclastics, which are clasts from carbonate margins that have been transported and redeposited through deepwater transport processes that are not formed *in situ* (Driskill et al., 2018). Clay-rich, organic-lean argillaceous mudstones and dolostones are also important lithofacies that occur abundantly in siliciclastic-dominated sections of the Wolfcamp intervals. Organic-rich siliceous mudstones, which have the highest average TOC, can be found in all four intervals of the Wolfcamp.

The Wolfcamp Formation is largely composed of lithofacies that were deposited as a result of calciclastic and siliciclastic sediment gravity flows. These sediment gravity flows transported sediment from surrounding platform margins into the basin. Between sediment gravity flows, periods of intermittent background sedimentation occurred. A sediment gravity flow is a term used to describe a mixture of sediment and water in which the sediment pulls interstitial water downslope due to gravity (Middleton and Hampton, 1973). Wolfcamp sediment gravity flows, from origin to distal terminus, have been estimated to flow considerable distances basinward from 25 to 34 miles (Hobson et al., 1985; Morgan et al., 1996; Kvale et al., 2020). The succession of alternating siliciclastic, calciclastic, and hemipelagic packages, makes up the larger Wolfcamp section. Carbonate event beds appear as cyclic, normally graded beds that are often capped with thin mudstones. The

noncalcareous mudstones that cap carbonate turbidites and hybrid event beds (HEBs) can preserve TOC upwards of 6.3 wt.% in this study and up to 8 wt.% in literature (Driskill et al., 2018). In contrast, siliciclastic event beds are most often thinly bedded, fine-grained turbidites. Siliciclastic turbidites generally have TOC less than 1 wt.%. Both carbonate and siliciclastic event beds are variable in thickness and can be found separated by intervals of background sedimentation. Event bed components and total thicknesses for both calciclastics and siliciclastic event beds can range from less than an inch to tens of feet in thickness.

The deposition of lower Permian facies reflects sea level fluctuations. The most common interpretation is the concept of reciprocal sedimentation (Van Siclen, 1958; Silver and Todd, 1969; Meissner, 1972), in which cyclic mixed carbonate and siliciclastic sedimentation occurred in the stratigraphic succession due to changes in relative sea level. The model suggests the dominance of siliciclastic deposition in the basin during lowstands as siliciclastic, terrigenous sand and silt are transported into the basin when adjacent platforms are subaerially exposed. During highstands, when the carbonate platforms are flooded, the dominance of carbonate deposition in the basin is derived from the transportation of shallow-water carbonates through structurally steepened ramps into the basin and basin margins as a result of deepwater transport processes. Noncalcareous, siliceous mudstones are deposited during both lowstand and highstand in periods of quiet, slow sedimentation (Handford, 1981; Hanford and Loucks, 1993; Kvale et al., 2020).

2.1 Compositional Analysis

Compositional analysis from 67 XRD measurements shows that while there are a variety of Wolfcamp rocks, their compositions vary in proportions of three mineral groups—siliceous minerals (quartz, feldspars, and micas, or QFM), argillaceous minerals (clays), and carbonate minerals (Fig. 2.1). On average, these three mineral groups make up 97 percent of the mineral constituents from XRD analyzed. The proportion of QFM range from 26.4 to 71.2 wt.%, with an average of 49.9 wt.%. Clays range from 9.1 to 52.5 wt.%, averaging 29.7 wt.%. Carbonates range from 0.8 to 58.3 wt.%, with an average of 16.9 wt.%. The dominant clay types found, from most to least abundant, include illite, illite/smectite, and chlorite. Carbonate minerals in the Wolfcamp are dominantly calcite

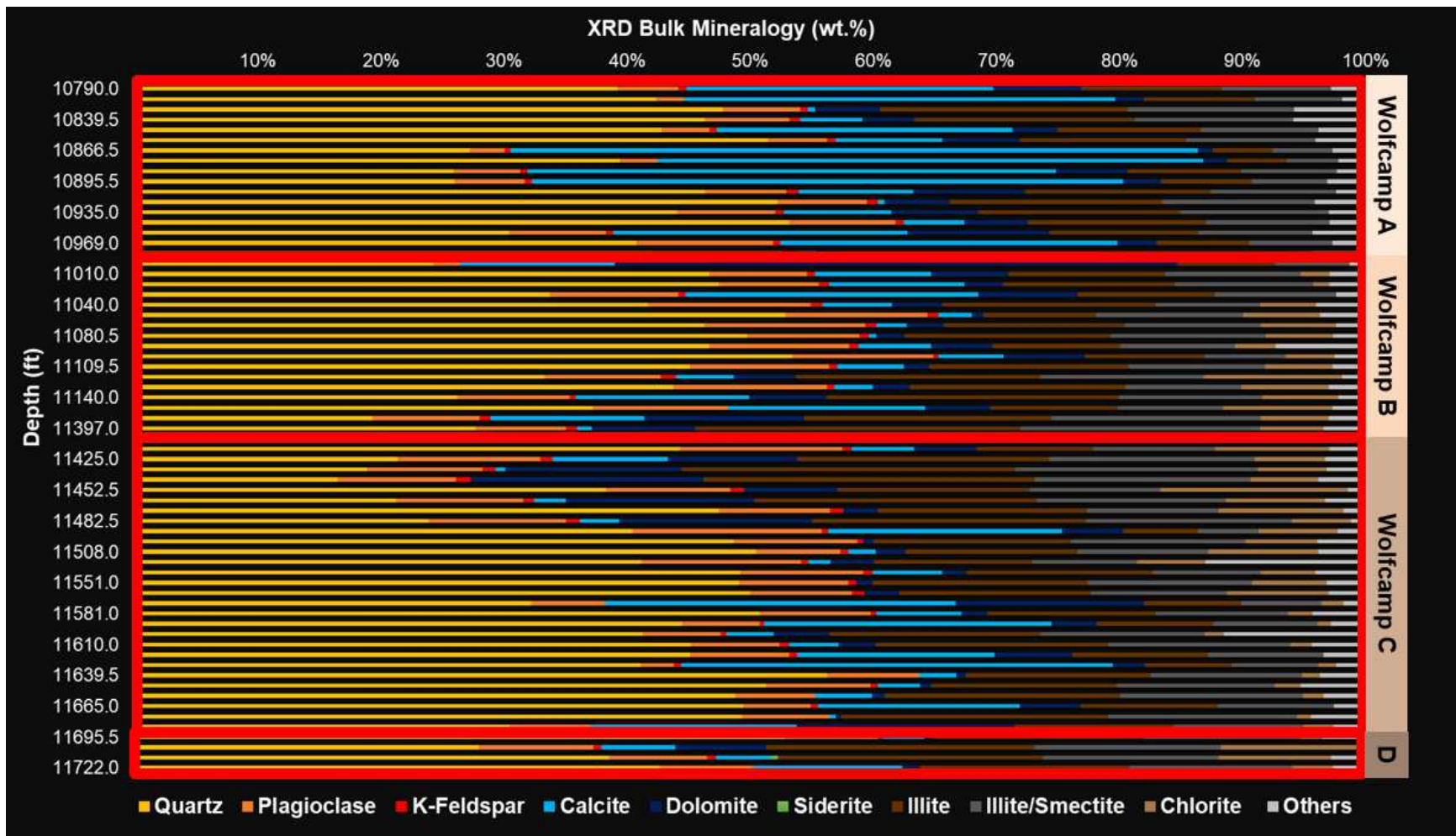


Figure 2.1—Mineral compositions from X-ray Diffraction (XRD) analyzed for Wolfcamp A, B, C, and D. Tectosilicates, such as quartz, potassium feldspars, and plagioclase, are shown in yellow, orange, and red. Carbonate minerals, primarily calcite and dolomite, are shown in blue. Clays are shown in brown and gray. Chlorite is abundant locally in Wolfcamp B, C, and D.

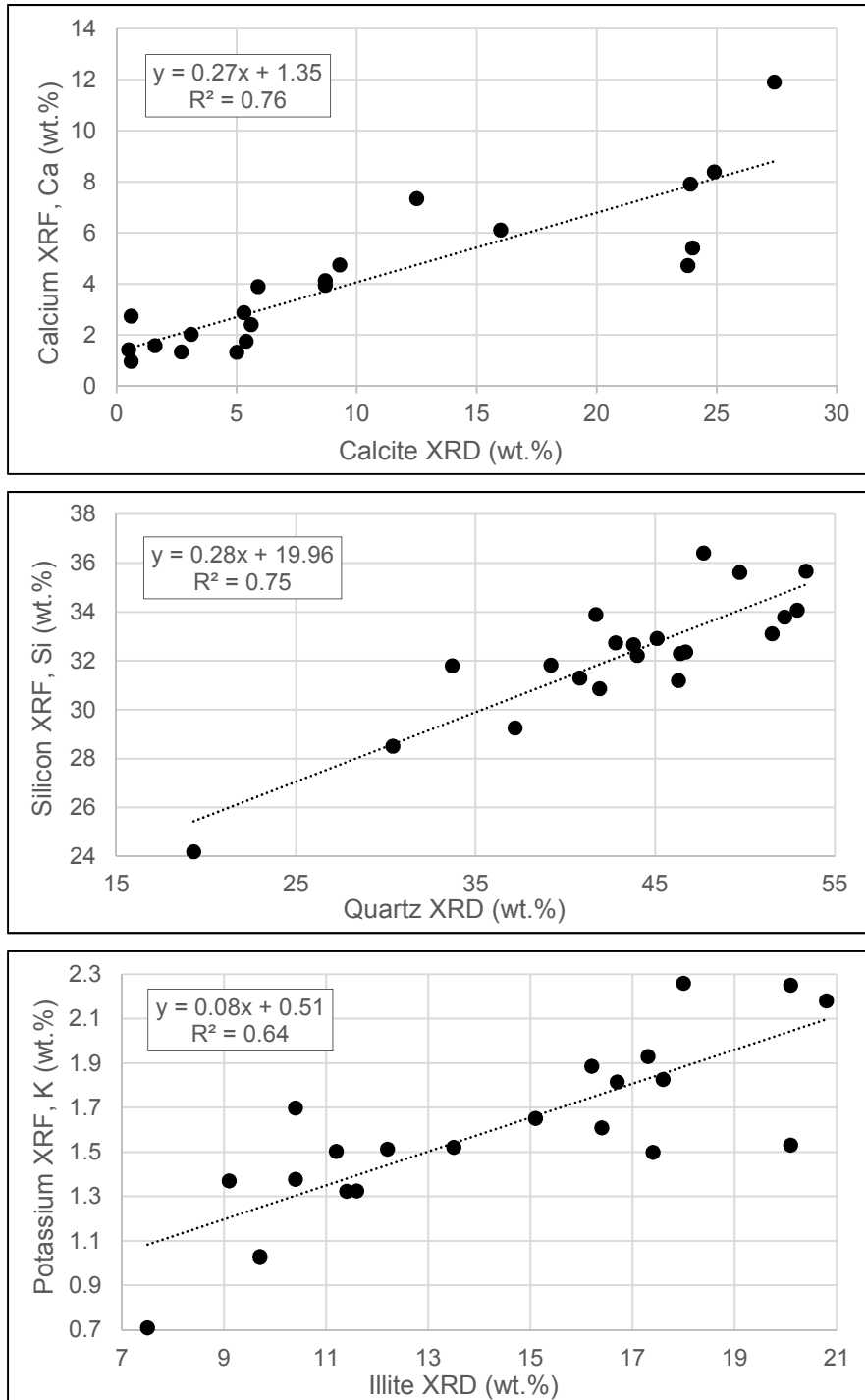


Figure 2.2—Scatter plots of elemental XRF data versus mineralogical data from XRD for 22 samples from the Thunder C20-13#2H core. The dashed line represents the best fit linear trendline.

and dolomite. The mineral group QFM is primarily composed of quartz with minor contributions from feldspars.

The three most abundant minerals observed are quartz, calcite, and illite. These three minerals represent, on average, 67 wt.% of samples analyzed. XRF elemental abundances of calcium (Ca), silicon (Si), and potassium (K) were examined in comparison to XRD mineralogical data for calcite, quartz, and illite. This investigates if elemental data can be used as mineralogical proxies for the three dominant mineral types in the Wolfcamp. Crossplots of Ca to calcite ($R^2 = 0.76$), Si to quartz ($R^2 = 0.75$), and K to illite ($R^2 = 0.64$) show positive correlations between the three elements to minerals (Fig. 2.2). The coefficient of determination (R^2) is a statistical measure of how close the data is to a fitted regression line. This quality check shows that elements from XRF (Ca, Si, and K) can be used to approximate mineral components, which are later applied in XRF analyses.

2.2 Lithofacies

Facies are mappable units of rocks that share physical, chemical, and/or biological attributes. Lithofacies, specifically, describe rocks that have similar physical rock characteristics, including mineral composition and grain size (textures). In this study, four facies groups were first defined based on mineral composition. Wolfcamp rocks are composed of 97 percent QFM, carbonates, and clays, on average. Using these three mineral groups as end members of a ternary diagram, facies groups can be evaluated based on the relative proportions of these three end members. Four facies groups were identified, including the siliceous facies group, mixed facies group, calcareous facies group, and argillaceous facies group. The four facies groups were subdivided into nine lithofacies based on grain size, grain type, and key sedimentary structures (Fig. 2.3). The siliceous facies group, primarily composed of 50 percent or more QFM normalized, can be subdivided into siliceous mudstone, bioturbated siliceous mudstone, and carbonate-rich siliceous mudstone lithofacies. The mixed facies group is composed of mixed calcareous silty mudstone. The calcareous facies group, composed of 50 percent or more carbonate minerals normalized, includes calcareous siltstone, skeletal packstone, dolostone, and wackestone lithofacies. Finally, the argillaceous facies group is composed of the argillaceous mudstone lithofacies.

Using a similar nomenclature as proposed by Lazar and others (2015), lithofacies names were assigned using two main components. First, a root term is defined based on dominant grain size using terms such as “mudstone” or “siltstone.” The grain size term is preceded by a modifier based on composition or defining core attribute. Combining the two components, a “siliceous mudstone” describes a rock that primarily consists of clay-sized grains that are dominantly composed of QFM mineral proportions. An additional modifier can be applied; for example, a “bioturbated siliceous mudstone” that has similar grain size and mineral components, but the latter has a distinguishing sedimentary feature that differentiates the two facies. The Dunham (1962) classification was used to describe coarse-grained, carbonate facies. For example, a packstone is grain-supported with more than 10 percent mud (micrite). A wackestone is mud-supported with more than 10 percent grains. Each lithofacies is summarized in Figures 2.4 and 2.5.

2.2.1 Siliceous Mudstone

The siliceous mudstone facies is a dark gray to black, structureless mudstone with clay to very fine silt-sized grains (0.12 to 3.9 μm). The siliceous mudstone can be found in all Wolfcamp intervals, representing 16 percent of the total cored interval in this study. Compositionally, the siliceous mudstone is dominantly QFM (avg. 58.2 wt.%) with significant portions of clay (avg. 32.8 wt.%) and minor carbonate minerals (avg. 5.0 wt.%). Framework grains of the siliceous mudstone are primarily subangular detrital quartz. The undifferentiated matrix is comprised of clays, plagioclase, pyrite, and organic matter. The siliceous mudstone is the darkest lithofacies in color, likely attributed to high clay and organic content. Clays and organic matter are found in the matrix surrounding the framework grains. The clay component is composed dominantly of illite and mixed layer illite-smectite. Organic matter can be found disseminated in the matrix and as wispy strands of elongated, compacted masses in thin sections. The siliceous mudstone has the highest average TOC of 2.6 wt.%, ranging from 1.5 to 6.3 wt.%. The presence of organic matter suggests high organic matter productivity and suitable preservation conditions. The siliceous mudstone also has high porosities ranging from 7.6 to 12.0 percent, with an average of 9.4 percent.

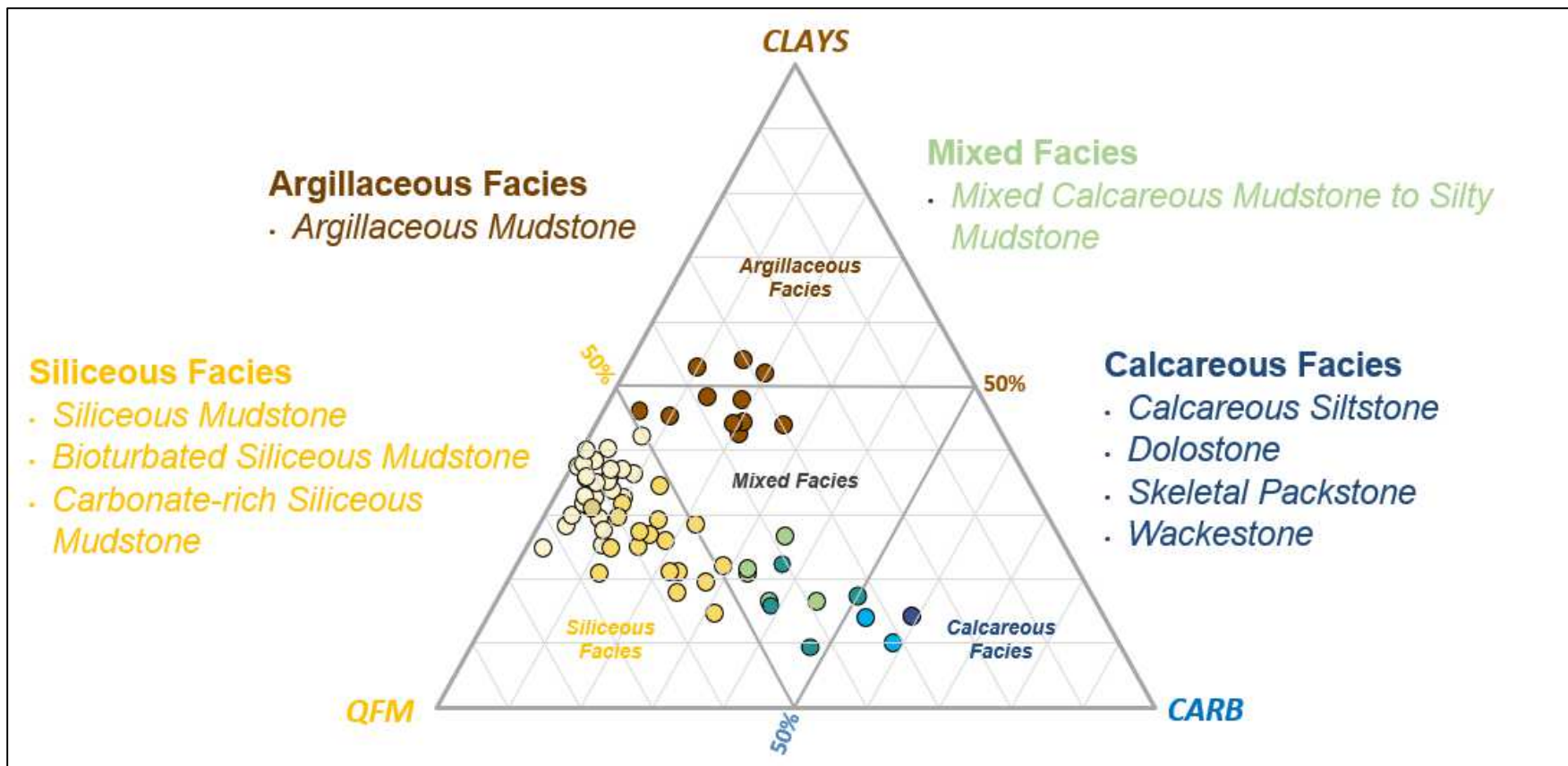


Figure 2.3—Ternary diagram with end members of the three key mineral groups—quartz, feldspars, and micas (QFM), carbonates (CARB), and clays. Samples with XRD (n=67) are first used to define facies groups based on mineral components, then subdivided into lithofacies based on elements captured from core description.

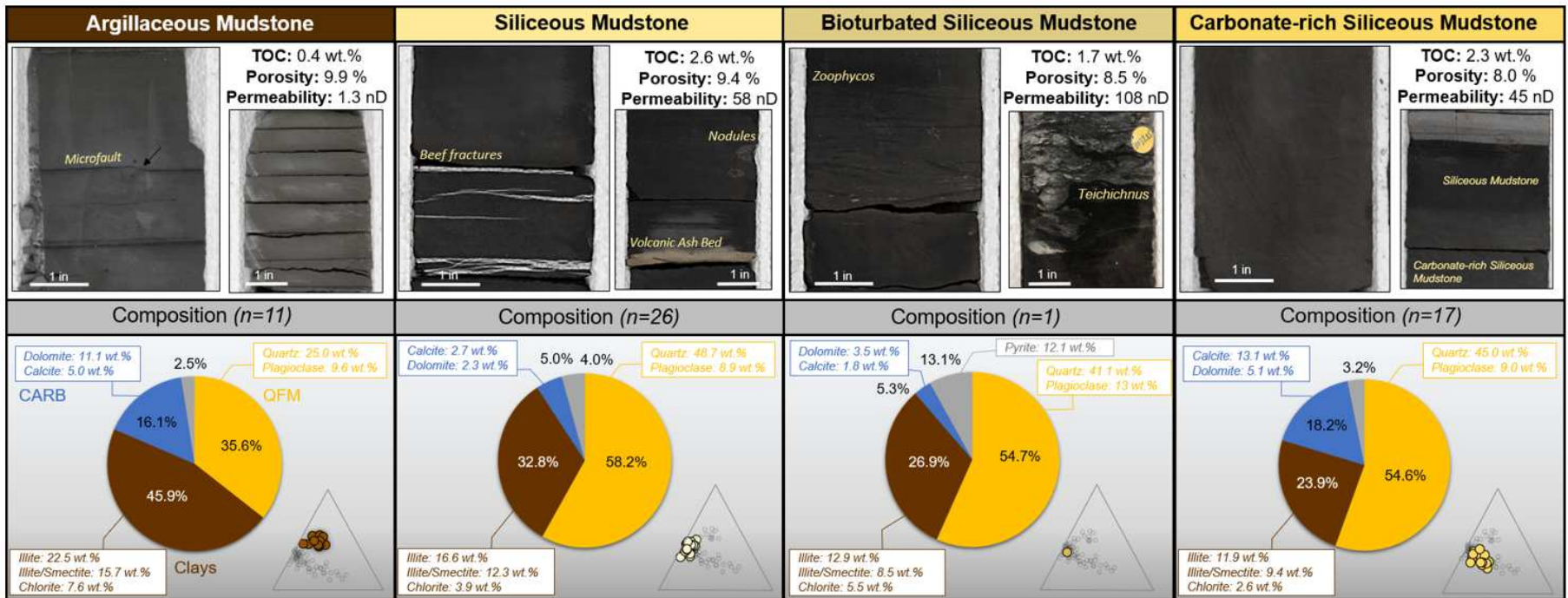


Figure 2.4—Summary of the Argillaceous Facies Group and Siliceous Facies Group lithofacies. The Argillaceous Facies Group consists of the Argillaceous Mudstone. The Siliceous Facies Group includes the Siliceous Mudstone, Bioturbated Siliceous Mudstone, and Carbonate-rich Siliceous Mudstone. For each lithofacies, the top section consists of two core images and average reservoir properties, including total organic carbon (TOC), porosity, and permeability. The bottom consists of X-ray Diffraction (XRD) compositional data. The pie chart shows the average weight percentages of QFM (yellow), clays (brown), carbonates (blue), and other minerals (gray). The call-out boxes show average mineral constituents for each mineral group.

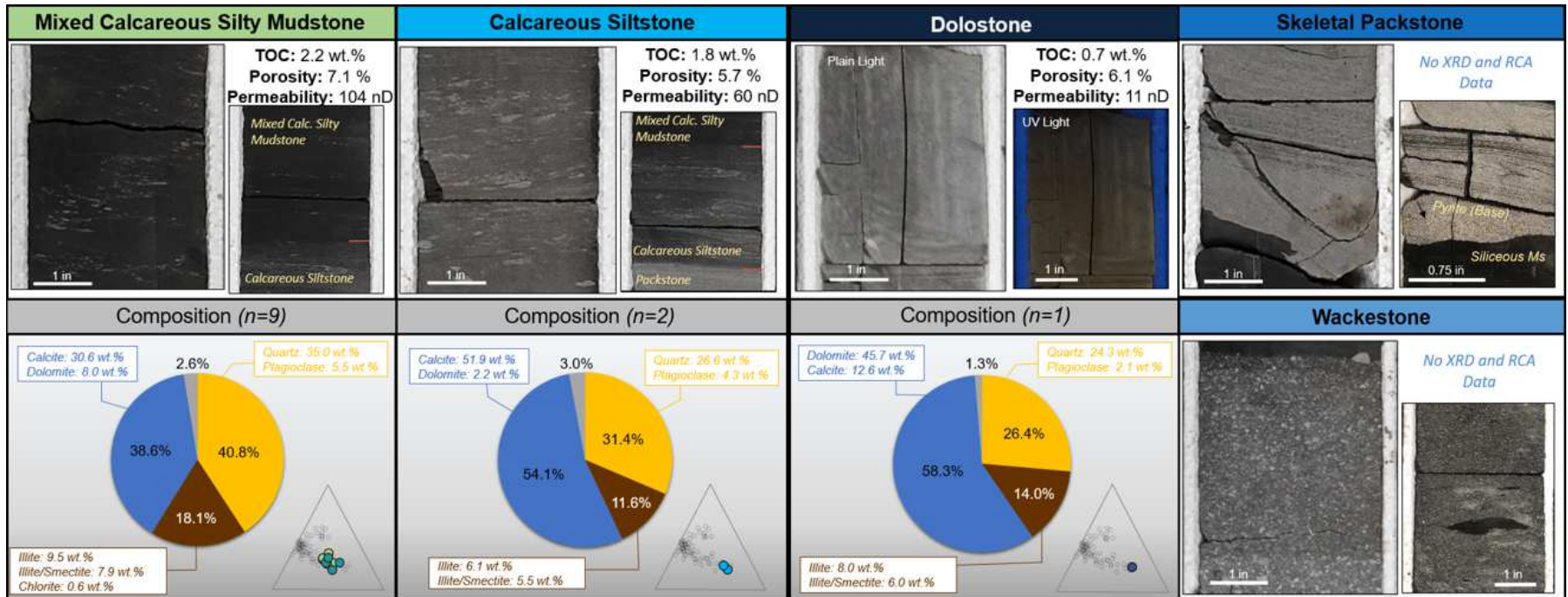


Figure 2.5—Summary of the Mixed Facies Group and Calcareous Facies Group lithofacies. The Mixed Facies Group consists of the Mixed Calcareous Silty Mudstone. The Calcareous Facies Group includes the Calcareous Siltstone, Dolostone, Skeletal Packstone, and Wackestone. For each lithofacies, the top section consists of two core images and average reservoir properties, including total organic carbon (TOC), porosity, and permeability. The bottom consists of X-ray Diffraction (XRD) compositional data. The pie chart shows the average weight percentages of QFM (yellow), clays (brown), carbonates (blue), and other minerals (gray). The call-out boxes show average mineral constituents for each mineral group.

While most commonly appearing massive, sedimentary structures associated with the siliceous mudstone lithofacies are the following: (1) faint, planar to subplanar, parallel laminations, (2) rare calcareous lag deposits, (3) phosphatic nodules, (4) horizontal “beef” fractures, and (5) volcanic ash beds. Faint, thin laminations of less than 0.1 inches thick, that show compositional variation between slightly siltier to more clay-rich laminae, are the most common sedimentary structure. Carbonates are minor constituents of the siliceous mudstone. However, rare calcareous lag deposits within the siliceous mudstone show allochems, including sponge spicules, radiolarians, and other fossil fragments. These bioclasts make up most of the sand-sized (>62.5 μm) grains found in the siliceous mudstone, likely transported due to bottom currents. Individual dolomite grains can also be found in thin section as euhedral, rhombic, and highly birefringent grains. Phosphatic nodules in core are spheroidal, ellipsoidal, or elongated in shape. These small nodules (0.4 to 2.0 inches) lack internal structure, often with a cryptocrystalline texture. Deformation of bedding and laminations above and below the nodule show small displacement of the mud matrix. Nodules are local cementation that primarily occurs during early diagenesis, commonly formed around an organic nucleus. Phosphatic nodules and concretions are allowed to grow in low influx environments. Horizontal “beef” fractures found in siliceous mudstones are absent in organic-lean facies. Beef fractures are most frequently found parallel to bedding or more rarely inclined or staggered. Beef fractures have been associated with organic-rich, thermally mature, and overpressured shales formed through petroleum expulsion during hydrocarbon generation (Al Duhailan et al., 2015). Thin volcanic ash beds comprised of brown, fissile claystone were observed in some siliceous mudstone beds, particularly in Wolfcamp A and B. In Wolfcamp literature, the sources of volcanic ash beds have been interpreted to be from the Delicias Volcanic arc, Sonoran arc, and Pacific arc volcanism (Centeno-Garcia, 2005; Lesli et al., 2019; Waite et al., 2019).

The siliceous mudstone facies is interpreted to be the mud cap of a waning flow or background suspension settling in a low energy environment with slow sedimentation rates. The small overall grain size and commonly massive mudstone suggest that these sediments were deposited in a low energy environment. Thin laminations of alternating clay and silt indicate some periods of alternating energy regimes or reworking of weak, bottom currents.

The high TOC associated with siliceous mudstones suggests high organic matter productivity with suitable preservation conditions. Furthermore, pyrite (avg. 3.1 wt.%) is most commonly found as framboids or, more rarely, as disseminated floccules and euhedral crystals. The presence of pyrite framboids is often associated with bacterial reduction of organic matter in euxinic to anoxic depositional conditions, where free H₂S is found in the water column.

2.2.2 *Bioturbated Siliceous Mudstone*

The bioturbated siliceous mudstone facies has a similar clay matrix, grain size, and composition to the siliceous mudstone; however, syndepositional modification by burrowing organisms can be seen in the core from various traces. The bioturbated siliceous mudstone is commonly found massive with associated sedimentary structures that include faint, planar to subplanar laminations and phosphatic nodules. The distinguishing characteristic of the bioturbated siliceous mudstone is mud-filled or silt-filled burrows. Molds showing the external forms of the burrows are preserved in the fine-grained mudstone matrix. Bioturbated siliceous mudstone represents primary sedimentation of the siliceous mudstone with syndepositional modification further reworked by burrowing organisms after deposition. The original depositional fabric of the siliceous mudstone is preserved when the bioturbation index is low.

Deepwater ichnofossil traces observed include *Nereites*, *Helminthopsis*, *Chondrites*, *Zoophycos*, and *Teichichnus*-like traces. Similar traces have been noted in literature (Kvale et al., 2020; Colburne, 2020), including *Chondrites*, *Helminthopsis*, *Cosmorphaphe*, *Planolites*, and *Thalassinoides* from Wolfcamp strata in the Delaware Basin. *Chondrites*, *Phycosiphon*, *Teichichnus*, *Zoophycos*, and *Planolites* have been observed in the Midland Basin (Murphy, 2015; Ward, 2017). In order for benthic communities to develop, their presence is controlled by environmental variables, including oxygen levels, water chemistry, depositional rate, and bottom water energy (Seilacher, 1977). A purely anoxic environment lacking dissolved oxygen would be uninhabitable to burrowing organisms. The occurrence of sediment-filled burrows suggests some available oxygen in the environment. Most bioturbated intervals were observed to contain one or two varieties of

ichnofossil traces. The low diversity of ichnofossil traces found in bioturbated intervals implies initial colonization with ecological stresses.

The lower TOC, compared to siliceous mudstone, is possibly due to the destruction of organic matter from biogenic activity. Bioturbated intervals are generally thin, with an average thickness of 3.9 inches. Only one sample for bioturbated siliceous mudstone was available for XRD and RCA analysis. Compositionally, the bioturbated siliceous mudstone is composed of QFM (54.7 wt.%), clays (26.9 wt.%), carbonates (5.3 wt.%), and other minerals (13.1 wt.%). The sample consists of 12.1 wt.% pyrite that makes up the bulk proportion outside of the three mineral groups.

2.2.3 Carbonate-rich Siliceous Mudstone

The carbonate-rich siliceous mudstone facies is dominantly composed of QFM (avg. 54.6 wt.%) with subequal proportions of clays (avg. 23.9 wt.%) and carbonates (avg. 18.2 wt.%). Compared to the siliceous mudstone and the bioturbated siliceous mudstone, the carbonate-rich siliceous mudstone has lower clay and higher carbonate proportions. The carbonate-rich siliceous mudstone is usually lighter in color than the siliceous mudstone (Fig. 2.4). In core, the carbonate-rich siliceous mudstone is a medium- to dark-gray, massive mudstone with visible silt-sized calcareous specks. These calcareous specks are disseminated throughout the matrix or in mm-scale groupings that lie parallel to bedding. Normally graded, upward fining beds are observed with decreasing silt-sized, calcareous specks at the top of the bed. The carbonate-rich siliceous mudstone is often in a sharp or graded contact from the basal mixed calcareous silty mudstone lithofacies. In thin section, the framework grains of the carbonate-rich siliceous mudstone are more variable, consisting of detrital quartz and allochem fragments. Compared to lithofacies in the mixed and calcareous facies groups, the allochem fragments in the carbonate-rich siliceous mudstone are more fragmented and smaller in size. Microfossils observed include sponge spicules, brachiopod fragments, radiolarians, and foraminiferas. The carbonate-rich siliceous mudstone can be found in all Wolfcamp intervals ranging from 0.12 inches to 7.2 feet in thickness, with an average thickness of 7.2 inches. The carbonate-rich siliceous mudstone is the most common lithofacies observed, comprising of 24 percent or 174.1 feet

of core examined. Average reservoir properties include porosity of 8.0 percent (range: 4.5 to 10.3 percent) and TOC of 2.3 wt.% (range: 1.1 to 3.6 wt.%).

2.2.4 Mixed Calcareous Silty Mudstone

The mixed calcareous silty mudstone facies contains subequal proportions of QFM (avg. 40.8 wt.%) and carbonate minerals (avg. 38.6 wt.%) with lower clays (avg. 18.1 wt.%). The mixed calcareous silty mudstone is structureless, normally graded, and commonly fines upwards to the carbonate-rich siliceous mudstone. Compared to the siliceous facies group, the mixed calcareous silty mudstone is composed of more carbonate components that are visible in both core and thin section. The mixed calcareous silty mudstone contains higher amounts of calcareous silt-sized specks compared to the carbonate-rich siliceous mudstone. In the mixed calcareous silty mudstone, elongated concentrations of silt-sized grains are common. Similar structures have been interpreted by Haughton and others (2009) to occur due to dewatering and compaction that cause fine grains (such as clays) to be elutriated while concentrations of larger grains remain. As the bed fines upwards, these concentrations of silt-sized grains begin to decrease. Reservoir properties from RCA of the mixed calcareous silty mudstone show porosities that range from 4.9 to 9.4 percent, averaging 7.1 percent. Core permeability varies significantly from 8 to 340 nD, averaging 104 nD. TOC ranges from 1.4 to 2.7 wt.%, with an average of 2.2 wt.%. The mixed calcareous silty mudstone accounts for 17 percent of the total cored interval, equivalent to 121.8 feet. The thickness of each bed ranges from 0.24 inches to 4.7 feet, with an average thickness of 6.0 inches.

2.2.5 Calcareous Siltstone

The calcareous siltstone facies is medium gray, massive, and composed of 50 percent or more subangular to subrounded, silt-sized grains. These silt-sized grains are calcareous fragments. Compositionally, the calcareous siltstone is dominantly comprised of carbonates (avg. 54.1 wt.%) with QFM (avg. 31.4 wt.%) and clays (11.6 wt.%). Beds of the calcareous siltstone show normal grading with decreasing silt and higher clay proportions as the bed fines upwards. A distinguishing sedimentary structure associated with the calcareous siltstone is “clotted” textures or “pseudonodules” that have been

previously described by Haughton and others (2009) and Kvale and others (2020). These “clotted” textures are absent in other facies and have been interpreted as fluid escape structures in past studies. The base of the calcareous siltstone often has a sharp basal contact to the underlying skeletal packstone. Graded contacts were also observed. The calcareous siltstone commonly underlies the mixed calcareous silty mudstone. The calcareous siltstone lithofacies accounts for 10 percent or 74.4 feet of the cored interval. The thickness of the calcareous siltstone ranges from 0.10 inches to 1.9 feet, with an average thickness of 2.4 inches. Bulk composition of the calcareous siltstone is dominantly calcite (avg. 51.9 wt.%), quartz (avg. 26.6 wt.%), illite (avg. 6.1 wt.%), illite/smectite (avg. 5.5 wt.%), and plagioclase (avg. 4.3 wt.%). The calcareous siltstone has an average porosity of 5.7 wt.%, average permeability of 59.7 nD, and average TOC of 1.8 wt.%.

2.2.6 Skeletal Packstone

The skeletal packstone facies is light- to medium-gray in color, massive to laminated, and has typical grain sizes ranging from very fine to fine sand-sized grains (62.5 to 125 μm). The skeletal packstone is composed of moderately well to well-sorted, subangular to subrounded grains. In core, packstones show normal grading, with the coarsest grains at the base of the bed fining upwards. At the top of the packstone bed, banding of alternating light packstone with dark, more clay-rich siltstone can be seen. Sedimentary structures associated with the skeletal packstone include the following: (1) small, elongated mudstone clasts that lie parallel to bedding; (2) planar, parallel to ripple cross laminations, (3) soft sediment deformation and dewatering features; and (4) sharp, slightly erosive basal contacts. Planar, parallel laminations are common in the packstone lithofacies. Ripple lamination can be found but occur less frequently. Dewatering features such as flame structures and convoluted bedding are common. The skeletal packstone has characteristically sharp, slightly erosive basal contacts that typically overlie mudstones. Pyrite can be found at or near the basal contact when a packstone bed is in contact with organic-rich mudstones below. Packstone facies observed in this study range from less than 0.1 inches to 6.5 feet thick, with an average thickness of 3.3 inches. Skeletal packstones account for 10.6 percent of the total cored section, totaling almost 80 feet. While no RCA or XRD measurements were available for this lithofacies, similar lithofacies have been

described in the literature from both Delaware and Midland basins (Baumgardner et al., 2014; Turner, 2016; Driskill et al., 2018; Kvale et al., 2020; Bievenour, 2019). In a study of the Delaware Basin, Kvale and others (2020) reported reservoir properties for the skeletal packstone to have low porosities (avg. 2.3 %), poor TOC (less than 1 wt.%), and low clay content (less than 4 %).

2.2.7 Dolostone

The dolostone facies is yellow to yellow-gray in plain light, commonly structureless with sparse, thin, planar laminations. A distinguishing characteristic of a dolostone bed is the dull orange fluorescence in core under ultraviolet (UV) light. The nature of fluorescence for the dolostone is likely mineral fluorescence. One XRD sample of the dolostone lithofacies shows that bulk mineralogy is dominantly attributed to dolomite at 45.7 wt.%. Other constituents include quartz (24.3 wt.%), calcite (12.6 wt.%), illite (8.0 wt.%), plagioclase (2.1 wt.%), and pyrite (1.3 wt.%). Petrographic analysis shows that the matrix consists of authigenic, microcrystalline dolomite with several stages of growth. Euhedral, rhombic, dolomite can be seen in the last stage of growth. Dolostone beds occur in conjunction with argillaceous mudstone beds displayed in thin fine-grained turbidites. The dolostone beds are most evident under UV light. One dolostone RCA sample shows low TOC of 0.7 wt.%, porosity of 6.1 percent, and low permeability of 11.2 nD. The dolostone lithofacies represents 2 percent, equivalent to 11.9 feet, of the total cored interval. The average thickness is 7.9 inches, ranging from 0.5 inches to 2.0 feet.

2.2.8 Wackestone

Wackstones have a dark gray to black mudstone matrix with light gray, poorly-sorted skeletal bioclasts that are chaotically arranged. These bioclasts range from silt- to granular-sized and are subrounded to subangular. The microfossil assemblage includes crinoids, sponge spicules, brachiopods, fusulinids, and other shelfal fossil fragments. Fusulinids, which were prevalent during the Wolfcampian and Leonardian times, are found in maximum water depths of 30 to 100 feet (Fitchen, 1997). The presence of shallow-water biota indicates that wackestones likely originated from shallow-water shelves or margins. The wackestone lithofacies is interpreted as deposits of debris flows transporting shallow-

water bioclasts to the basin based on several observations. These include the following: (1) chaotically arranged, poorly-sorted clasts, (2) lack of sedimentary structures, and (3) sharp basal and upper contacts. Wackestone deposits from this study are likely the distal, fine-grained equivalents to the calcareous paraconglomerates and breccias from more proximal settings that have been described from literature (Silvis, 2001; Baumgardner et al., 2016; Kvale et al., 2020). Calcareous paraconglomerates and breccias were not observed in this study. No RCA and XRD data were available for the wackestone lithofacies.

2.2.9 Argillaceous Mudstone

The argillaceous mudstone facies is medium to dark greenish-gray in color and can be structureless to laminated. Thin, silty laminae in the argillaceous mudstone contain dominantly quartz and feldspar grains. Other sedimentary structures associated with the argillaceous mudstone include mm-sized, dark gray to black, elongated rip up clasts and microfaults. Microfaults are frequently found at contacts between the argillaceous mudstone and other lithologies. Compositionally, the argillaceous mudstone has the highest clay content of lithofacies analyzed in the Wolfcamp. Clay compositions in the argillaceous mudstone range from 41.5 to 52.5 wt.% (avg. 45.9 wt.%). Dolomite can be found in the argillaceous mudstone at an average of 12.2 wt.%. The argillaceous mudstone is found as a part of thin (inch-scale), fine-grained turbidite deposits. The green, argillaceous mudstone is characterized by high clay content, high porosities, very low permeabilities, and poor TOC. Porosity ranges from 7.4 to 12.1 percent (avg. 9.9 percent). Core permeability analyzed ranges from 0.1 to 4.1 nD (avg. 1.0 nD). The TOC of the argillaceous mudstone, the lowest of lithofacies examined, is on average 0.4 wt.%, ranging from 0.2 to 1.1 wt.%.

2.3 Facies Distribution

The facies distribution for the four facies groups and nine lithofacies can be found in Figure 2.6. To understand the changes in facies distribution, the facies group and lithofacies were plotted as a function of depth. The facies distribution was also quantified based on abundance for each Wolfcamp interval. The subsequent sections discuss the facies distribution seen in the Wolfcamp A, B, C, and D.

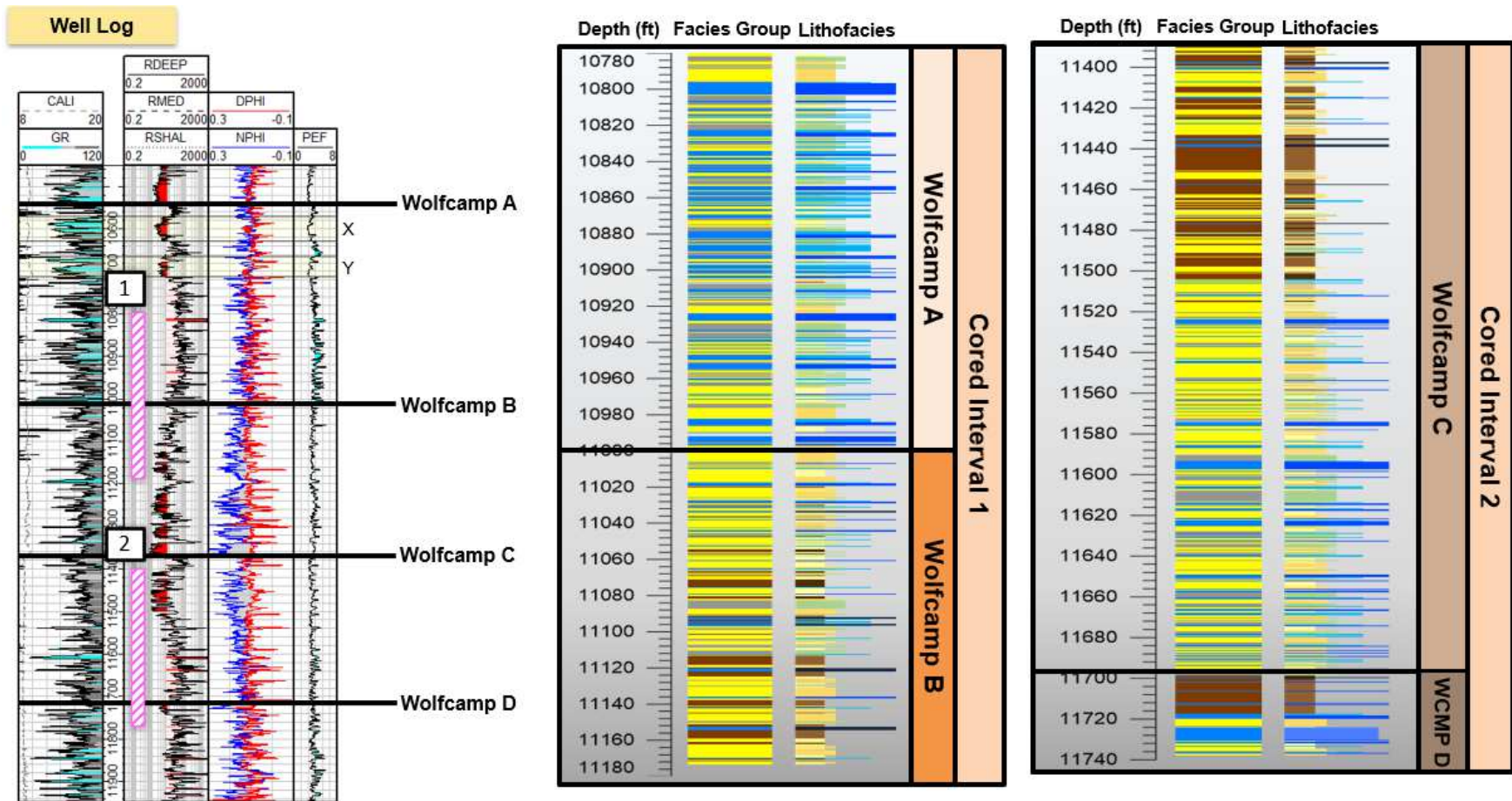


Figure 2.6—Facies distribution for the cored intervals of Wolfcamp A, B, C, and D. On the left, a normal well log suite of the Thunder C20-13 #2H is shown with the cored intervals noted as (1) and (2) in the pink rectangles. Facies distribution is shown to the right showing core depth, facies group, and lithofacies.

2.3.1 *Wolfcamp A*

The cored interval, equivalent to the lower 45.2 percent of the Wolfcamp A, was analyzed in this study. The Wolfcamp A is also referred to in the literature as the “Upper Wolfcamp Carbonate.” The Wolfcamp A consists of three facies groups—the calcareous facies group (38.5%), siliceous facies group (37.0%), and mixed facies group (24.5%). The Wolfcamp A interval is composed of the highest influx of carbonate material in the Wolfcamp Formation. The calcareous facies group is made up of calcite-rich lithofacies of packstones and calcareous siltstones. Wolfcamp A is characterized by cyclic, carbonate sediment gravity flow deposits, in which hybrid event beds (HEB) are most common. These event beds are seen in core as compositionally stratified, fining upward sequences with genetically related lithofacies. The base consists of coarser-grained skeletal packstone that fines upwards into a calcareous siltstone followed by finer-grained mixed and siliceous lithofacies (Fig. 2.7, HEB deposit shown in red arrow). As a result, the primary lithofacies that make up a majority of Wolfcamp A are related to carbonate sediment gravity flows.

The most abundant lithofacies found in the Wolfcamp A includes the following: packstone (18.0%), calcareous siltstone (20.7%), mixed calcareous silty mudstone (24.5%), carbonate-rich siliceous mudstone (17.8%), and siliceous mudstone (17.7%). Pervasive in the Wolfcamp A are fine-grained carbonates, calcareous siltstones, and calcareous mudstones interbedded with organic-rich, noncalcareous mudstone. The sediment source for the calcareous lithofacies is likely from the Central Basin Platform and surrounding shelf margins (Thompson et al., 2018; EIA, 2018). Organic-rich siliceous mudstone deposition seen capping or in-between event beds are deposits that suggest a return to background sedimentation. However, due to the cyclic and repeating cycles of sediment gravity flows, these interbedded noncalcareous mudstones were susceptible to being eroded by a subsequent cycle. Sediment gravity flows in Wolfcamp A can range from less than a foot to tens of feet thick. The high carbonate content and cyclic stacking of carbonate sediment gravity flows pervasive in the Wolfcamp A are consistent with the interpretation that these deposits occurred during a highstand, when the adjacent carbonate platforms were flooded. The flooded carbonate platforms allow for a greater influx and frequency of carbonate material to be deposited into the basin through sediment gravity flows.

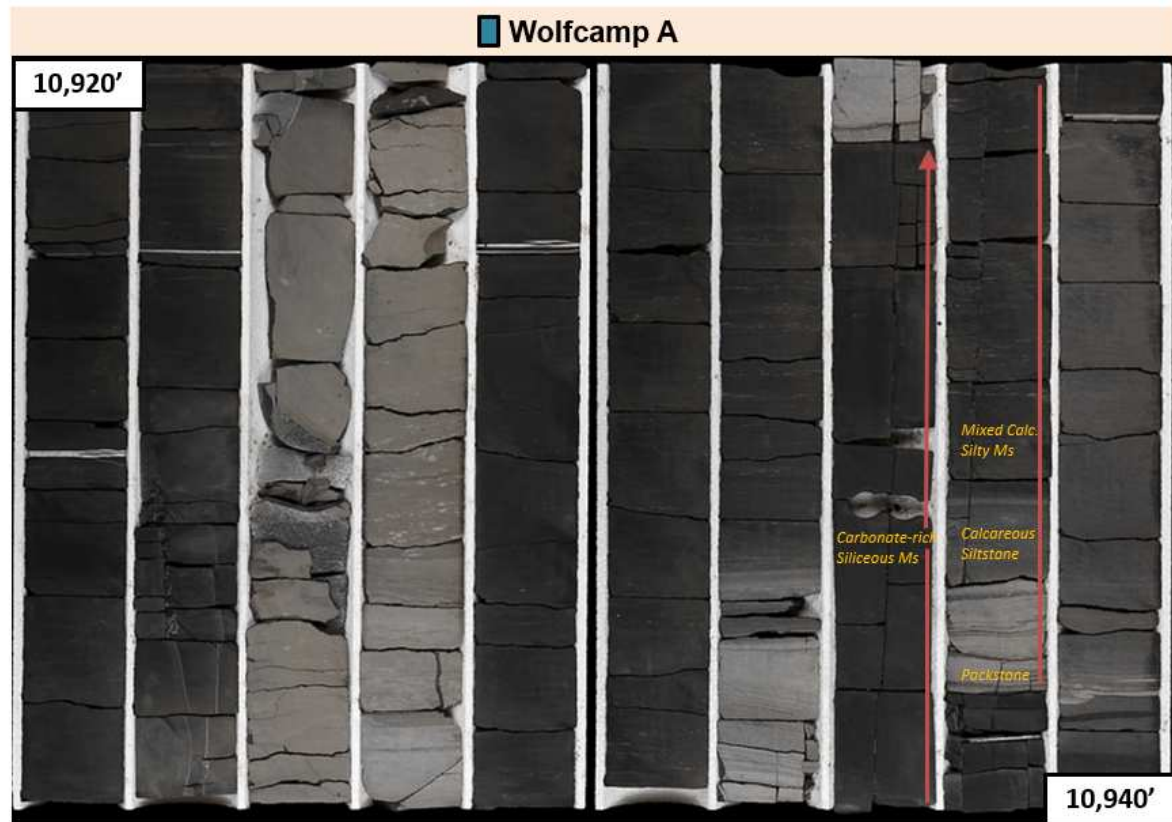
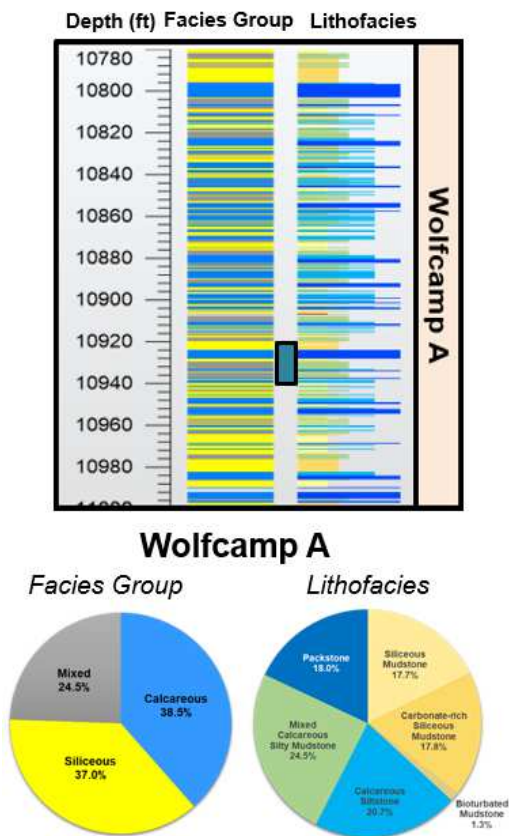
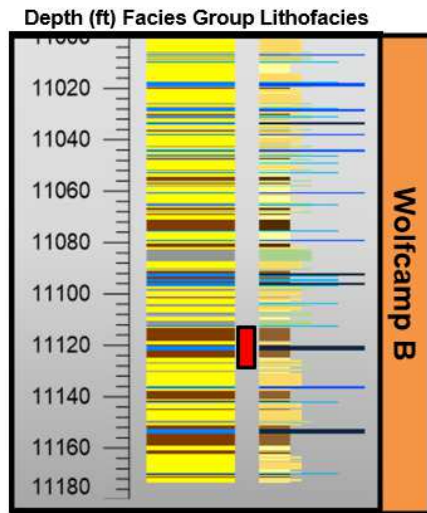


Figure 2.7—Wolfcamp A facies distribution and example of cored interval spanning 20 ft. The core depth, facies group, and lithofacies can be found on the left. The blue box is the cored example shown. Wolfcamp A is composed of the calcareous, siliceous, and mixed facies groups. Lithofacies associated Wolfcamp A are primarily the result of carbonate sediment gravity flows, predominantly hybrid event beds (HEBs). An example of one HEB deposit seen in the red arrow. The base of the HEB is a packstone bed (coarsest grain size, highest carbonate content) that fines upwards to a calcareous siltstone, mixed calcareous silty mudstone, and carbonate-rich siliceous mudstone. Wolfcamp A shows cyclic stacking of these fining upward sequences.

2.3.2 *Wolfcamp B*

The top 48.8 percent of Wolfcamp B, totaling 175.9 feet, was cored and evaluated for this study. Wolfcamp B is composed of the siliceous facies group (55.8%), argillaceous facies group (20.3%), mixed facies group (12.5%), and calcareous facies group (11.3%). Compared to Wolfcamp A, Wolfcamp B shows a significant decrease in carbonate-rich facies. The calcareous facies in Wolfcamp B is composed of packstone (4.2%), calcareous siltstone (4.1%), and dolostone (3.9%). The dolostone lithofacies, largely absent in Wolfcamp A, are distinct beds that fluoresce in Wolfcamp B. These massive dolostone beds are often found with the argillaceous mudstone. The argillaceous mudstone is also absent in Wolfcamp A. Some of the prominent lithofacies found in Wolfcamp B include the following: carbonate-rich siliceous mudstone (29.6%), argillaceous mudstone (19.3%), siliceous mudstone (19.3%), and mixed calcareous silty mudstone (12.6%).

The Wolfcamp B consists of thin, fine-grained, low-density turbidites that are abundant in the lower two-thirds of the cored interval (Fig. 2.8, fine-grained, low-density turbidite event beds shown in yellow arrows). The base of fine-grained turbidite cycles contains a thin, light gray, planar to ripple laminated siltstone that can range from 0.04 inches (1 mm) to several inches in thickness. These beds can also be absent. The base grades or can have a sharp contact with the overlying argillaceous mudstone lithofacies. The largely structureless argillaceous mudstone facies is characterized by high clay content, low permeability, and low TOC (less than 1 wt.%). A thin bed of dark gray, siliceous mudstone caps the cycle. Each one of these thin, fine-grained turbidite cycles can range from less than 1 inch to several inches in thickness. Carbonate sediment gravity flows can be found in the Wolfcamp B (Fig. 2.8, HEB deposit shown in the red arrow). However, in lower frequencies and smaller thicknesses compared to those in Wolfcamp A. The significant change between the carbonate-dominated Wolfcamp A to the siliciclastic-dominated Wolfcamp B is often interpreted to be due to changes in relative sea level (Handford and Loucks, 1993). Kvale and Rahman (2016) suggest the siliciclastic dominance could be related to river discharge during periods where the carbonate platforms were exposed, limiting carbonate deposition.



Wolfcamp B

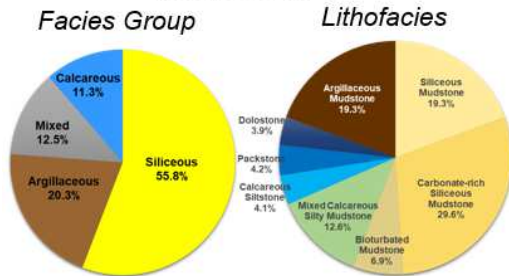


Figure 2.8—Wolfcamp B facies distribution and example of cored interval spanning 20 ft. The core depth, facies group, and lithofacies can be found on the left. Pie charts of the facies group and lithofacies distributions are seen below. The red box is the cored example shown. An example of one carbonate sediment gravity flow deposit is shown in the red arrow. Yellow arrows represent individual fine-grained turbidites associated with the argillaceous mudstone lithofacies. The brown star shows RCA location for argillaceous mudstone at 11,118 ft (LECO TOC 0.81 wt.%, porosity 10.0%, permeability 1.63 nD, and water saturation 74.9%). The yellow star shows RCA location for siliceous mudstone at 11,131 ft (LECO TOC 2.33 wt.%, porosity 9.3%, permeability 52.5 nD, and water saturation 55.5%).

2.3.3 *Wolfcamp C*

Over 300 feet (90%) of the Wolfcamp C was cored and examined for this study. Wolfcamp C is comprised of the siliceous facies group (47.1%), argillaceous facies group (20.0%), calcareous facies group (17.7%), and mixed facies group (15.2%). Lithofacies identified include the following: carbonate-rich siliceous mudstone (25.2%), argillaceous mudstone (20.0%), mixed calcareous silty mudstone (15.2%), siliceous mudstone (13.9%), packstone (9.0%), bioturbated siliceous mudstone (8.1%), calcareous siltstone (6.9%), dolostone (1.6%), and wackestone (0.2%). Based on the facies distribution, the Wolfcamp C can be subdivided into the Upper Wolfcamp C and Lower Wolfcamp C.

The Upper Wolfcamp C, the top one-third of the Wolfcamp C interval, is composed of argillaceous (52.5%), siliceous (35.5%), calcareous (10.8%), and mixed (1.1%) facies groups. From all cored intervals examined, the argillaceous mudstone lithofacies is most common in the Upper Wolfcamp C. Similar to the Wolfcamp B, the argillaceous mudstone was observed to be deposited in cyclic, fine-grained turbidites (Fig. 2.9). However, turbidites in the Wolfcamp C appear to be thinner on average. In logs, the upper clay-rich Wolfcamp C section shows distinctive log curve signatures with high gamma ray, low resistivity, and large porosity separation.

The Lower Wolfcamp C, the basal two-thirds of the Wolfcamp C, differs in the type of facies observed compared to the Upper Wolfcamp C. The lower Wolfcamp C is composed of siliceous (53.3%), mixed (22.7%), calcareous (21.3%), and argillaceous (2.7%) facies groups. The argillaceous mudstone that was a primary lithofacies in the Upper Wolfcamp C only accounts for 2.7 percent of the facies distribution observed in the lower two-thirds of Wolfcamp C. Lower Wolfcamp C is primarily composed of the carbonate-rich siliceous mudstone (27.7%), mixed calcareous silty mudstone (22.7%), siliceous mudstone (19.0%), packstone (12.2%), calcareous siltstone (8.2%), and bioturbated siliceous mudstone (6.5%). Minor argillaceous mudstone, dolostone, and wackestone were observed accounting for less than 4 percent of lithofacies analyzed. The type of lithofacies and stacking patterns observed in the Lower Wolfcamp C are most similar to those observed in Wolfcamp A (Fig. 2.7).

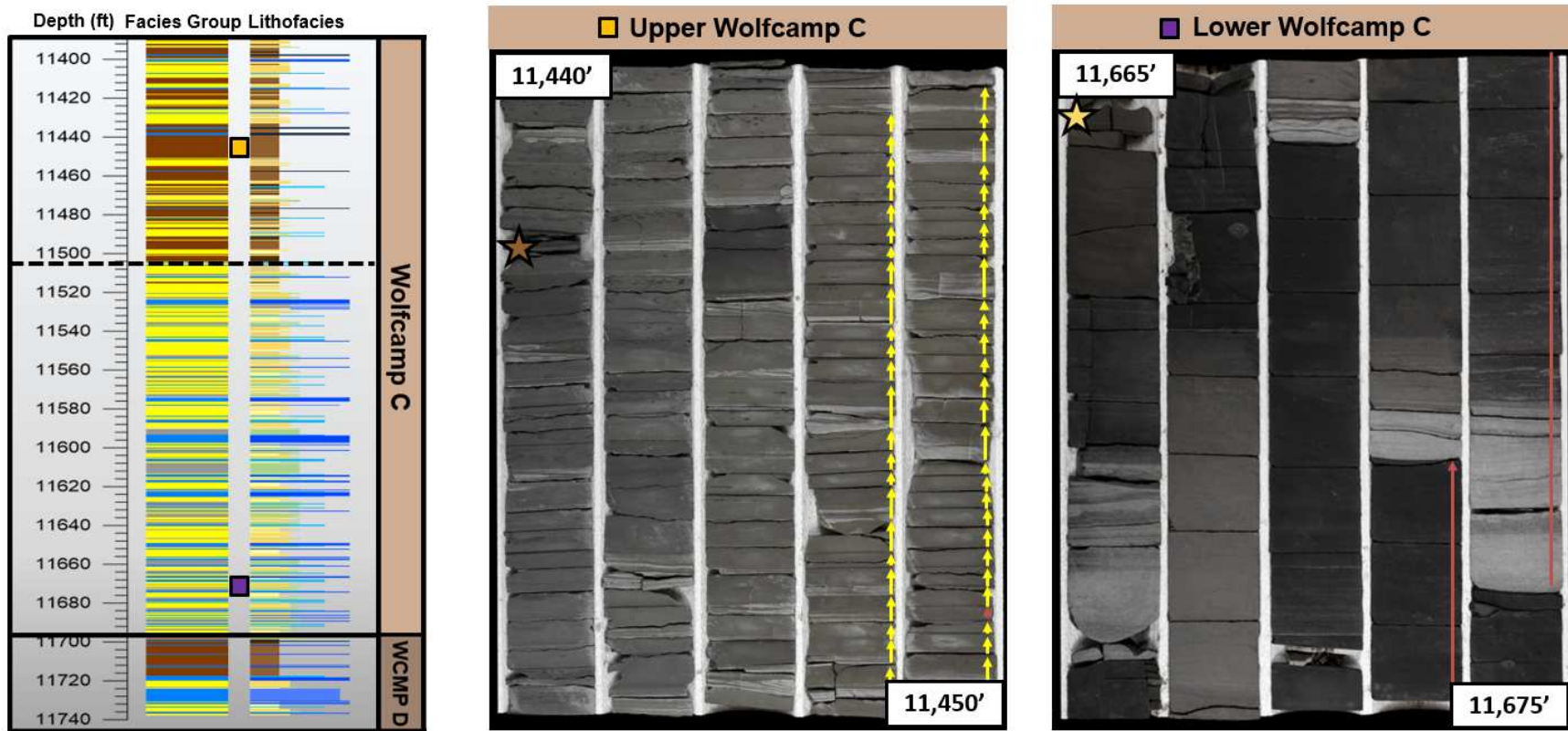


Figure 2.9—Wolfcamp C facies distribution and examples of core from Upper Wolfcamp C and Lower Wolfcamp C, spanning 10 ft each. The core depth, facies group, and lithofacies can be found on the left. An example of one carbonate sediment gravity flow deposit is shown in the red arrow from the Lower Wolfcamp C. The yellow arrows represent individual fine-grained turbidites associated with the argillaceous mudstone lithofacies from Upper Wolfcamp C. The brown star shows RCA location for argillaceous mudstone at 11,440.5 ft (LECO TOC 0.16 wt.%, porosity 11.5%, permeability 0.7 nD, and water saturation 86.4%). The yellow star shows RCA location for carbonate-rich siliceous mudstone at 11,665 ft (LECO TOC 2.15 wt.%, porosity 7.9%, permeability 71.9 nD, and water saturation 32.6%).

2.3.4 *Wolfcamp D*

The top 36.7 feet of the Wolfcamp D was cored and evaluated for this study. The cored interval is comprised of the argillaceous (39.3%), calcareous (35.1%), siliceous (23.4%), and mixed (2.1%) facies groups. Lithofacies include the following: argillaceous mudstone (39.3%), wackestone (16.1%), carbonate-rich siliceous mudstone (15.4%), packstone (13.7%), siliceous mudstone (8.1%), calcareous siltstone (5.3%), and mixed calcareous silty mudstone (2.1%). Analysis of core available showed deposition of siliciclastic and carbonate lithofacies (Fig. 2.10). The base of the Wolfcamp D cored interval consists of calcareous lithofacies, including wackestones, packstones, siltstones, carbonate-rich siliceous mudstones, calcareous siltstones, and noncalcareous siliceous mudstones. Debris flows consisting of wackestone were observed in the carbonate-rich section along with other carbonate sediment gravity flows. Wackestone and packstone beds appear massive with visible skeletal allochem fragments. Elongated mudstone rip up clasts were present within the wackestone lithofacies. The top of the Wolfcamp D cored interval consists of argillaceous mudstones, packstones, and calcareous siltstones. Similar lithofacies were noted by Hennenfent and others (2015) who described the base of the Wolfcamp D as containing polymictic breccias that fine upwards to a massive skeletal packstone, laminated wackestone, and organic-rich silty mudstone containing beef fractures.

Due to the small cored interval from the Thunder C20-13 #2H well, a thorough investigation of the lithofacies distribution representative of the whole Wolfcamp D interval could not be made. Descriptions of lithofacies and facies associations of the Wolfcamp D in the Delaware and Midland basins are available from various sources in the literature (Jacobs, 2013; McGlue and Baldwin, 2015; Hennenfent et al., 2015; Perlman, 2017; Waite et al., 2019). The Wolfcamp D is the base of the Wolfcamp Formation that unconformably overlies the Cisco clastics or Strawn carbonates (Hennenfent et al., 2015). The Wolfcamp D was deposited during the Late Pennsylvanian to Early Permian (Wolfcampian) time. Icehouse conditions prevailed and ice sheets began to wane, transitioning gradually towards greenhouse conditions by the Late Wolfcampian (Waite et al., 2019).

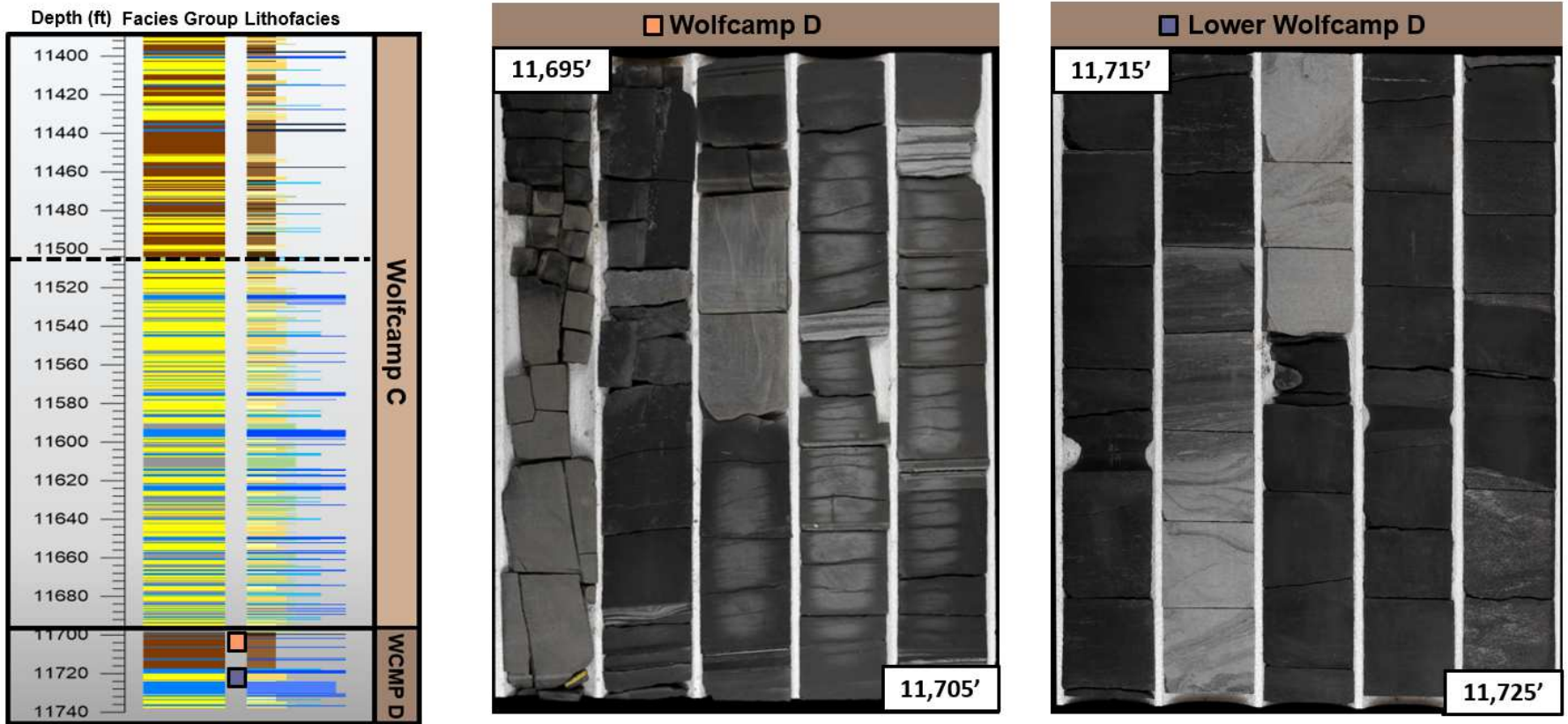


Figure 2.10—Wolfcamp D facies distribution and example of two cored intervals, spanning 10 ft each. The core depth, facies group, and lithofacies can be found on the left. The top 36.7 ft of Wolfcamp D was cored and examined for this study. The Wolfcamp D cored interval shows both siliciclastic- and carbonate-dominated lithofacies.

2.4 Depositional Processes

Recent studies investigating Wolfcamp depositional processes most often use a combination or modification of classical deepwater depositional classifications, such as Bouma (1962), Lowe (1982), Middleton and Hampton (1973), and Haughton and others (2009), among other literature. Beginning in the Pennsylvanian Desmonian time, around 312 Ma, the rate of subsidence in the Delaware Basin exceeded the rate of carbonate and siliciclastic deposition. This resulted in further subsidence of a deepwater basin attached to shallow-water carbonate platforms through a structurally steepened ramp (Kvale et al., 2020). Subsidence proceeded during Wolfcamp deposition. Paleowater depths were estimated to have increased from 1,000 ft in the Early Wolfcampian time to over 1,500 ft in the Late Wolfcampian with a slope gradient of over 7 degrees based on outcrop studies (Hill, 1984; Playton and Kerans, 2002; Kvale et al., 2020).

As tectonic subsidence and movement proceeded, repeating platform and shelf-edge failure resulted in the transportation of shallow-water carbonate detritus down ramps into the basin. As a result, the Wolfcamp consists of deposits of mass movement and sediment gravity flows. The deposition of the Wolfcamp Formation is dominated by series of carbonate- and siliciclastic-sediment gravity flows and mass transport deposits with intermittent background sedimentation. Sediment gravity flows can transport large quantities of carbonate debris and mud into the deepwater (Boggs, 2001). Wolfcamp sediment gravity flows have been estimated to flow considerable distances basinward ranging from 25 to 34 miles, from origin to distal terminus (Hobson et al., 1985; Morgan et al., 1996; Kvale et al., 2020). Furthermore, multiple sediment sources resulted in a complex and heterolithic arrangement of strata. Haughton and others (2009) proposed a classification for sediment gravity flows based on flow behavior and dominant sediment-support mechanism. Debrites, deposited from debris flows, exhibit cohesive, laminar flow behavior. The other end members are turbidites deposited by non-cohesive, turbulent flows. Intermediate, composite flows include hybrid event beds (HEBs) that show both cohesive, laminar flow behavior and non-cohesive, turbulent flow behavior within a single flow.

The four most common depositional processes identified from core are the following:

1. Hemipelagic/Background Sedimentation
2. Debris Flows
3. Hybrid Event Beds (HEBs)
4. Fine-grained, Low-density Turbidity Flows

2.4.1 Hemipelagic/Background Sedimentation

Hemipelagic deposits, or hemipelagites, are formed through a process involving the vertical settling of fine-grained sediments through the water column with very low current velocities and limited lateral transport (Pickering and Hiscott, 2016). The two primary sediment transport mechanisms are (1) suspension settling and (2) reworking from weak, diluted bottom currents. The accumulation of hemipelagic deposits can occur on the slope or basin floor settings (Boggs, 2001). Hemipelagites represent a return to low energy conditions. Background sedimentation has slower sediment accumulation rates compared to other depositional processes discussed. Deposits from hemipelagic settling are characteristically poorly laminated to structureless. These deposits can be bioturbated, in the case where sediment deposited by hemipelagic processes is reworked by burrowing organisms. The mud cap of a waning flow from a hybrid event bed (H5 division) or turbidity current (Te) both represents the muddy tail ends of a waning flow where suspension settling occurs at the wake of the flow. Mud caps to these sediment gravity flows are usually thin (inch-scale). Packages thicker than a few inches may include background sedimentation or hemipelagic settling from other distal events (Kvale et al., 2020). These deposits represent a return to low energy, slow sedimentation conditions. An example of a hemipelagic, background deposit can be seen in Figure 2.11.

Three lithofacies within this facies association are the siliceous mudstone, bioturbated siliceous mudstone, and carbonate-rich siliceous mudstone. The base of the deposit shows slightly higher energy that decreases to the top. All three lithofacies have very small grain sizes ranging from clay- to fine silt-sized (0.12 to 7.8 μm) and are commonly structureless. These features are consistent with deposits from a persistently low energy setting. While these deposits are often structureless, faint, thin (mm-scale) laminations of alternating clay-

and silt-sized laminae can be found. This suggests possible influences from weak, bottom currents. Ichnofossil traces from the bioturbated siliceous mudstone are consistent with deepwater traces. Bioturbation found in these deposits suggests that there were periods of time with oxygen available and intermittent periods of slow sediment accumulation rates for benthic communities to develop. Deposits associated with hemipelagic/background sedimentation can be found throughout the Wolfcamp Formation in all four Wolfcamp intervals, showing deposition with changes in fluctuating sea levels. These fine mudstones likely originated as unconsolidated muds that were eroded from the slope or basin floor. Sediment gravity flows then incorporate these muds into the flow, transporting them into the basin (Kvale et al., 2020).

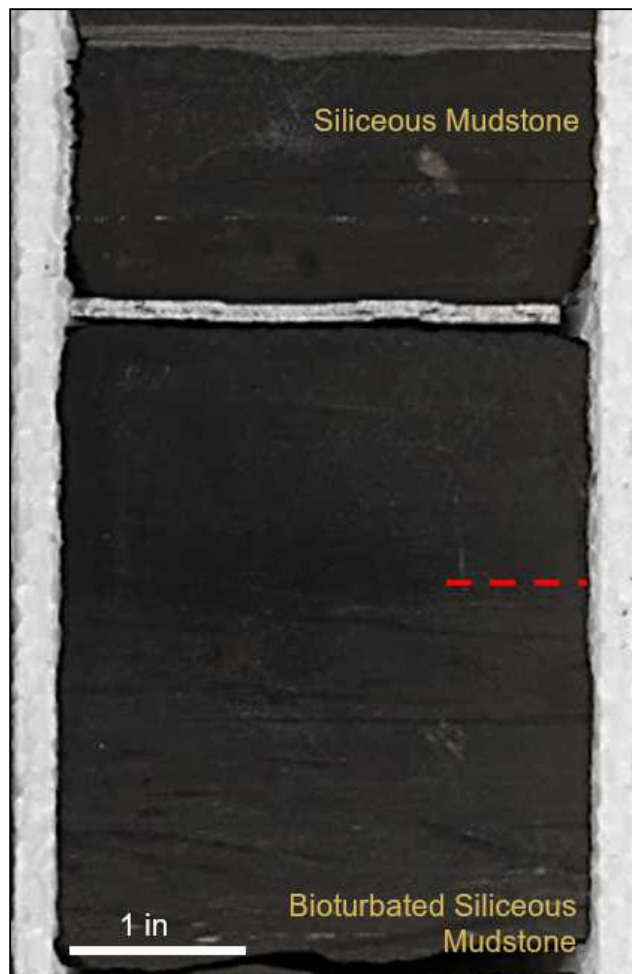


Figure 2.11— Core photo illustrating a hemipelagic facies association illustrating facies stacking pattern of a bioturbated siliceous mudstone with an overlying siliceous mudstone from 10,906 ft. The bioturbated mudstone marks the end of an underlying sediment gravity flow event into a period of lower energy, slow sediment accumulation rate.

2.4.2 Debris Flows

Debris flows are characterized by cohesive, laminar flow behavior (Haughton et al., 2009). Debris flow deposits (debrites) exhibit poorly-sorted intraclasts supported by a cohesive, finer-grained matrix of mud and interstitial water (Middleton and Hampton, 1973). Debris flows are slurry-like flows that must overcome a yield strength to initiate flow. When the flow reaches a critical point and cannot exceed the yield strength, the flow stops creating an *en masse* deposit. Debris flow deposits have several characteristics that distinguish them from other mass transport deposits and sediment gravity flows (Fig. 2.12). The wackestone lithofacies were interpreted to meet the characteristics prevalent in this facies association.

Intraclasts in the Wolfcamp debris flows of the wackestone lithofacies are allochthonous carbonate fragments containing shallow-shelf microfossils. These fragments range from silt- to granular-sized bioclasts with microfossil assemblages that include crinoids, sponge spicules, brachiopods, fusulinids, and other shelfal fossil fragments. The presence of shallow-water biota indicates that wackestones likely originated from shallow-water shelf margins. Grains within the debris flows are chaotically arranged and have a range of grain sizes. These intraclasts show no preferred orientation or poor grading. Talling (2012) attributes weak normal grading to seawater mixed into the flow that can reduce the cohesive strength at the top of the flow. Elongated mud rip up clasts are common in these deposits and are composed of dark gray, calcareous to noncalcareous mudstone. Debris flow deposits have sharp basal and upper contacts that can be parallel or nonparallel to bedding. The dark gray mudstones that commonly overlie these deposits are interpreted to be background sedimentation or sediment from a distant, waning flow. The grain size of intraclasts in debris flow deposits are largest (up to boulder-sized) in proximal locations to the basin margins and decreases in more distal positions of the fan (Boggs, 2001). Paraconglomerates, also called carbonate breccias and conglomerates, that consist of granule- to boulder-sized carbonate bioclasts in a wackestone matrix have been reported and interpreted to be debris flow deposits in the Wolfcamp (Baumgardner et al., 2016; Kvale et al., 2020).

No paraconglomerates were observed in the cored intervals for this study. Wackestones that are present in core are likely the distal, fine-grained equivalents to the calcareous paraconglomerates and breccias from proximal settings. Compared to paraconglomerates, wackestone deposits have smaller clast sizes and are more clay matrix-dominated. They are interpreted to be low- to medium-cohesive strength flows. Debris flow deposits were not as commonly found in the cored intervals provided for this study in comparison to other facies associations. They are most often found above sequence boundaries, in which their occurrence represents the collapse of an adjacent carbonate platform. However, shelf instability can occur during highstands and lowstands (Thompson et al., 2018).



Figure 2.12—Core photo of a debris flow deposit from 11,578 ft illustrating key architectural elements including (1) sharp basal contact, (2) chaotically arranged intraclasts, (3) subangular, poorly sorted grains, and (4) clast protrusion. The dark gray mudstone that overlies the debrite is interpreted to be the equivalent of a Te bed, likely background sedimentation or sediment from a distant, waning flow.

2.4.3 Hybrid Event Beds (HEBs)

Hybrid event beds, or HEBs, are an intermediate, composite flow that shows both cohesive, laminar flow behavior and non-cohesive, turbulent behavior within a single flow. Siliciclastic HEBs were proposed by Haughton and others (2009) to describe flows that transport sediment in siliciclastic deepwater fans. An idealized HEB has five divisions (H1 through H5) that each represent a change to the flow regime. The H1 division at the base is composed of coarse-grained sandstone that can be structureless to laminated. Mud clasts and dewatering features are common sedimentary structures. The H1 division shows poorly cohesive, turbulent flow equivalents to a high-density turbidite. The H2 division is interpreted to be the transitional part of the flow that shows alternating lighter sands with darker, more clay-rich sands. Dewatering features are common in the H2 division. The H3 division, also referred to as a linked debrite, shows cohesive, debris flow-like characteristics. The H3 division is described as sand-specked muddy sand with features including mud clasts, outsized granules, and sand injections from the underlying layer. Mud clasts in the H3 division are common in some systems and absent in others. The H4 division is composed of a thin, graded, fine-grained sandstone showing planar, parallel, and ripple cross laminations. The H4 division is interpreted to represent traction from a trailing, low-density turbulent wake. Lastly, the H5 division represents mud from suspension fallout (Haughton et al., 2009).

Recent studies (Kvale and Rhaman, 2016; Kvale et al., 2020) have applied HEB divisions from siliciclastic systems to the mixed carbonate-siliciclastic system of the Wolfcamp Formation. Instead of quartz sand, Wolfcamp HEBs are composed of allochthonous carbonate packstones in their H1 division, and the carbonate content decreases as the Wolfcamp HEB fines upwards. Kvale and others (2020) proposed a modified version of Haughton and others (2009) divisions specifically for the Wolfcamp HEBs (Fig. 2.13). Carbonate HEBs are commonly found throughout the Wolfcamp Formation but occur most frequently in the “Upper Wolfcamp Carbonate” in the Wolfcamp A. Lithofacies associated with HEBs include skeletal packstone, calcareous siltstones, mixed calcareous silty mudstones, carbonate-rich mudstones, and siliceous mudstones (Fig. 2.14).

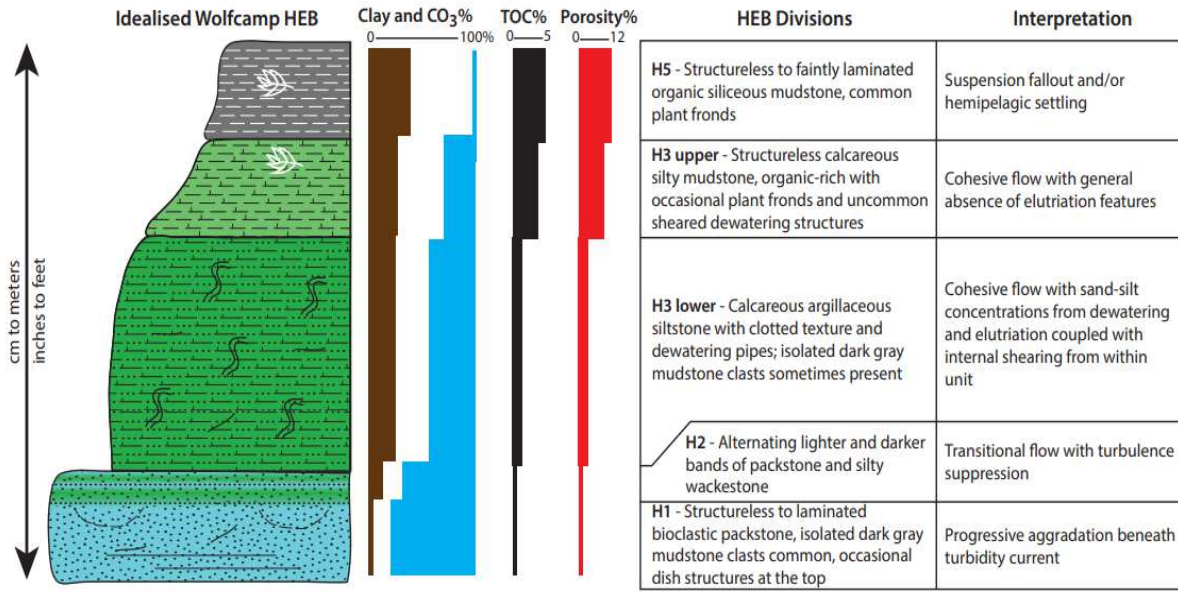


Figure 2.13—Idealized Wolfcamp hybrid event bed deposit (Kvale et al., 2020).

The skeletal packstone lithofacies resembles the H1 and H2 divisions noted by Haughton and others (2009) and Kvale and others (2020). The skeletal packstone lithofacies is composed of very fine to fine sand-sized grains (62.5 to 125 μm) of skeletal, shallow-water shelf allochems. The skeletal packstone is usually the base of the HEBs in this study. Skeletal packstones have several characteristics: (1) massive to laminated, (2) elongated mud clasts, (3) slightly erosive basal contact, (4) normal grading, and (5) dewatering features, such as convoluted bedding and flame structures. At the top of the packstone beds, banding of alternating light packstone to calcareous siltstone can be seen, resembling the H2 division. The H2 division is interpreted to be the transitional flow from non-cohesive, turbulent flow to cohesive, laminar flow. Kvale and others (2020) subdivided the H3 division of the Wolfcamp into a lower H3 (H3l) and an upper H3 (H3u). The calcareous siltstone, often found overlying the skeletal packstone, is a massive siltstone with fluid escape structures that produce a unique “clotted” texture not found in other facies. The calcareous siltstone corresponds to characteristics found in the H3l division and is interpreted to represent part of the cohesive, laminar flow in an HEB. Mud clasts that were described in Haughton and others (2009) were not found in the calcareous siltstones in this study. The calcareous siltstones can have a sharp or graded upper contact to the mixed calcareous silty mudstones or carbonate-rich siliceous mudstones.

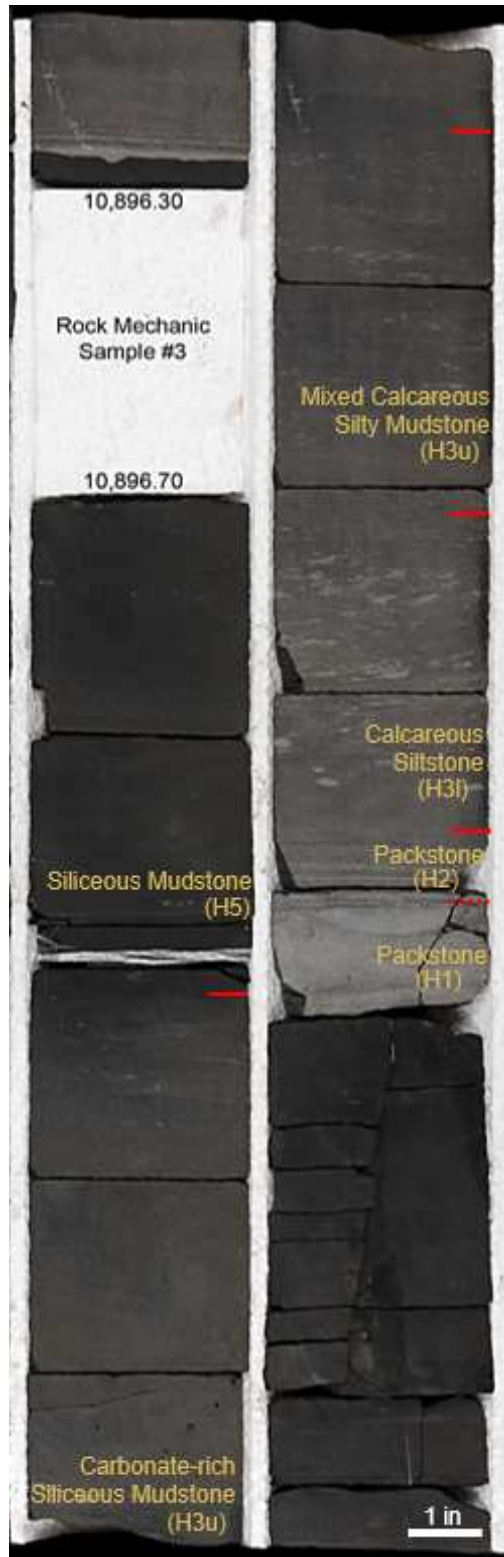


Figure 2.14— Core photo (from 10,896 to 10,900 ft) with annotations for a single flow, fining upwards hybrid event bed (HEB) deposit. Illustrated are the lithofacies and corresponding HEB division based on the HEB components described by Kvale and others (2020).

The mixed calcareous silty mudstones contain small, elongated concentrations of silt-sized grains that can be seen in core. Similar structures have been interpreted in siliciclastic muddy debris flows, described to be the result of dewatering (Haughton et al., 2009). As the cohesive flow decelerates, dewatering and compaction occur. Finer grains, including clays, are elutriated and concentrations of silt remain. The mixed calcareous silty mudstones often fines into a massive, carbonate-rich siliceous mudstone. The carbonate-rich siliceous mudstones have lower silt concentrations as the event bed fines upwards. The carbonate-rich siliceous mudstone bed is slightly darker in color compared to the mixed calcareous silty mudstone bed, likely due to the higher clay and lower carbonate content. The siliceous mudstone bed is equivalent to the H5 division. The siliceous mudstone bed is a noncalcareous, massive to faintly laminated mudstone that is interpreted to represent the final mud settling from suspension in the wake of the flow. The Wolfcamp HEBs range in thickness from a few inches to tens of feet in thickness. While complete HEBs are observed in core, incomplete successions are abundant. The Wolfcamp sediment gravity flows observed in this study, more often show characteristics of carbonate HEBs proposed by Kvale and others (2020) rather than the calciturbidites in other studies. Most carbonate HEBs show muddier calcareous siltstones and mixed calcareous silty mudstones, interpreted to be the cohesive portion of the flow that would otherwise be absent in the traditional Bouma sequence (1962).

2.4.4 Fine-grained, Low-density Turbidity Flows

Low-density turbidites are primarily composed of clay, silt, and fine to medium sand-sized grains (Lowe, 1982). Low-density turbidite deposits correspond to the finer-grained regime of the Bouma sequence (1962) and are composed of the Tc, Td, and Te divisions. Low-density turbidites have the following: (1) the Tc bed of fine-grained, ripple laminated base, (2) Td division that consists of parallel laminated siltstone, and (3) Te bed of massive, ungraded mudstone. Low-density turbidites observed in the Wolfcamp most often have three components: (1) the Tc base of coarser-grained, normally graded, yellow-gray siltstone with ripple to planar laminations, (2) the Td division of laminated to massive, green-colored argillaceous mudstone, and (3) the Te mud cap of massive, siliceous mudstone (Fig. 2.15). The green argillaceous mudstone in the Td division that makes up

the bulk of the flow, has a high clay content and exhibits very low permeabilities, very low TOC, and high water saturation. The mudstone cap from the siliceous mudstone is often very thin (sub-inch in thickness) with higher TOC. Prior studies (Kvale and Rahman, 2018) have shown that finer-grained, siliciclastic turbidites typically have TOC values of less than 1 wt.%, which is consistent with core analysis from this study. The carbonate HEBs and calciturbidites are sourced from the Central Basin Platform. However, the siliciclastic turbidites are interpreted to be derived from a west-northwest source, like the siliciclastic turbidites of the Bone Spring Formation (Thompson et al., 2018; U.S. Energy Information Administration, 2018).

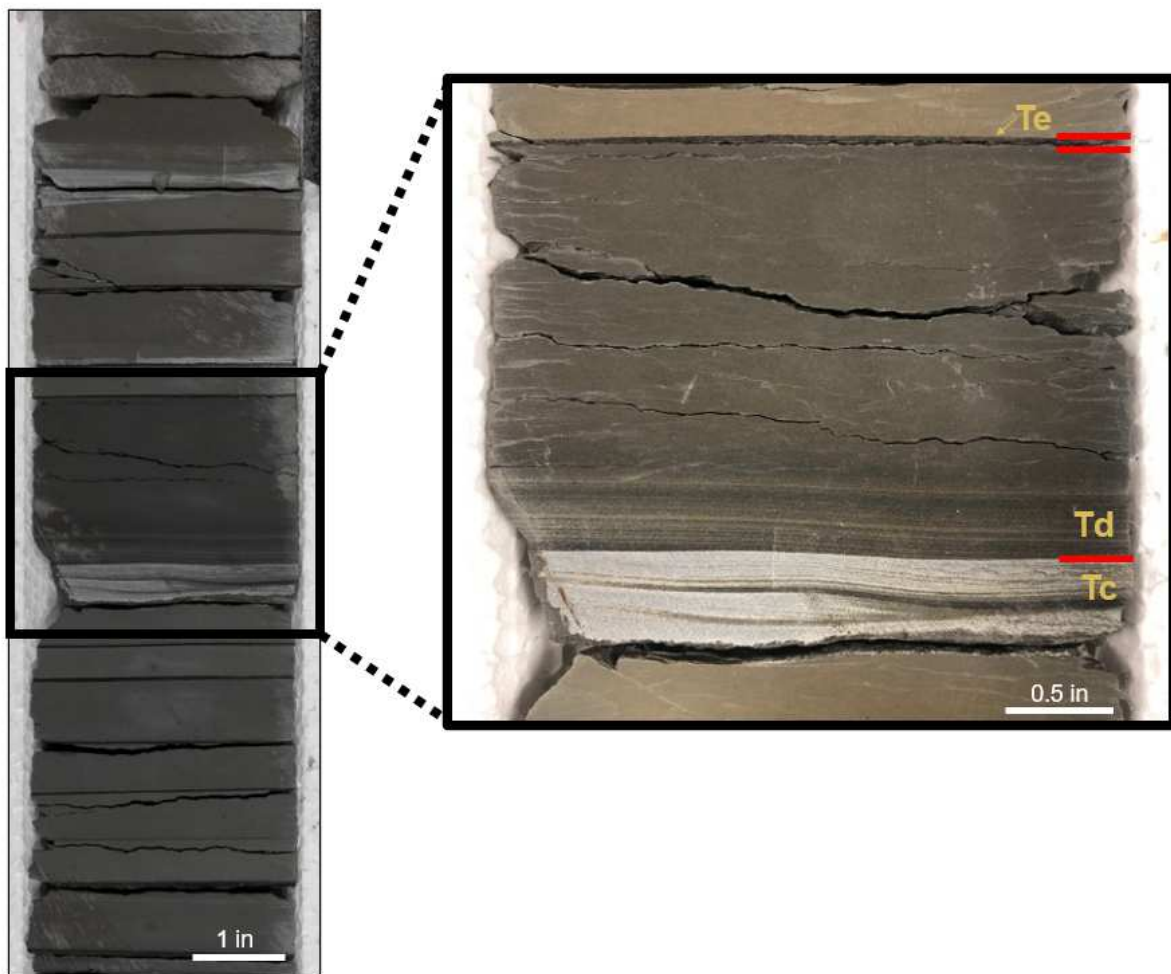


Figure 2.15— Core photo (from 11,450 to 11,451 ft) showing cyclic, low-density turbidite deposits. The enlarged core photo to the right shows a single fine-grained, low-density, turbidite deposit. The basal Tc is a ripple laminated fine-grained siltstone. The Td bed is a laminated to massive argillaceous mudstone. The Te division is the mud cap comprised of a massive, siliceous mudstone. Mud caps are very thin, often 0.04 inches (1 mm) or less.

CHAPTER 3: ELEMENTAL GEOCHEMISTRY

Elemental geochemistry analyzes major and trace elements to understand the geochemical components of sediments. Elemental data, obtained from X-ray Fluorescence (XRF), was analyzed using available data for the Wolfcamp A and B. There are many applications in analyzing chemical variations in stratigraphic intervals. First, elemental abundances can be modeled to predict mineralogy using stoichiometric relationships. As seen from compositional analysis, positive relationships observed between elements of silicon (Si), calcium (Ca), and potassium (K) to minerals quartz, calcite, and illite show that these elements can be used as mineral proxies. A mineral model used to calculate quartz, calcite, and illite using these elements was applied to the XRF dataset to evaluate changes in lithology for the Wolfcamp intervals. Other applications for XRF include utilizing statistical methods to define chemofacies with similar elemental signatures. High-resolution elemental data can also be used for calculating a synthetic gamma ray, which can then be compared to the wireline gamma ray. The synthetic gamma ray can produce a more realistic gamma ray profile that captures beds that are below the logging tool resolution. Finally, elemental indicators for terrestrial flux, carbonate flux, and paleoredox conditions were investigated based on elemental concentrations throughout the Wolfcamp A and B. These analyses are described within this chapter.

3.1 Mineral Model

In unconventional reservoirs dominantly composed of very fine-grained sediment, compositions can be difficult to discern based on visual inspection of core. Mineral components are quantified using X-ray Diffraction (XRD), which is an essential reservoir characterization technique. However, XRD sampling is more expensive and, therefore, often poorly sampled. The gaps between sampling locations are often too coarse to capture variations in highly heterogeneous strata, including the Wolfcamp. The cored section of the Wolfcamp A and B has 391.4 ft of core, in which 33 XRD samples were analyzed to provide mineralogical data. The same interval contains 799 measurements for XRF elemental data. An element-to-mineral model proposed by Nance and Rowe (2015) was

applied to the XRF dataset to understand mineralogical changes in the Wolfcamp Formation.

The mineral model uses XRF elemental data to approximate mineral components based on stoichiometric relationships. From compositional analysis for all XRD samples (n=67), 67 percent of the samples, on average, are composed of three minerals—quartz (SiO₂), calcite (CaCO₃), and illite [K_{0.8}Al₂[Al_{0.8}Si_{3.2}O₁₀](OH)₂]. The mineral model uses the elements Ca, K, and Si from XRF to determine the relative proportions of calcite, illite, and quartz. Detailed steps for the calculations and background on this mineral model method can be found in Nance and Rowe (2015) and summarized here.

First, XRF elemental data is converted from parts per million (ppm) into weight percent (wt.%) for Si, Ca, and K. Beginning with calcite, Ca is 40 percent of CaCO₃. Therefore, the percentage of calcite based on stoichiometry is as seen below:

$$Calcite_{wt\%} = \left(\frac{1}{0.40}\right) * Ca_{wt\%} = 2.5 * Ca_{wt\%} \quad (3.1)$$

K is on average 6.03 percent of illite (Nesse, 2013). The equation for using K to calculate for illite is the following:

$$Illite_{wt\%} = \left(\frac{1}{0.0603}\right) * K_{wt\%} = 16.58 * K_{wt\%} \quad (3.2)$$

Since Si is a key element in both illite and quartz, Si must be differentiated between the two minerals. Si is, on average, 25.25 percent of illite. Therefore, the proportion of Si in illite can be calculated as follows:

$$Si_{illite_{wt\%}} = \left(\frac{1}{0.2525}\right) * Illite_{wt\%} = 3.96 * Illite_{wt\%} \quad (3.3)$$

The proportion of Si found in quartz can be calculated by:

$$Si_{quartz_{wt\%}} = Si_{total_{wt\%}} - Si_{illite_{wt\%}} \quad (3.4)$$

Si is 47 percent of quartz (SiO₂). To calculate the percentage of quartz, the following equation is used:

$$Quartz_{wt\%} = \left(\frac{1}{0.47}\right) * Si_{quartz_{wt\%}} = 2.14 * Si_{quartz_{wt\%}} \quad (3.5)$$

Finally, the three calculated mineral proportions for calcite, illite, and quartz are normalized, as seen in the following:

$$Total_{wt\%} = Calcite_{wt\%} + Illite_{wt\%} + Quartz_{wt\%} \quad (3.6)$$

$$Calcite_{normalized_{wt\%}} = \frac{Calcite_{wt\%}}{Total_{wt\%}} \quad (3.7)$$

$$Illite_{normalized_{wt\%}} = \frac{Illite_{wt\%}}{Total_{wt\%}} \quad (3.8)$$

$$Quartz_{normalized_{wt\%}} = \frac{Quartz_{wt\%}}{Total_{wt\%}} \quad (3.9)$$

These calculations were applied to the XRF dataset, resulting in normalized portions of quartz, calcite, and illite throughout Wolfcamp A and B. These proportions were plotted as a function of depth, illustrating changes in these three key minerals (Fig. 3.1). The modeled results were compared to facies group and lithofacies determined from core description as well as mineral components from XRD. The XRF mineral model implemented in Wolfcamp A and B aligns very well to the corresponding lithofacies noted from core. Furthermore, the mineral model also contrasts the difference in mineral proportions that vary significantly between the more carbonate-rich Wolfcamp A and the more siliciclastic-dominated Wolfcamp B.

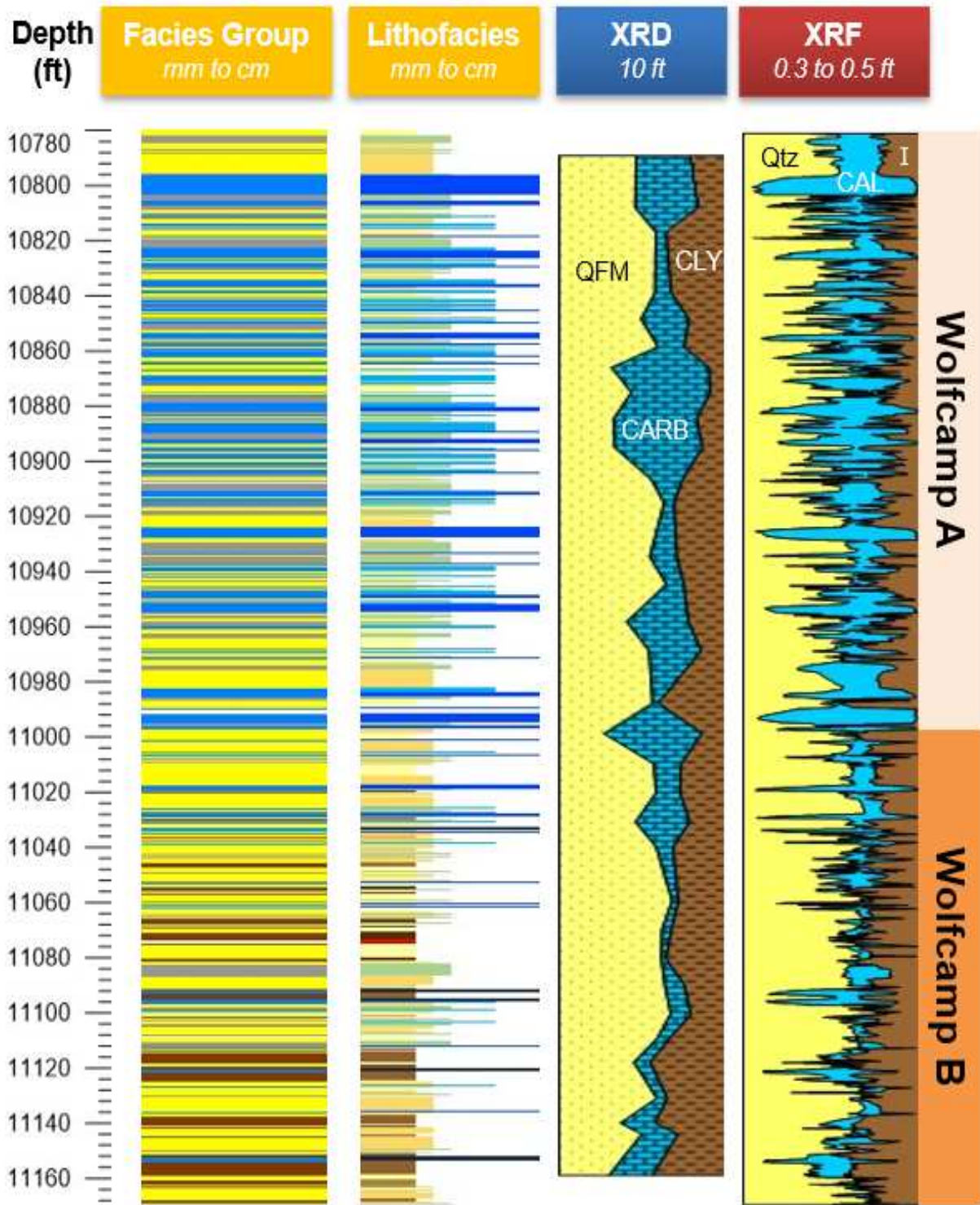


Figure 3.1—Lithology logs showing (1) facies group from core description, (2) lithofacies from core description, (3) XRD normalized abundances of total QFM, carbonates (CARB), and clays (CLY), and (4) XRF mineral model calculated abundances for normalized quartz (Qtz), calcite (CAL), and illite (I).

3.2 Principal Component Analysis (PCA)

XRF is beneficial in providing large quantities of elemental data at high sampling resolutions. For each measurement (n=799), 41 elements are detected, including Ag, Al, As, Au, Ba, Bal, Bi, Ca, Cd, Ce, Cl, Co, Cr, Cu, Fe, K, La, Mg, Mn, Mo, Nb, Nd, Ni, P, Pb, Pr, Rb, S, Sb, Se, Si, Sn, Sr, Th, Ti, U, V, W, Y, Zn, and Zr. The proportions of these elements frequently change due to the heterolithic arrangement of strata. Conventionally chemostratigraphic workflows involve plotting 250 to 300 elemental profiles (elements and elemental ratios by depth) for each study (Michael and Craigie, 2021). While elemental profiles and crossplots are still very useful, one method to process the vast amounts of data is to use principal component analysis (PCA). PCA is a statistical tool that reduces the dimensionality of large datasets into a 2D graph, making it easier to determine elemental relationships when applied to the XRF dataset. On the 2D graph, cells that are highly correlated to one another form “clusters” and are spaced closely to one another. PCA was completed using the Unistat software for the dataset. Figures 3.2 and 3.3 show the results from PCA for the Wolfcamp A and B, respectively.

In the Wolfcamp A (Fig. 3.2), three main clusters are seen for elements that are strongly correlated to one another. The first group includes calcium (Ca) and strontium (Sr), which are both carbonate elemental indicators. Magnesium (Mg), another carbonate elemental indicator, shows the lack of a relationship to Ca and Sr in the Wolfcamp A. Another group of elements that form the second cluster, showing close associations, are terrigenous and paleoredox-sensitive elemental indicators. Terrigenous minerals include quartz, feldspars, and clay minerals. Elemental proxies for terrigenous minerals include silicon (Si), aluminum (Al), potassium (K), titanium (Ti), rubidium (Rb), and zirconium (Zr). These terrestrial indicators in the Wolfcamp A, cluster together along with paleoredox-sensitive elements such as zinc (Zn), molybdenum (Mo), uranium (U), lead (Pb), iron (Fe), niobium (Nb), and chromium (Cr). The third group includes rare-earth elements of neodymium (Nd), praseodymium (Pr), lanthanum (La), and cerium (Ce).

In the Wolfcamp B (Fig. 3.3), all three carbonate indicators of Ca, Sr, and Mg were found to cluster loosely with one another. The strength of association between Mg and the other carbonate indicators of Ca and Sr depends on the dolomite presence in the interval.

The carbonates of the Wolfcamp A are dominantly composed of calcite. In contrast, the Wolfcamp B contains both calcite-dominated and dolomite-dominated lithofacies found within the interval. This likely produces a poorer cluster between the three carbonate elements. A similar observation is made for the terrigenous and paleoredox-sensitive elemental proxies. The close associations of terrigenous and redox-sensitive indicators seen in the Wolfcamp A are more loosely associated with one another in the Wolfcamp B. Clay mineral proxies, a subset of terrigenous elemental indicators, appear to have close associations with one another in the Wolfcamp B. These elements include Al, K, Zr, and Ti. Another group with Si, Cr, and Zn can be seen. Si is a fundamental element for silicate minerals. Cr is a redox-sensitive element associated with suboxic environments and broadly associated with organic matter. Zn is an element associated with anoxic conditions. A fourth group, Fe, Mo, U, and Th, is another loose cluster comprised of paleoredox-sensitive and terrestrial indicators. Rare-earth elements of Nd, Pr, La, and Ce also show a clear, yet looser relationship. The wider clusters found in the Wolfcamp B are likely attributed to more types of lithofacies observed in the Wolfcamp B compared to the Wolfcamp A, producing more complex elemental relationships.

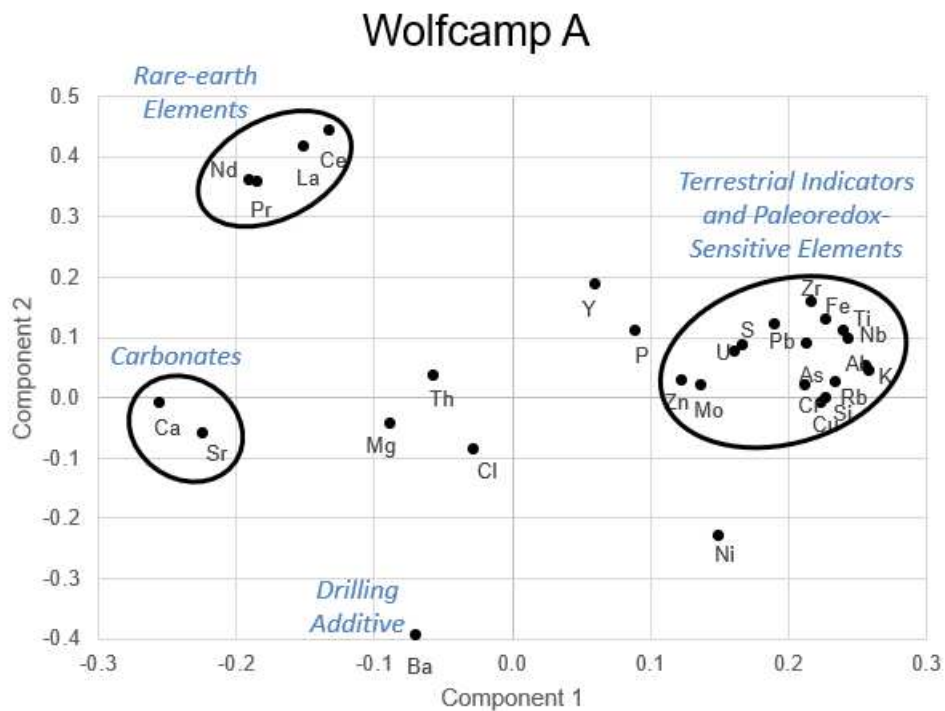


Figure 3.2—Principal component analysis (PCA) for the Wolfcamp A elemental dataset from XRF showing interpreted clusters of elements in circles.

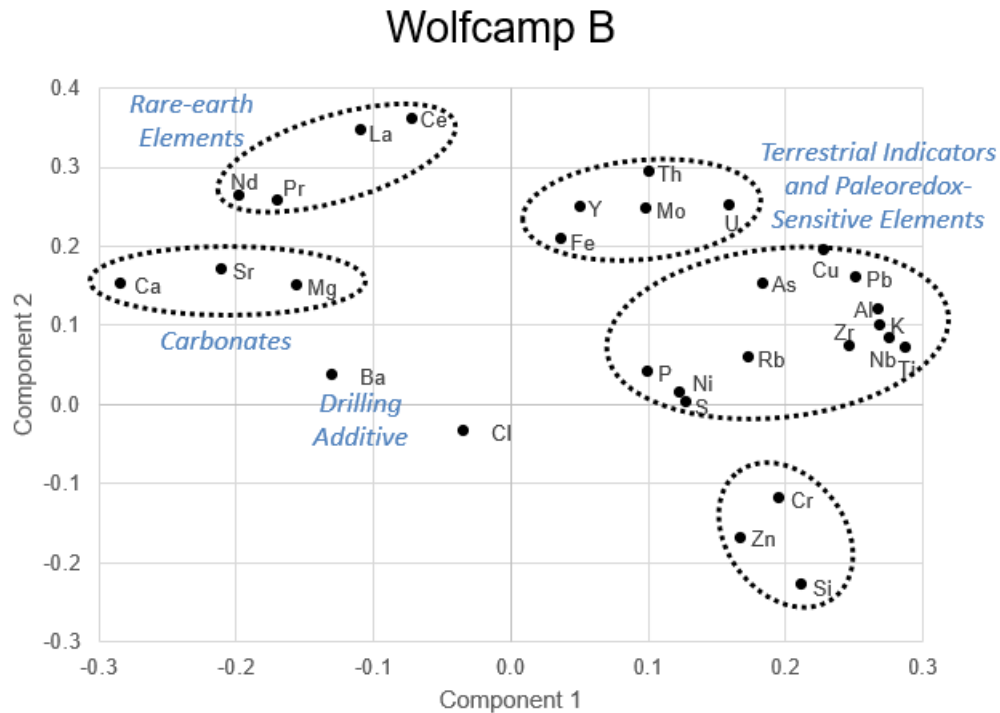


Figure 3.3—Principal component analysis (PCA) for the Wolfcamp B elemental dataset from XRF showing interpreted clusters of elements in circles.

3.3 Chemofacies

In addition to PCA, K-means clustering analysis was applied to the XRF dataset to define chemofacies. Chemofacies are rocks with similar geochemical or elemental signatures that are distinct from other strata. K-means clustering is another statistical method in which the “k” refers to the target number of clusters for the dataset. The term “means” refers to the averaging of data to identify the position of the centroid. The centroid represents the middle of the cluster. This method uses an iterative process to optimize the position of a centroid to keep the centroid a minimum size while assigning each sample point to a set number of clusters. K-means clustering was performed using Microsoft Excel. Cluster analysis was used to define four chemofacies and quantify the elemental signatures that make each of these chemofacies unique by taking into account the enrichment and depletion of each element analyzed. Bar graphs showing the elemental signatures in terms of enrichments and depletions can be seen in Figure 3.4. Enriched elements are shown in green, whereas depleted elements are in red.

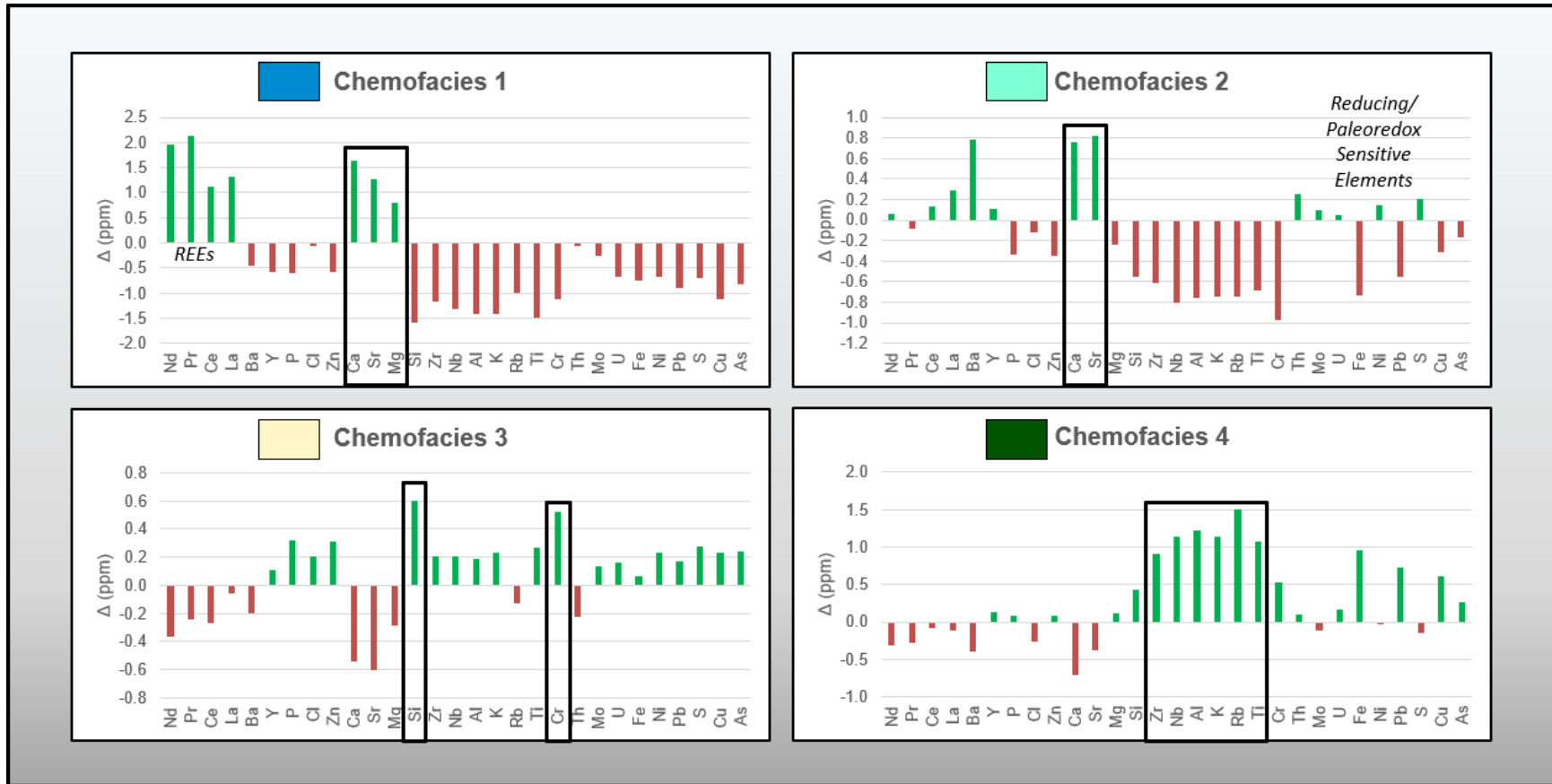


Figure 3.4—Bar graphs showing four chemofacies defined based on elemental signatures of enrichments and depletions. Elemental enrichments are shown in green and depletions in red.

Chemofacies 1 is enriched in the major elements Ca, Sr, and Mg, with depletions in terrestrial, clay, and paleoredox-sensitive elements. The elements Ca, Sr, and Mg are carbonate elemental indicators, suggesting that Chemofacies 1 is associated with carbonate-rich strata. Chemofacies 2 is enriched in Ca and Sr, slightly less than Chemofacies 1. Chemofacies 2 shows a depletion in Mg, which is enriched in Chemofacies 1. Other enrichments in Chemofacies 2 include several paleoredox-sensitive and reducing proxies, such as Mo, U, Ni, and S. The dominant enrichments in Ca and Sr suggest that Chemofacies 2 is also related to carbonate-dominated rocks. Slight enrichment in Th seen in Chemofacies 2 suggests potential terrigenous or clay influences. Both Chemofacies 1 and 2 show enrichments in carbonate elemental indicators as well as rare-earth elements (REEs). Conversely, REEs primarily show depletions in Chemofacies 3 and 4 that are also depleted in carbonate-related elements. A possible explanation is that REEs can be incorporated through microbial processes into marine carbonates. REE signatures from seawater or pore water are substituted for Ca in the crystal lattice. This occurs during precipitation or is post-depositional, during early diagenesis (Tobia and Aqrabi, 2016; Auer et al., 2017). Chemofacies 3 is most enriched in Si and Cr and depleted in carbonate elemental proxies. Si is a terrigenous indicator, while Cr is both a terrigenous and paleoredox-sensitive indicator for suboxic environments. Chemofacies 3 also shows some enrichments in elements associated with clay and other paleoredox-sensitive elements. Chemofacies 4 is the most enriched in terrestrial and clay indicators, including Al, K, Rb, Zr, and Ti. Paleoredox indicators of Nb, Cr, U, Fe, Pb, Cu, and As are also enriched along with slight enrichment in Mg.

3.4 Synthetic Gamma Ray

The elemental or synthetic gamma ray (GRsyn) is the total gamma ray calculated using elements of Th, U, and K from the XRF elemental data. The calculated synthetic gamma ray can be compared with the gamma ray from wireline logs to confirm the validity of the XRF dataset if similar curve signatures are achieved. The gamma ray log from wireline is a common tool used to identify lithologies and correlate wells. However, the standard gamma ray tool has a vertical resolution of 12-inches and a 24-inch depth of investigation (Bratton, 2014). The sampling resolution of the synthetic gamma ray, equivalent to the

XRF sampling resolution, is 6 inches or less, in this study. The gamma ray tool measures the total count of natural radiation emitted from the elements of Th, U, and K present in the formation. These three elements obtained from XRF measurements can be used to calculate the synthetic gamma ray based on the following equation (Rider and Kennedy, 2011):

$$GR_{syn} = (3.93 * Th_{ppm}) + (8.09 * U_{ppm}) + (16.32 * K_{wt.\%}) \quad (3.10)$$

The calculated GRsyn from core is compared to the wireline log suite of the Thunder C20-13 #2H in Figure 3.5. Both wireline total GR and GRsyn curves show similar log curve signatures indicating agreement between the two datasets. While wireline gamma ray can capture the overall lithology, GRsyn provides a more realistic gamma ray profile that aligns with the bed thicknesses and facies changes seen from core description. Wireline gamma ray tools are also prone to “shoulder effects,” in which the signal from a thin bed between thicker units is not fully observed (Masoudi et al., 2017). Shoulder effects are caused by the logging tool resolution and distort the petrophysical profile. Looking at Wolfcamp A, wireline total GR captures the overall characteristic of low gamma ray carbonate beds interbedded with high gamma ray strata that show abrupt contrasts. GRsyn from XRF can capture the individual bed profiles more precisely throughout the interval, showing a highly interbedded vertical section of low gamma ray beds that fines upwards into higher gamma ray beds. In Wolfcamp B, the vertical section shows high gamma rays from both wireline and synthetic gamma ray. Synthetic gamma ray captures thin carbonate beds at the top of Wolfcamp B that were described in core as seen in the lithofacies column but not observed in wireline gamma ray.

An up-close example comparing an eight-foot section of the wireline gamma ray, synthetic gamma ray, and the associated core section can be seen in Figure 3.6. The wireline gamma ray captures the large carbonate bed and the overall fining upward change in lithology. For the thin carbonate bed, the wireline gamma ray detects the signal but the signal is not fully developed (indicated by the black arrow). When core is available, using XRF to calculate GRsyn is a good method to bridge core analysis to the corresponding log signatures and to visualize changes in gamma ray under log resolution.

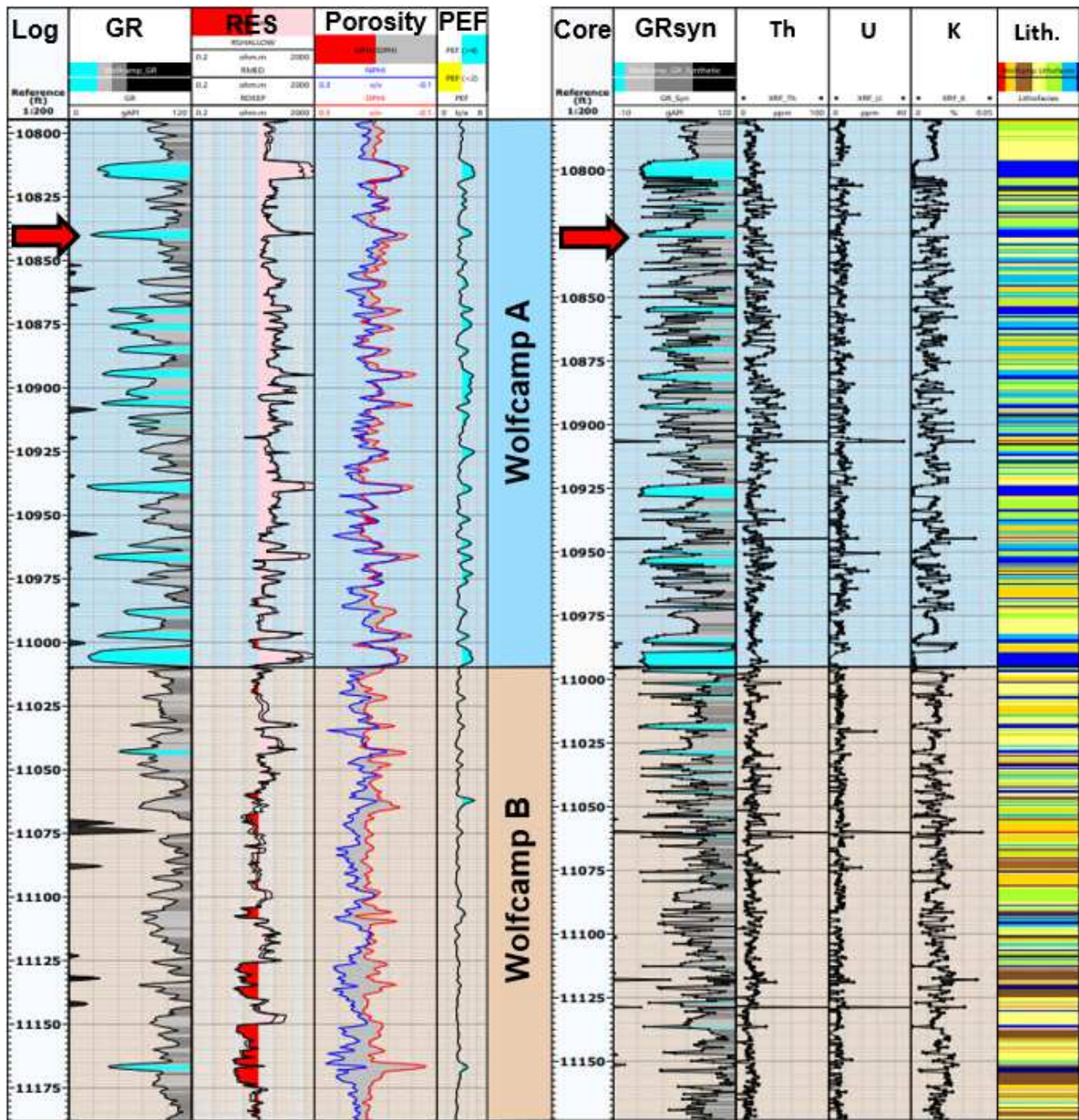


Figure 3.5—Comparison between wireline log gamma ray (GR) to core-derived synthetic gamma ray (GRsyn) calculated from XRF data. Wireline logs seen to the left show the following tracks (1) total GR, (2) resistivity curves, (3) porosity curves, and (4) photoelectric factor (PEF). Core-derived curves are seen to the right, showing the following tracks: (1) GRsyn, (2) XRF thorium concentration, (3) XRF uranium concentration, (4) XRF potassium concentration, and (5) lithofacies from core description. The red arrow indicates the location of the up-close example seen in Figure 3.6.

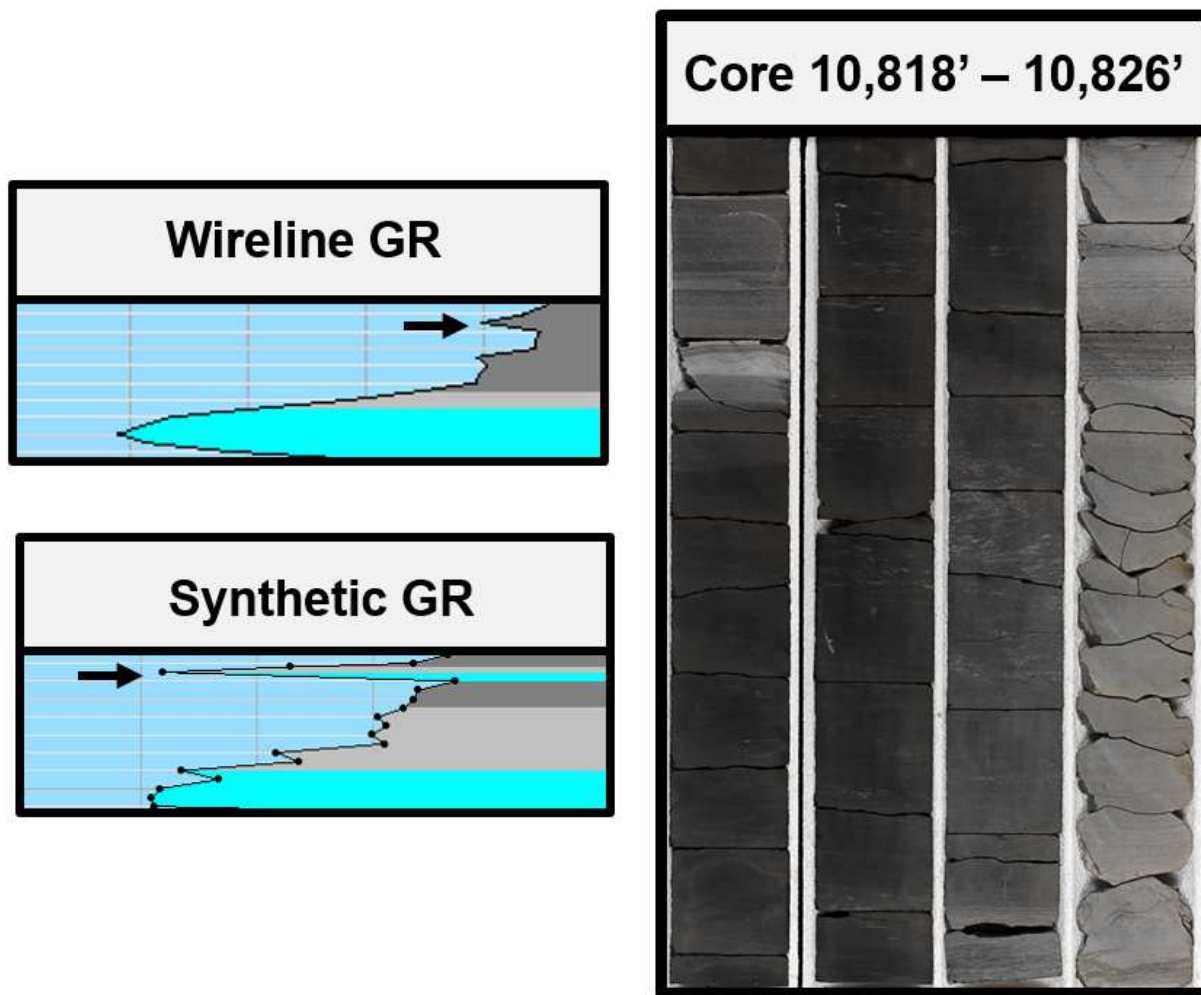


Figure 3.6—Comparison between wireline log gamma ray (GR) and core-derived synthetic GR (GRsyn) for an eight-foot section with the associated core interval. Wireline captures the overall change in lithology and thick beds. For thin carbonate beds (indicated by the black arrow), wireline captures the signal but the signal is not fully developed.

3.5 Terrestrial (Detrital) Indicators

Terrigenous influx proxies are used to provide insights into sediment provenance and indications of the amount of detrital material going into the basin (Driskill et al., 2018). Elemental components for terrestrial-driven influx are influenced by several factors, including the mineral composition of the source rock, weather regime, and diagenesis (Sageman and Lyons, 2009). Major elements associated with detrital flux are Si, Al, K, Ti, Rb, Cr, and Zr (Sageman and Lyons, 2009; Driskill et al., 2018). These elemental proxies are stable, land-derived elements that are less prone to the effects of diagenesis, dilution,

and grain size (Tribovillard et al., 2006). Crossplots against aluminum (Al) are commonly used to determine whether an element has a terrigenous source. Al is instrumental as a terrigenous indicator due to its association with clays and silicates and their diagenetic stability (Arthur and Dean, 1991). By crossplotting Al to other terrestrial indicators, a positive trend shows the correlation of the particular element to a detrital influence. A negative trend suggests that the element is associated with authigenic or biogenic origins (Tribovillard et al., 2006).

The elements potassium (K) and rubidium (Rb) are associated with clay minerals and weathering of potassium feldspar from felsic igneous rocks. Past studies, including Craigie (2018), have shown strong correlations between K and Rb to illite $[K_{0.8}Al_2[Al_{0.8}Si_{3.2}O_{10}](OH)_2]$. Rb ions can replace K in the illite structure. Figure 3.7.A shows a strong positive correlation between Al and K ($R^2=0.96$), suggesting that the elements are terrestrially sourced and appear associated with clay minerals. The crossplot of Al to Rb (Fig. 3.7.B) shows two strong, positive trends, with one trend that has an R^2 of 0.88 and a second trend with an R^2 of 0.90. However, there are two slopes that show slightly different ratios of Al and Rb. The differences in trendline can be caused by variations in mineralogy or mineralogical phase. Overall, the two positive trendlines still suggest that Rb entered the system as a terrestrial component.

Zirconium (Zr) is predominantly found in zircons ($ZrSiO_4$). Zircons are common accessory minerals in granite, syenite, granodiorite, pegmatites, and other igneous rocks (Nesse, 2014). Titanium (Ti) is a framework element in rutile (TiO_2), titanite or sphene ($CaTiOSiO_4$), and ilmenite ($FeTiO_3$). Rutile, titanite, and ilmenite are common accessory minerals in many igneous and metamorphic rocks (Sageman and Lyons, 2009). Ti and Zr are also useful detrital indicators due to their diagenetic stability. Positive trends observed between Al vs. Ti ($R^2=0.84$) and Al vs. Zr ($R^2=0.57$) suggest that these elements are terrestrial in origin. The element Cr is used as a paleoredox indicator but can have detrital fractions. Therefore, it is important to test the relationship of Cr with Al to determine the sediment origin. Figure 3.7.E shows a moderate, positive correlation between Cr vs. Al ($R^2=0.41$), suggesting that Cr is partially terrestrially derived and is less favorable as a paleoredox indicator.

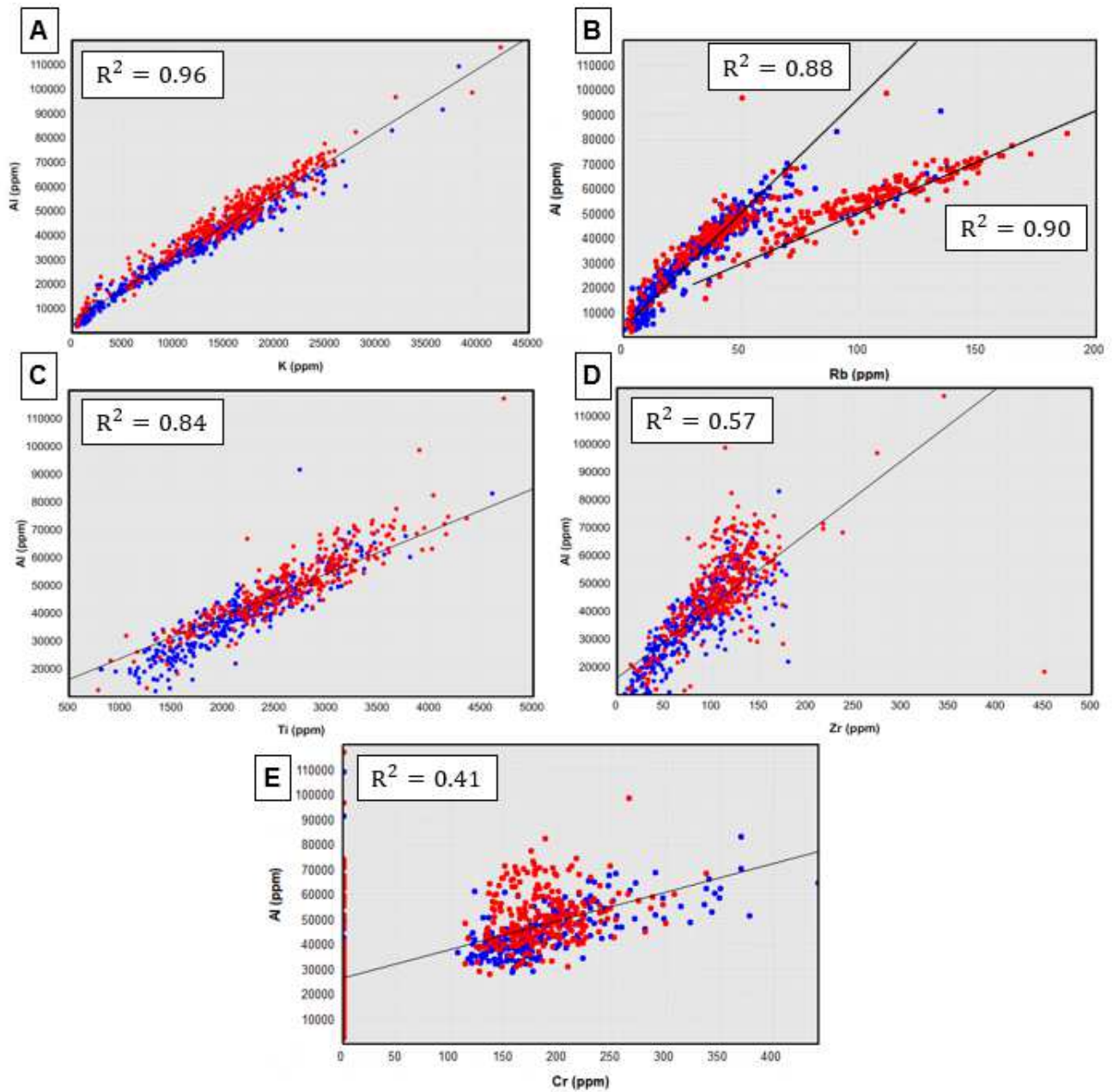


Figure 3.7—Crossplots of terrigenous influx proxies vs. aluminum (Al). Positive trends were observed in elements K, Rb, Ti, Zr, and Cr, suggesting that these elements are associated with terrestrial (detrital) input.

Silicon (Si) is a fundamental element for silicate detrital minerals, including quartz, feldspars, and clays. Si can be compared to Al in a crossplot to investigate the silica origin in the system. Compared to the other minerals observed, Si does not have as strong of a detrital trend because Si in the system can either be detrital, authigenic or biogenic. A strong positive correlation suggests that the silica is likely detrital in origin. A negative correlation between Al and Si suggests authigenic/biogenic sources. The negative correlation is explained as an excess of Si due to biogenic or authigenic influences (Sageman and Lyons, 2009). The elemental analysis for the Wolfcamp shows both a detrital and authigenic/biogenic trend (Fig. 3.8.A-D).

The Wolfcamp A, in blue, displays a distinct positive trend ($R^2=0.80$), suggesting a dominantly extrabasinal, detrital silica source (Fig. 3.8.A). However, samples with higher Si/Al abundances in the Wolfcamp A, show some biogenic and authigenic influences. In contrast, the Wolfcamp B has a weaker, positive trend ($R^2=0.31$) with more variance away from the detrital trend (Fig. 3.8.B). Instead, the Wolfcamp B shows stronger authigenic or biogenic influences. When they are plotted together (Fig. 3.8.C), samples that have a high Si/Al ratio in both the Wolfcamp A and B, show some deviation from the detrital trend. Looking at these data points by chemofacies (Fig. 3.8.D), the positive, detrital Si trend is made up of Chemofacies 1 and Chemofacies 2 from Wolfcamp A. Chemofacies 1 and 2 are enriched in carbonate elements such as Ca, Sr, and Mg. The silica source associated with more carbonate-rich strata in Wolfcamp A is dominantly detrital, with some authigenic/biogenic enrichment. Chemofacies 3 follows the positive detrital trend with authigenic/biogenic influences. Chemofacies 4 shows a negative trend, suggesting dominantly authigenic/biogenic sources of silica. The higher Al proportions observed in Chemofacies 4 corresponds to high clay strata. Chemofacies 3 differs in that it has higher enrichments in Si and lower enrichments in Al. Biogenic and authigenic sources of Si make up parts of the Si proportion in the Wolfcamp. A possible source of biogenic silica is from the dissolution of siliceous microfossils, such as radiolarian tests and sponge spicules. Both of these can be found in photomicrographs and thin sections from both the Wolfcamp A and B. Authigenic quartz in the form of intergranular, clay-sized microcrystalline quartz described in the literature are found within organic-rich shales in the Wolfcamp (Peng et al., 2019).

The elemental profiles for terrestrial indicators can be seen in Figure 3.9. Wolfcamp A and the top of the Wolfcamp B show lower concentrations of terrestrial indicators. Terrestrial influx increases to the middle and lower Wolfcamp B, particularly enriched in Al, K, and Rb. The increase in terrestrial elemental indicators corresponds to changes in lithofacies and chemofacies that have higher clay mineral and clay-associated elemental concentrations.

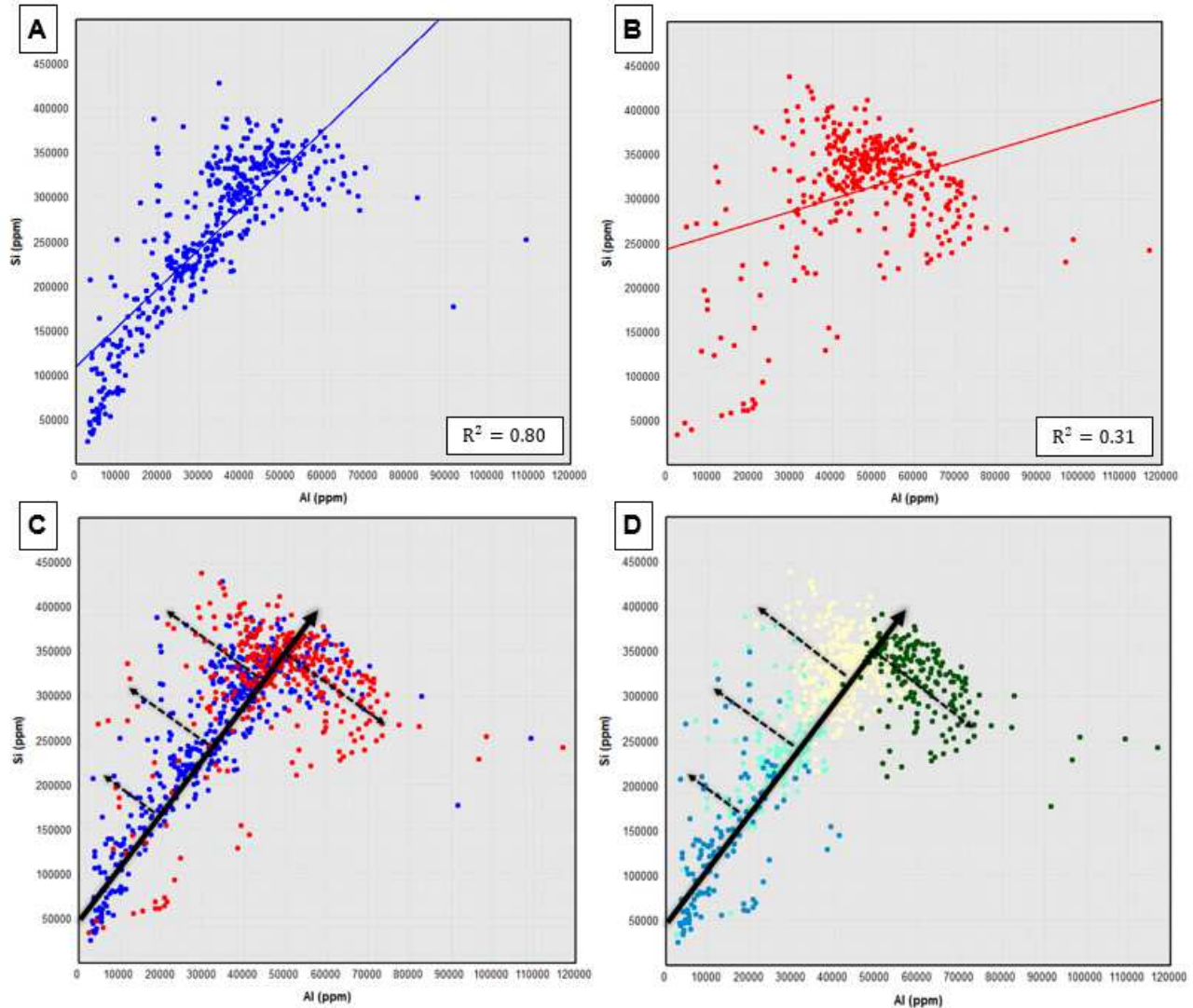


Figure 3.8—Crossplot of Al vs. Si to investigate the origin of silica in the Wolfcamp A and B. A positive trend indicates silica is detrital in origin. A negative trend, or deviation from the positive trend, suggests authigenic or biogenic influences. The crossplots include A) Si vs. Al for Wolfcamp A. B) Si vs. Al for Wolfcamp B. C) Si vs. Al for both Wolfcamp A (blue) and Wolfcamp B (red). D) Si vs. Al by chemofacies. Chemofacies 1 shown in blue ($R^2=0.31$, positive trend), Chemofacies 2 in light blue ($R^2=0.32$, positive trend), Chemofacies 3 in yellow ($R^2=0.01$, no trend), and Chemofacies 4 in green ($R^2=0.27$, negative trend).

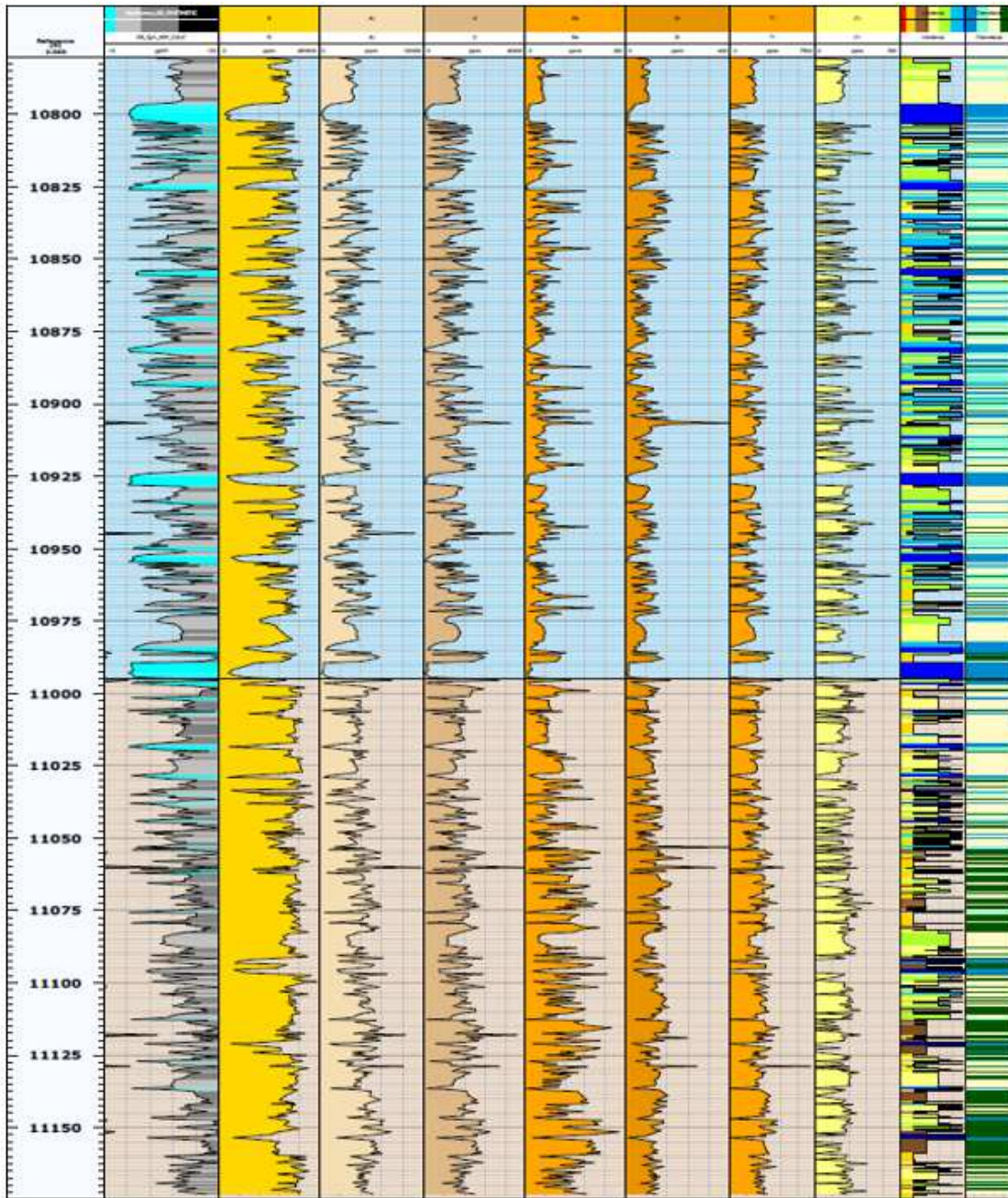


Figure 3.9—Elemental profiles for terrestrial indicators. Track 1: GRsyn. Track 2 through 8 show terrestrial indicators, from left to right, silicon (Si), aluminum (Al), potassium (K), rubidium (Rb), zirconium (Zr), titanium (Ti), and chromium (Cr). Track 9: lithofacies from core description. Track 10: chemofacies from cluster analysis.

3.6 Carbonate Indicators

Carbonate indicators are used to identify carbonate-rich intervals. Carbonate elemental indicators of Ca, Sr, and Mg are shown in elemental profiles in Figure 3.10. Calcium (Ca) is the primary cation of carbonate minerals, including calcite (CaCO_3) and dolomite [$\text{CaMg}(\text{CO}_3)_2$]. Strontium (Sr) is primarily found in aragonite and can substitute for Ca (Katz et al., 1972). From XRD analysis, calcite and dolomite are the dominant carbonate minerals found in the Wolfcamp. While manganese (Mn) is also a carbonate indicator, Mn values from XRF in this study often fell below the detection limit. Figure 3.10 shows that the highest carbonate flux is in the Wolfcamp A with enrichment particularly evident in Ca and Sr. The Wolfcamp B shows significantly lower concentrations in carbonate indicators. Thin beds showing enrichment in Ca and Sr can be seen at the top of the Wolfcamp B. Enrichments in Mg coinciding with low enrichments in Ca can be seen in known dolostone beds.

Ca is also a key element found in detrital anorthite ($\text{CaAl}_2\text{Si}_2\text{O}_8$), a plagioclase end member. Figures 3.11.A-B show crossplots of Ca vs. Al, displaying a negative trend ($R^2=0.70$). This indicates that Ca is not part of detrital anorthite. The negative trend is strongest in the Wolfcamp A (Fig. 3.11.A) as well as Chemofacies 1 and 2 (Fig. 3.11.B). Chemofacies 1 and 2 are enriched in carbonate elements corresponding to carbonate lithofacies. Chemofacies 3 and 4 that are depleted in carbonate elements (noncalcareous rocks) show a lack of trend. The overall negative trend confirms that Ca is not detrital and is authigenic or biogenic in origin.

Using PCA, carbonate indicators of Ca and Sr were both seen to be associated with one another in both the Wolfcamp A and B. A crossplot of Ca and Sr (Fig. 3.12) shows a high correlation between Ca and Sr ($R^2=0.84$). Ca and Sr are good proxies for calcite in both the Wolfcamp A and B. In contrast, from PCA analysis, the Wolfcamp A shows associations between the elements Ca and Sr, but not Mg. In the Wolfcamp B, Ca, Sr, and Mg are more loosely related to one another. This was also observed using crossplots of Ca vs. Mg (Fig. 3.13.A-B) that shows a clear positive trend only in the Wolfcamp B. No positive trend was seen in the Wolfcamp A. Mg is primarily found in association with dolomite. In the Wolfcamp B, where there are known dolostones from core analysis, high correlations

between Ca and Mg can be seen with an R^2 of 0.89. A positive trend can also be seen with Chemofacies 4, which is most abundant in the Wolfcamp B, associated with clay-rich strata.

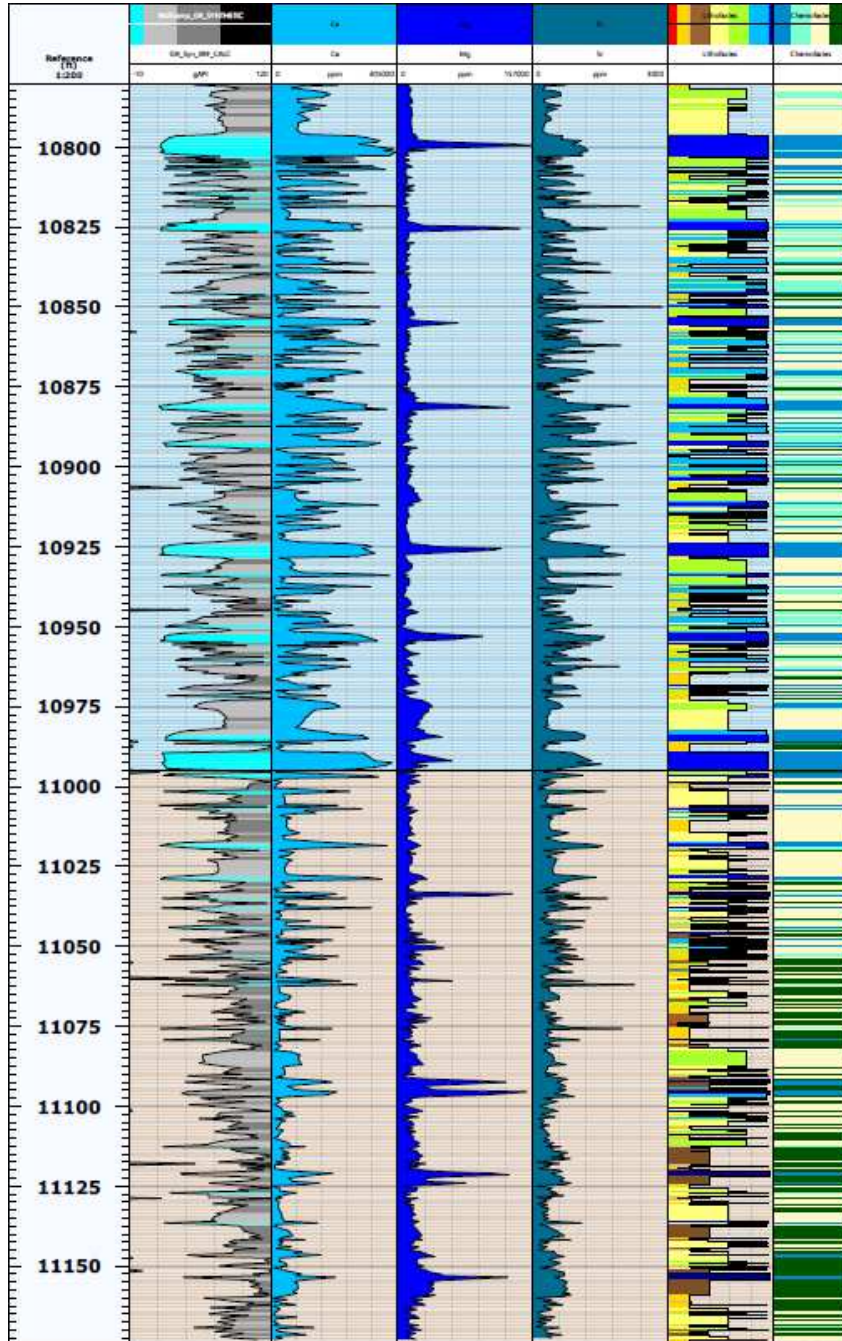


Figure 3.10—Elemental profiles for carbonate indicators. Track 1: GRsyn. Track 2 through 4 show carbonate indicators, from left to right, calcium (Ca), strontium (Sr), and magnesium (Mg). Track 5: lithofacies from core description. Track 6: chemofacies from cluster analysis.

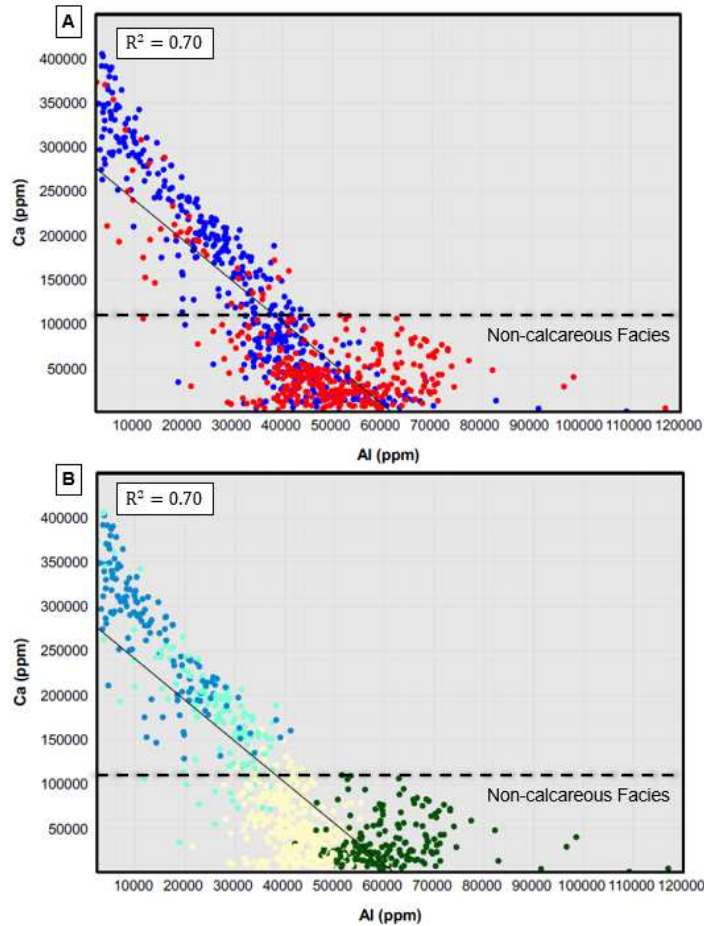


Figure 3.11—Crossplots of Ca vs. Al to determine the origin of Ca. A) Ca vs. Al for Wolfcamp A (blue) and Wolfcamp B (red). B) Ca vs. Al by chemofacies with Chemofacies 1 (blue), Chemofacies 2 (light blue), Chemofacies 3 (yellow), and Chemofacies 4 (green). The overall negative trend implies Ca does not have a detrital source and is either biogenic or authigenic in origin.

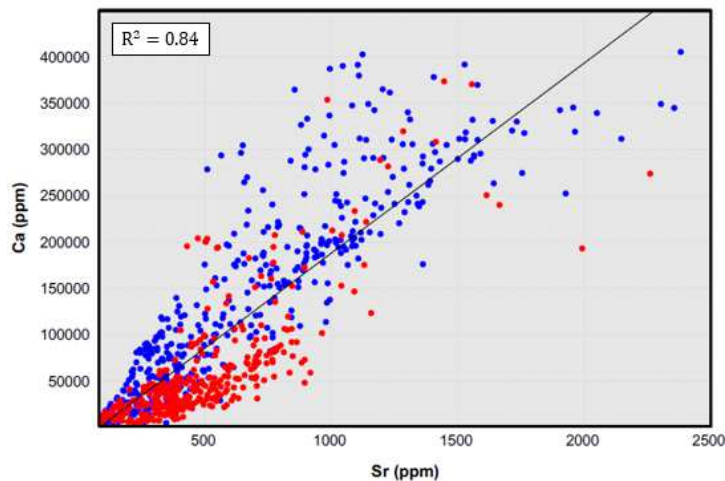


Figure 3.12—Crossplot of Ca vs. Sr for Wolfcamp A (blue) and Wolfcamp B (red). A strong positive correlation is seen in both Wolfcamp intervals.

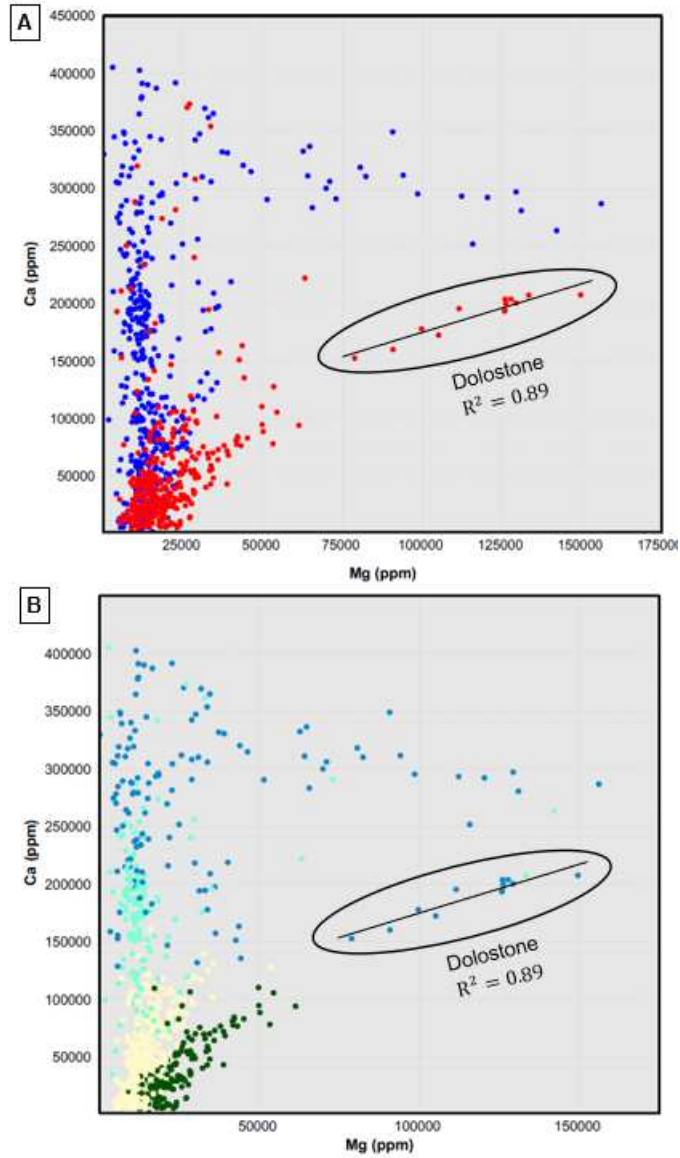


Figure 3.13—Crossplot of Ca vs. Mg showing A) Ca vs. Mg for Wolfcamp A (blue) and Wolfcamp B (red). B) Ca vs. Mg by chemofacies with Chemofacies 1 (blue), Chemofacies 2 (light blue), Chemofacies 3 (yellow), and Chemofacies 4 (green).

3.7 Redox-Sensitive Trace Elements

An important application of elemental analysis is to gain insights into paleoredox conditions and the level of dissolved oxygen present at the time of deposition. These often include tracking relative distributions of oxidizing agents to determine the paleoredox condition (Tribovillard et al., 2006). Redox conditions can be classified into a spectrum of five conditions, which range from oxic, dysoxic, suboxic, anoxic, and euxinic (Wignall et al., 2010). In oxic conditions, oxygen is readily available in the water column and interstitial waters, allowing it to be used by aerobic organisms. Oxic conditions are prone to the degradation of organic matter. In contrast, in anoxic and euxinic regimes, where dissolved oxygen levels are low to nonexistent, organic matter preservation is more favorable due to the reducing conditions that limit biological activity. Paleoredox-sensitive elements include Mo, U, V, Cr, Co, Zn, Ni, Cu, Zr, S, Se, Fe, and Nb (Tribovillard et al., 2006; Driskill et al., 2018). Redox-sensitive elements that indicate anoxic and euxinic conditions are often examined with TOC (Driskill et al., 2018). Elements including V, Co, and Se are paleoredox-sensitive elements that were often below the detection limit from XRF and could not be analyzed in this study.

The analysis of eight paleoredox-sensitive elements to the relationship of core LECO TOC can be found in Figure 3.14. A strong positive correlation ($R^2 \geq 0.5$) was established between Ni and TOC ($R^2=0.79$). Moderate correlations ($0.2 \leq R^2 < 0.5$) to TOC were observed in U ($R^2=0.40$), Cu ($R^2=0.35$), and Mo ($R^2=0.28$). Low correlations ($R^2 < 0.2$) to TOC were found in elements S ($R^2=0.18$), As ($R^2=0.16$), Fe ($R^2=0.10$), and Zn ($R^2=0.01$). Ni and Cu are organophilic trace elements that are preferentially enriched within organic molecules or micronutrients. Organophilic trace elements are also paleoproductivity indicators. Ni and Cu both occur in the water column as organometallic ligands, which are important micronutrients for marine organisms. These elements are transported into the sediment through the settling of organic materials. As they begin to decay, oxygen is removed to free the element and allows it to bind to S. These form NiS and Cu₂S compounds (Tribovillard et al., 2006). U in oxygen-rich waters is a soluble cation with an oxidation state of six that bonds with carbonate anions and diffuses at the sediment-water interface.

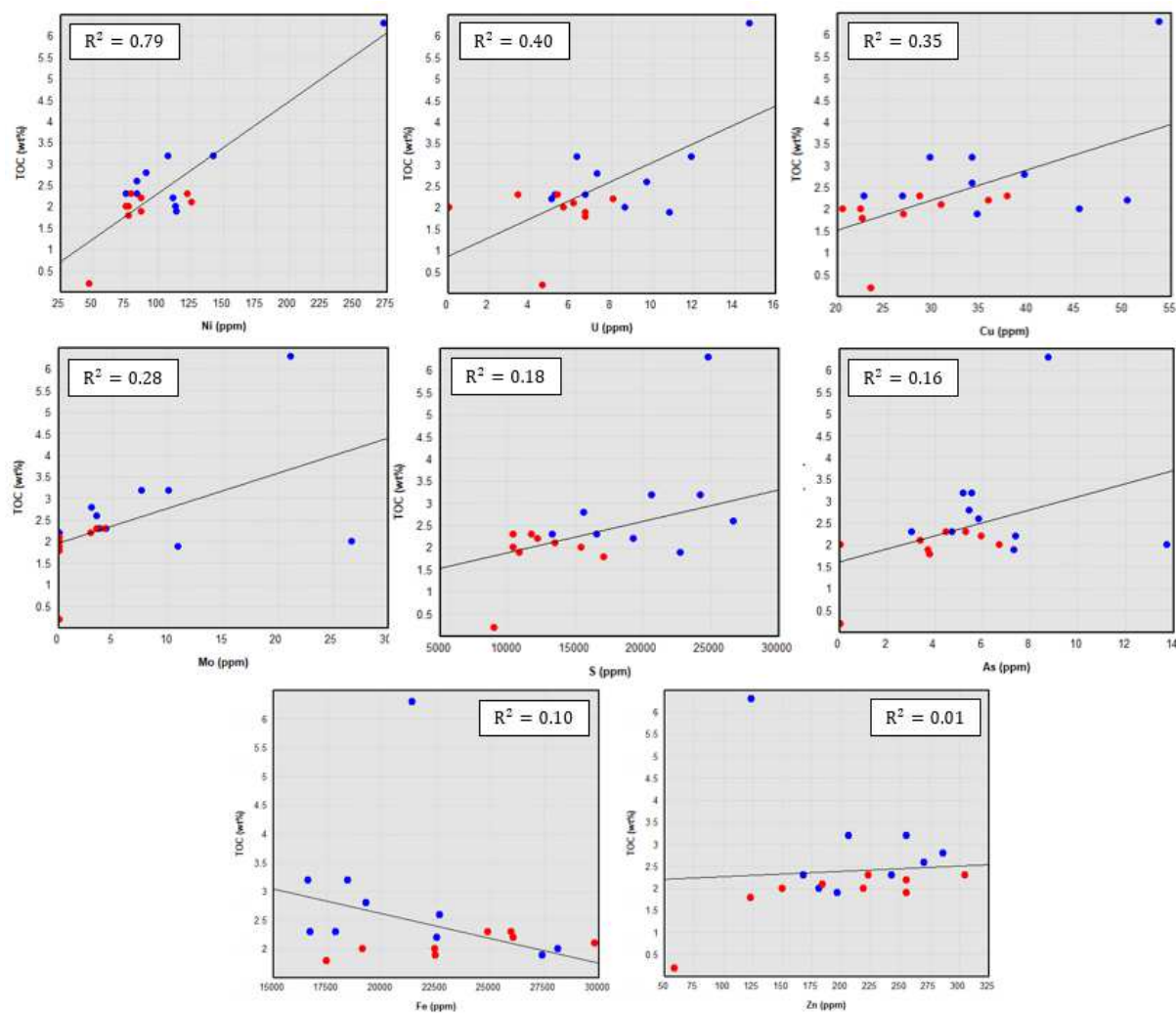


Figure 3.14—Crossplots of redox-sensitive trace elements vs. core TOC. The strongest relationship to TOC was seen for the element Ni ($R^2=0.79$). Moderate correlations were observed for U ($R^2=0.40$), Cu ($R^2=0.35$), and Mo ($R^2=0.28$). Low correlations were established for S ($R^2=0.18$), As ($R^2=0.16$), Fe ($R^2=0.10$), and Zn ($R^2=0.01$).

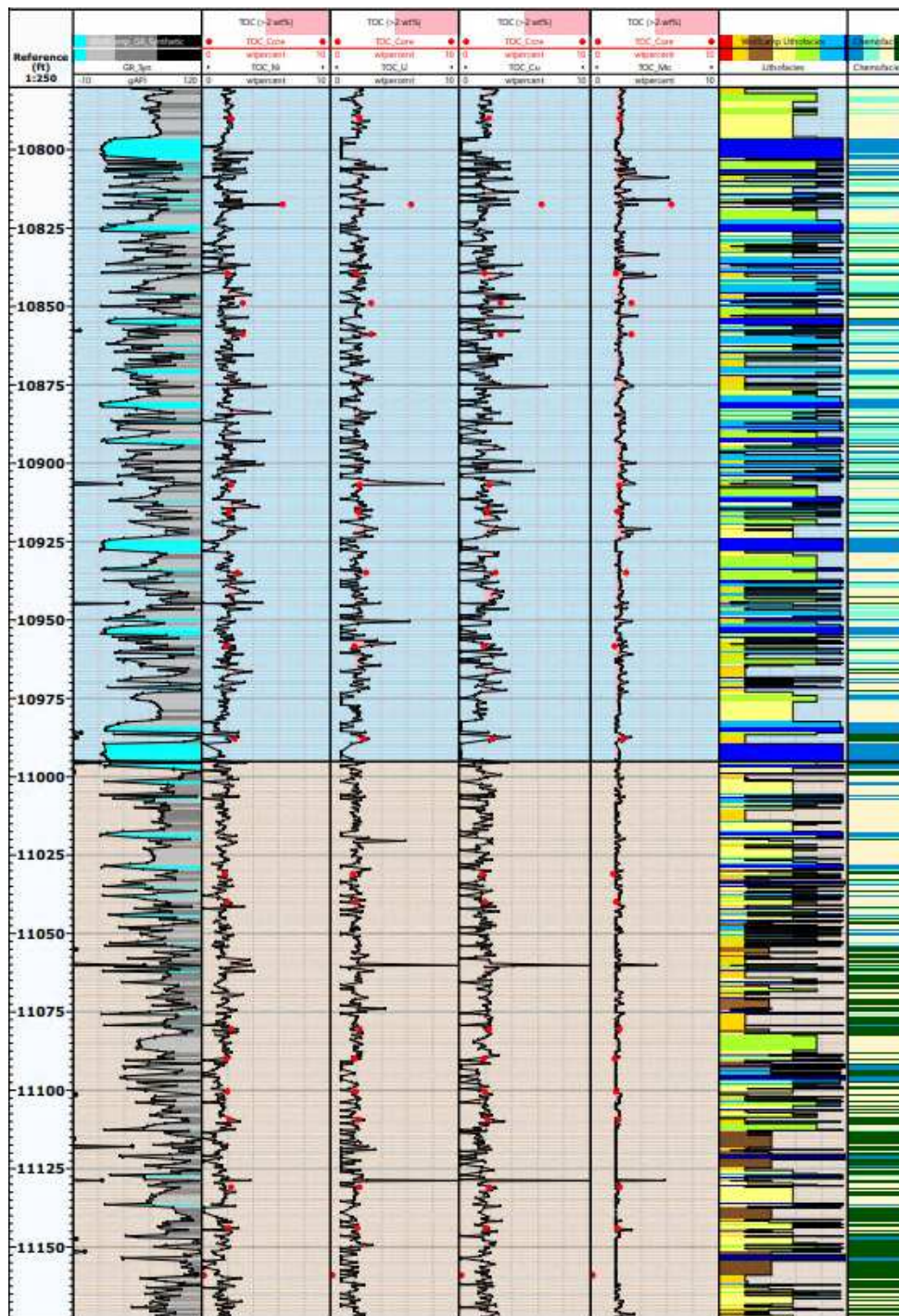


Figure 3.15—Calculated TOC from redox-sensitive elements that have strong to moderate correlations to core-measured TOC. Track 1: GRSyn. Track 2 through 5 show calculated TOC curves, from left to right, TOC_{Ni}, TOC_U, TOC_{Cu}, and TOC_{Mo}. Red dots indicate LECO TOC from core analysis. Track 6: lithofacies from core description. Track 7: chemofacies from cluster analysis.

However, when the sediment is in reducing conditions, U becomes stable in an oxidation state of four and precipitates into uraninite (UO_2). Studies of modern anoxic marine systems (Algeo and Lyons, 2006; Emerson and Huested, 1991) have shown that molybdenum (Mo) is a stable element that accumulates in sediments in anoxic or near-anoxic waters. In oxic waters, Mo has an oxidation state of six and is present in the form of a divalent molybdate anion (MoO_4^{2-}) with a neutral pH (Emerson and Huested, 1991). However, Mo can break away from its original structure as it approaches dysoxic, suboxic, and anoxic conditions. Mo can only be incorporated into the sediment in significantly prolonged, low oxygenated conditions or in high H_2S waters (Tribovillard et al., 2006).

Using crossplots of paleoredox-sensitive elements to TOC, the five elements, Ni, U, Cu, and Mo, were identified to have strong to moderate correlations to TOC. Using the equation established between these elements and core-derived TOC, TOC logs can be calculated as a function of depth as seen in Figure 3.15. For each element, the calculated TOC curve using paleoredox-elemental relationships was also compared to LECO TOC core data shown in red dots. Calculated log curves are shaded in for TOC greater than or equal to 2 wt.%, which is considered a good quality, unconventional reservoir rock (Diaz et al., 2013; Peters et al., 2016). From Figure 3.15, the element Ni shows the highest similarities between calculated TOC and core TOC. U and Cu show agreement between calculated and core TOC for moderate TOC values. However, very high and low TOC values analyzed from core did not match precisely to calculated values using U and Cu. TOC calculated from Mo shows to be the least precise compared to core TOC. Calculated TOC from Mo tends to overpredict TOC throughout the interval.

In Figure 3.16, paleoredox-sensitive elemental profiles show fluctuations in paleoredox-sensitive elemental concentrations throughout the Wolfcamp A and B. No significant thicknesses of high paleoredox-sensitive elements were observed in either Wolfcamp intervals, that would have shown prolonged periods of low dissolved oxygen conditions. Very high or low abundances in these elemental indicators are seen to be associated with individual beds. This is consistent with the arrangement of strata deposited primarily through sediment gravity flows from compositionally stratified beds. Paleoredox indicators combined with lithofacies can be used to interpret the redox conditions at the time of

deposition. Beds with the largest concentration of paleoredox indicator elements coincide with zones that have the highest gamma ray signatures. These beds are thin and found in both the Wolfcamp A and B. Spikes in the concentration of paleoredox indicators can be seen through multiple elements, including Mo, U, Zr, As, Nb, S, Fe, Ni, and Cu.

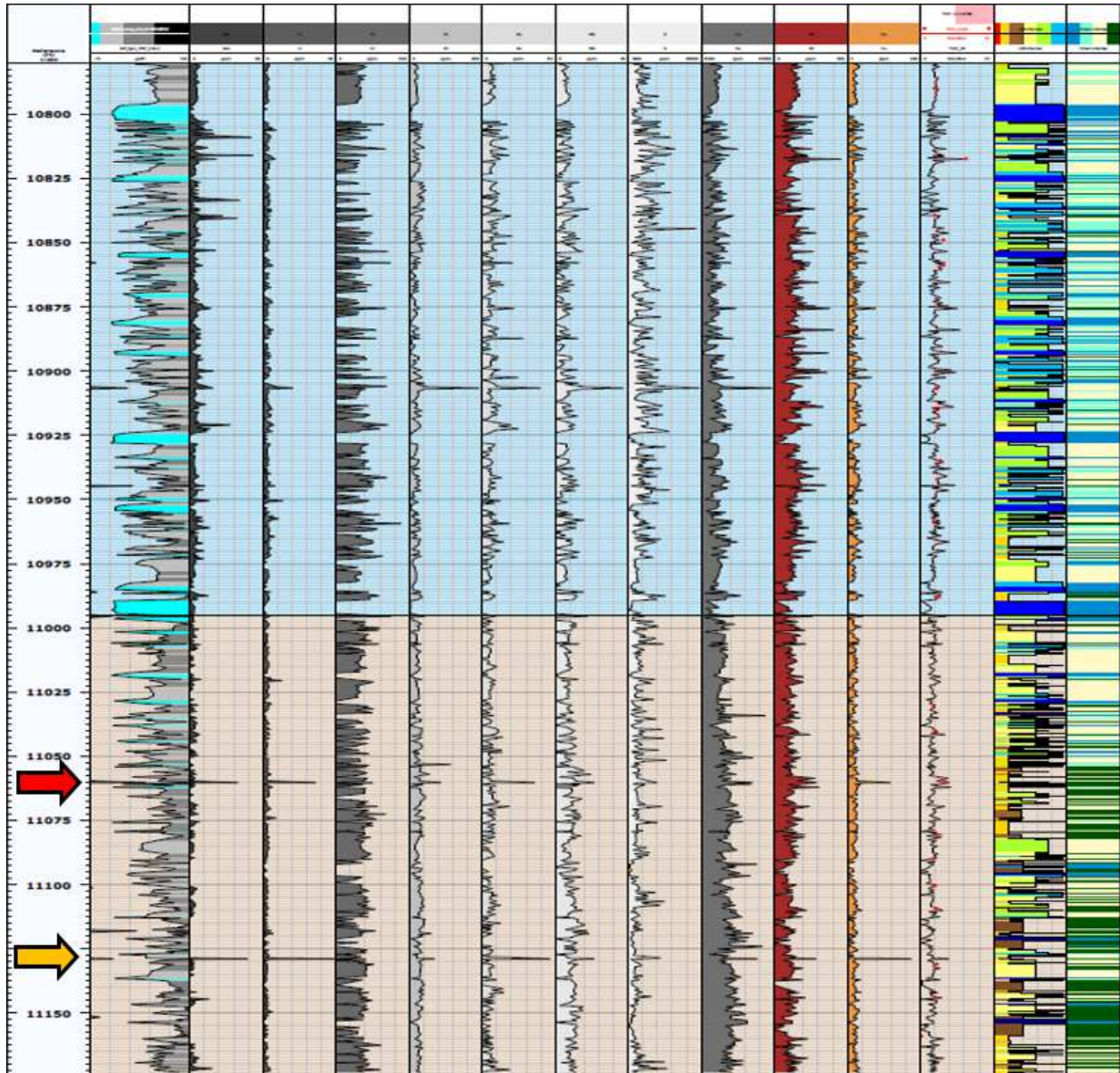


Figure 3.16—Elemental profiles of paleoredox-sensitive indicators. Track 1: GRsyn. Track 2 through 11 show paleoredox-sensitive indicators, from left to right, molybdenum (Mo), uranium (U), chromium (Cr), zirconium (Zr), arsenic (As), niobium (Nb), sulfur (S), iron (Fe), nickel (Ni), and copper (Cu). Track 12: TOC calculated from Ni ($R^2=0.79$). Red dots indicate LECO TOC from core analysis. Track 13: lithofacies from core description. Track 14: chemofacies from cluster analysis. The red and orange arrows show examples of core associated with elevated paleoredox-sensitive elements seen in Figure 3.17.

From Figure 3.16, depths with elevated concentrations of paleoredox indicators were examined in core. The highest increases are found associated with the siliceous mudstone lithofacies. Two examples of these core locations are shown in Figure 3.17 (core location indicated in Fig. 3.16 by arrows). The siliceous mudstone has several characteristics from core that support the interpretation of low oxygen conditions. Phosphatic nodules and beef fractures found in these cored locations are almost exclusively associated with the siliceous mudstone lithofacies. Studies examining Pennsylvanian authigenic phosphate nodules from the midcontinent have proposed that phosphate nodules develop below the sediment-water interface in suboxic to anoxic conditions (Kidder, 1985; Ece, 1990). The decomposition and dissolution of organic matter, promoted by anoxia, releases high phosphorus concentrations into the interstitial waters (Ece, 1990). As a result, phosphate nodules often occur in organic-rich black shales associated with high concentrations of TOC. Furthermore, the preservation of organic matter is more likely to occur in low oxygen, reducing conditions around the sediment-water interface. The siliceous mudstone has the highest average TOC of the lithofacies analyzed. The elevated concentration of paleoredox-indicators, presence of phosphatic nodules, and high TOC found in siliceous mudstones are independent factors that support that in these intervals, suboxic to anoxic conditions likely occurred at the time of deposition.

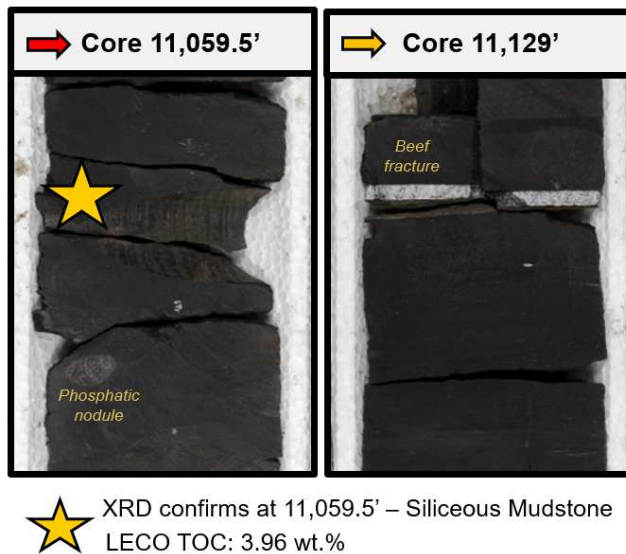


Figure 3.17—Core locations with high enrichments in paleoredox-sensitive elements found associated with the Siliceous Mudstone lithofacies. The core depths are indicated in arrows in Figure 3.16.

CHAPTER 4: RESERVOIR CHARACTERIZATION

The objective of reservoir characterization is to evaluate rock and fluid properties to understand their ability to store and produce hydrocarbons. Reservoir characterization includes a combination of technical skills from multidisciplinary groups, including geology, geophysics, petrophysics, petroleum engineering, geochemistry, geostatistics, and computer science (Slatt, 2006). For this study, a detailed geologic evaluation was conducted by integrating lithology (lithofacies and facies distribution), Source Rock Analysis (SRA), reservoir and fluid properties from Routine Core Analysis (RCA), and geomechanical data. The combination of these analyses is used to evaluate reservoir and nonreservoir prone rocks found in the Wolfcamp Formation. Core analyses are also compared to associated well logs to investigate the controls of rock and fluid properties on well log responses.

4.1 Source Rock Analysis

As an unconventional reservoir, the Wolfcamp Formation in the Permian Basin petroleum system is both a source and reservoir rock (Jarvie et al., 2017). Source Rock Analysis (SRA) data for 67 samples were prepared by GeoMark. Of these samples, 17 are from the Wolfcamp A, 16 from the Wolfcamp B, 30 from the Wolfcamp C, and 4 from the Wolfcamp D. An assessment of source rock analysis includes an investigation of the following: (1) the quantity of organic matter, (2) quality and type of organic matter, and (3) extent of thermal maturity.

The amount of organic matter is quantified through total organic carbon (TOC). TOC is the measure of organic matter enrichment in sediments, including both kerogen and bitumen. Kerogen is the fraction of organic matter that remains after pulverized rocks are extracted with organic solvents. Bitumen is the fraction of organic matter that is soluble in organic solvents. TOC is unitized in weight percent of organic carbon per weight of dry rock, or more simply as weight percent (wt.%). LECO TOC was performed on 67 samples. LECO refers to the method of estimating TOC using the instrument LECO carbon analyzer. Weighed samples are acidified, dried, and combusted to measure the amount of carbon dioxide produced. The released carbon dioxide is measured using an infrared detection cell

converted into TOC. TOC is indicative of the quantity of organic matter available for hydrocarbon formation and is an indirect indicator of hydrocarbon potential (Peter and Cassa, 1994).

The type of organic matter and the extent of thermal maturity can be determined through indices from programmed pyrolysis (Rock-Eval®). Pyrolysis is the thermal degradation of organic matter by heat within an inert atmosphere (Peters et al., 2002). The volume of hydrocarbons and carbon dioxide released from the sample is measured. The results for each sample can be seen in a pyrogram, which has three peaks referred to as S1, S2, and S3. As the sample of pulverized rock begins heating, the existing free organic compounds in the sample produce the S1 peak. The S1 (mgHC/g rock) peak represents the volume of free hydrocarbons present in the sample that is readily producible. As the sample is gradually heated, kerogen from within the sample is converted into hydrocarbon, producing the S2 peak. S2 (mgHC/g rock) is the volume of hydrocarbons formed with thermal alteration, which is an indicator of hydrocarbon potential. It is a term used to estimate the remaining hydrocarbon generative potential of a given sample. The temperature at which the S2 peak occurs is recorded as the term Tmax (°C), which is an important term used to interpret the extent of thermal maturity in a sample. The S3 (mg CO₂/g rock) peak represents the amount of CO₂ produced from kerogen during pyrolysis (Peter and Cassa, 1994). From the S1, S2, and S3 peaks produced, other important indices can be calculated, including HI, OI, and PI. The equations for the mentioned indices are as follows:

$$HI = \frac{100 \cdot S_2}{TOC} \quad (4.1)$$

$$OI = \frac{100 \cdot S_3}{TOC} \quad (4.2)$$

$$PI = \frac{S_1}{S_1 + S_2} \quad (4.3)$$

The hydrogen index (HI) represents the amount of hydrogen to organic carbon within a sample. The oxygen index (OI) represents the amount of oxygen relative to the amount of organic carbon in a sample. These two calculated indices from pyrolysis are used to determine the type of kerogen present in the rock using a modified van Krevlen diagram.

Modified van Krevlen diagrams can only determine kerogen type in rocks that are immature to early mature. As the source rock matures, the amount of hydrogen and oxygen to organic carbon decreases, causing the convergence of HI to OI points to plot towards the origin (0,0) on the modified van Krevlen diagram. Production index (PI) is another way to assess the maturity of a source sample by calculating relative proportions of S1 to S2. As a source rock matures, the S1 peak increases while the S2 peak decreases. As a result, higher maturity samples tend to have higher PI. Vitrinite reflectance (Ro or VRo) is a measure of maturity based on the percentage of incident light that is reflected from the surface of vitrinite particles in a sample (Peter and Cassa, 1994). Vitrinite reflectance is a visual determination and another key indicator for source rock maturity. SRA data for the studied Wolfcamp intervals plotted as a function of depth can be seen in Figure 4.1.

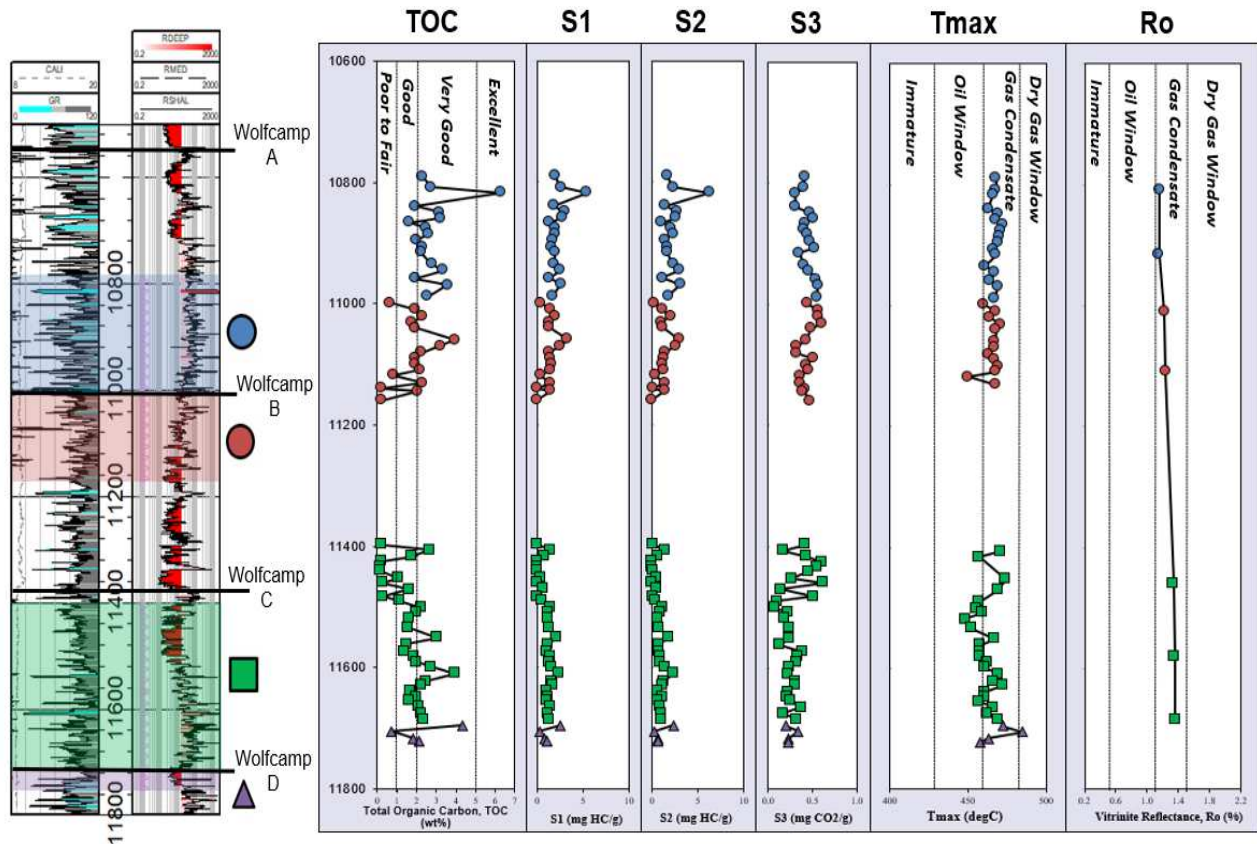


Figure 4.1—Source Rock Analysis (SRA) data for the Wolfcamp A, B, C, and D. TOC classification based on Law (1999) proposed for assessing source rock generative potential. Jarvie and others (2001) classification used for thermal maturity indicators Tmax and Ro.

4.1.1 Quantity of Organic Matter

LECO TOC for the Wolfcamp Formation in this study ranges from 0.15 to 6.30 wt.%. LECO TOC was measured at approximately 10 ft intervals throughout the Wolfcamp A, B, C, and D. From Figure 4.1, the Wolfcamp A has good to excellent TOC ranging from 1.64 to 6.30 wt.%. In the Wolfcamp B, over half the samples have TOC lower than 2 wt.%, reaching as low as 0.22 wt.% in organic-lean intervals. The Wolfcamp C shows samples with the lowest TOCs on the top one-third of the cored interval. In the lower two-thirds of Wolfcamp C, most TOC ranks as good to very good. The four samples from the Wolfcamp D were not enough to make a clear assessment. LECO TOC data provides an accurate, quantitative assessment of organic matter content in samples. However, they can be costly to perform and hence, can be undersampled. In heterogeneous strata such as the Wolfcamp, where facies change frequently, it is challenging to acquire measurements at a fine enough resolution to capture changes in TOC within an interval. Furthermore, measured TOC is limited to sampling from intervals with readily available cores.

Wireline logs can be used to approximate TOC continuously over depth for areas that lack core TOC measurements. The relationship between wireline total GR and spectral GR (U, K, and Th concentrations) was compared to core-derived TOC using crossplots in Figure 4.2.A-D. Comparing wireline GR to core TOC, total GR shows no relationship to TOC with R^2 of 0.02. Spectral GR concentrations for Th and K show negative relationships to TOC. Spectral GR concentration for U shows a positive relationship to core TOC ($R^2=0.40$) for the Wolfcamp Formation. U from spectral GR, or SGR_U , is often related to the amount of TOC in the formation (Peters et al., 2016).

Two methods were applied on a log scale to approximate changes in TOC throughout the Wolfcamp. First, TOC can be calculated from SGR_U using the equation from Figure 4.2.D. The calculated TOC curve from SGR_U is shown in Figure 4.3 (Track 5). Shaded in pink is TOC greater than 2 wt.%. Core TOC values are shown in the red dots. Since the uranium concentration has the strongest relationship to TOC, the concentration of uranium that makes up the total gamma ray curve can also be displayed directly on the gamma ray track (Track 1). Corrected gamma ray, CGR or GR_{TK} , is total gamma ray without uranium (with contributions from only thorium and potassium). By overlaying GR_{TK} together with

total gamma ray, the separation between the two curves is the concentration of uranium. The separation (uranium concentration) is highlighted in orange on Track 1 to approximate changes in organic matter content throughout the intervals. This method can quickly show intervals with high or low uranium concentrations as a proxy for TOC. Looking at Figure 4.3, uranium concentrations (in orange) appear to be the lowest from the Lower Wolfcamp B (not cored) and the Upper Wolfcamp C. The interval from the Lower Wolfcamp B to the Upper Wolfcamp C shows high total GR with little contribution from uranium, which suggests that these intervals are likely comprised of organic-lean clays. This observation was also seen in core measurements, where the lowest TOC values observed from core analyses were from portions of the Wolfcamp B and the Upper Wolfcamp C.

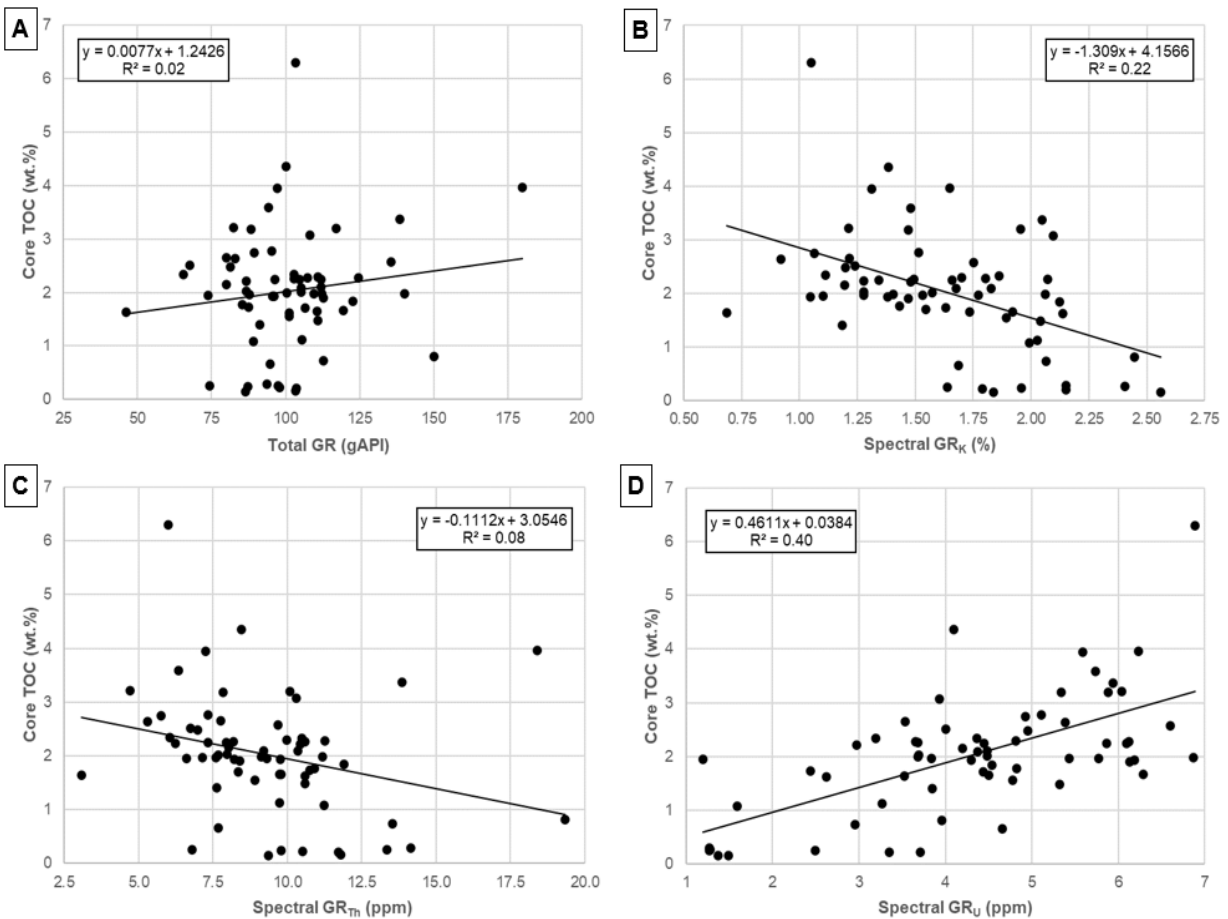


Figure 4.2—Crossplots investigating the relationship between LECO TOC from core vs. wireline GR. A) Total GR vs. TOC. B) Spectral GR from potassium (K) vs. TOC. C) Spectral GR from thorium (Th) vs. TOC. D) Spectral GR from uranium (U) vs. TOC.

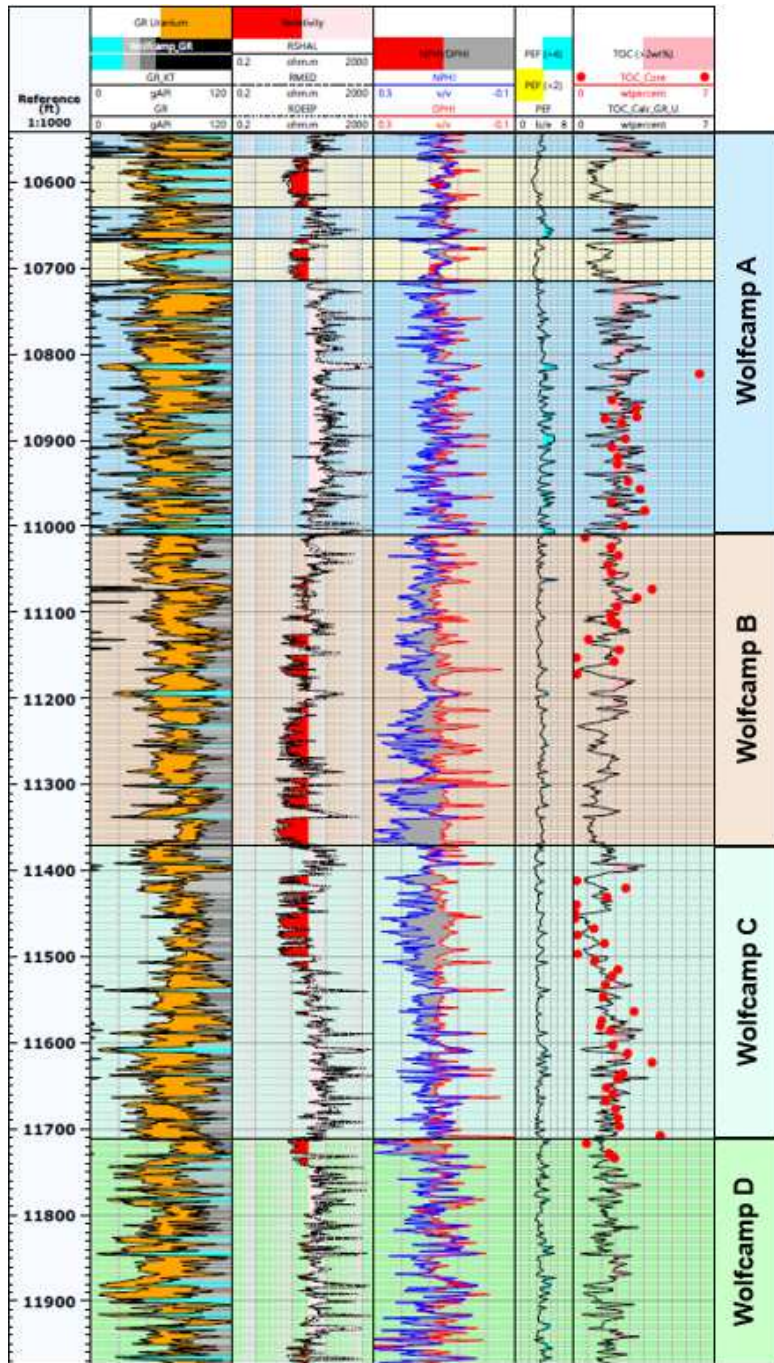


Figure 4.3—Indirect methods to approximate TOC on log-scale using spectral gamma ray from uranium (SGR_U). Track 1: GR_{KT} and GR, shaded in orange, is the contribution of uranium to total GR as a proxy for TOC. Track 2: resistivity curves. Track 3: porosity curves. Track 4: photoelectric factor (PEF). Track 5: TOC_{SGRU} calculated from the equation derived from SGR_U to core TOC (Fig. 4.2.D).

The quantity of TOC is an indicator of the total amount of organic matter in the sediment. However, TOC alone cannot be used as the only metric to evaluate good source rock potential. Organic matter requires hydrogen to be able to generate hydrocarbons. The hydrogen content can be estimated indirectly from the Rock-Eval S2 values. The S2 peak is an indicator of hydrocarbon potential, in which higher S2 values suggest greater hydrocarbon generating potential.

A crossplot of S2 vs. core TOC takes into account both hydrocarbon generating potential and TOC to evaluate source potential (Fig. 4.4). A classification from Dembicki (2009) was used for S2, which ranks generative potential from poor to excellent. This was paired with TOC guidelines from Law (1999) for assessing source rocks. Samples that are good quality source rocks, greater than 2 wt.%, are primarily found associated with the siliceous mudstone, carbonate-rich siliceous mudstone, and mixed calcareous silty mudstone. Lithofacies that predominantly rank poor to fair, or lower than 2 wt.%, are the calcareous siltstone, dolostone, bioturbated siliceous mudstone, and argillaceous mudstone. Looking at S2, almost all samples analyzed ranked poor to fair for hydrocarbon generative potential. Only one sample with the highest TOC showed good hydrocarbon generating potential from S2.

Low S2 values do not inherently show that the Wolfcamp is a poor source rock. Another critical evaluation to take into account for source rock analysis is the extent of thermal maturity. As a source rock matures, kerogen is consumed to generate and expel hydrocarbons. This will subsequently lower the amount of TOC in the sediment. As the source rock matures, the amount of hydrogen also decreases, producing a lower S2 peak in high maturity samples. Evaluating mature source rocks with present-day TOC and S2 values can make sediments look organic-lean, even for rich oil-prone source rocks. For mature source rocks, the original TOC in the sediment is higher than the present-day LECO TOC since the samples have already generated hydrocarbons (Dembicki, 2009).

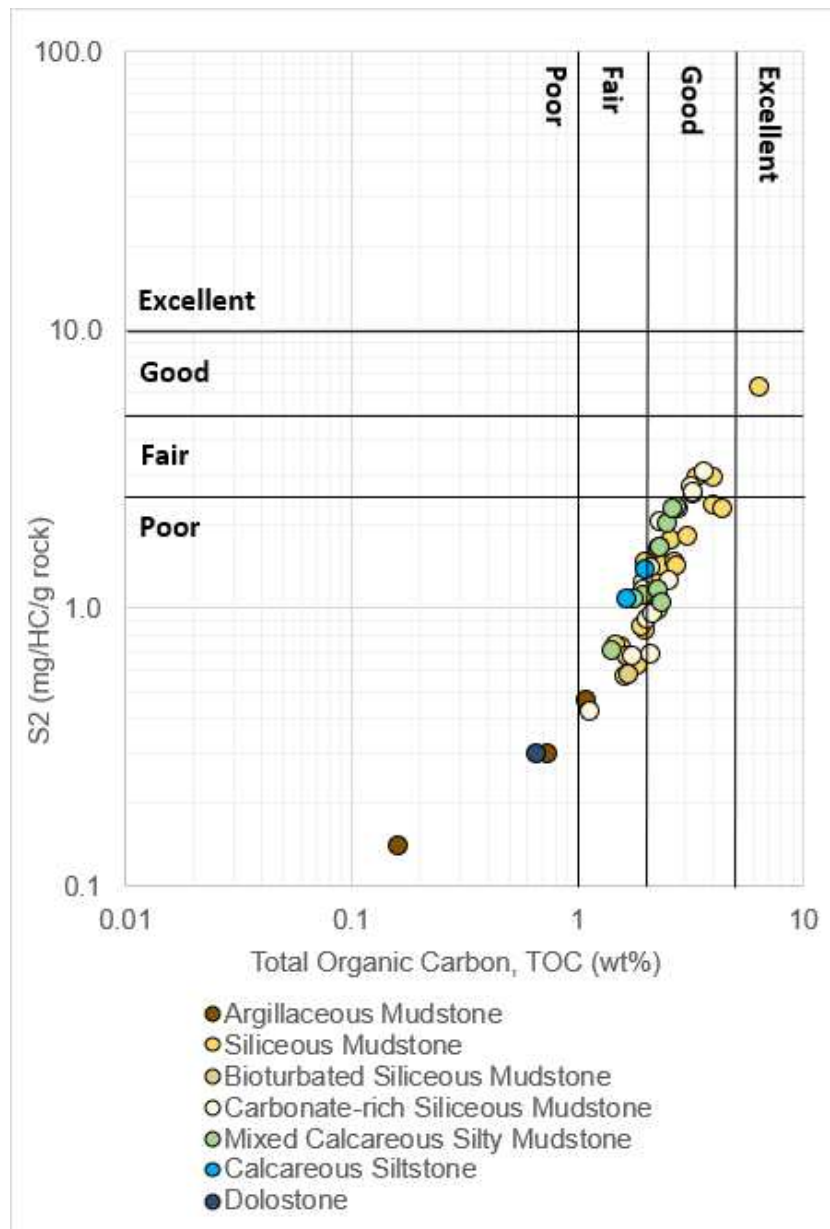


Figure 4.4—Crossplot of S2 vs. TOC showing that most siliceous mudstone, carbonate-rich siliceous mudstone, and mixed calcareous silty mudstone lithofacies have TOC values ranging from good to excellent. Calcareous siltstone, dolostone, bioturbated siliceous mudstone, and argillaceous mudstone are more organic-lean facies with TOC that ranked poor to fair. Most samples show poor hydrocarbon generating potential. Classification for TOC is based on Law (1999) proposed for assessing source rocks. Classification for hydrocarbon generating potential after Dembicki (2009).

4.1.2 Kerogen Type and Thermal Maturity

The type of kerogen and thermal maturity of a source rock determines the hydrocarbon product it can produce. Kerogen is defined as the portion of naturally occurring organic matter that is non-extractable or insoluble in normal petroleum solvents (Selley and Sonnenberg, 2015). Kerogen type can be determined by the atomic hydrogen to carbon (H/C) ratio and the atomic oxygen to carbon (O/C) ratio from elemental analysis in a van Krevelen diagram. A modified van Krevelen diagram uses hydrogen index (HI) and oxygen index (OI) from Rock-Eval pyrolysis to identify the type of kerogen and the maturation pathway of samples. Both methods generally yield similar results; however, pyrolysis is more inexpensive to perform and requires smaller samples for analysis (Peter and Cassa, 1994; Peters et al., 2016).

Rock-Eval pyrolysis HI and OI values for the Thunder C20-13 #2H well were plotted on a modified van Krevelen diagram to determine kerogen type and the extent of thermal maturity (Fig. 4.5). The lines on a modified van Krevelen diagram show the maturation pathways for each kerogen type as it matures. However, modified van Krevelen diagrams can only show valid kerogen type in immature to very early mature samples. HI and OI in samples from the Wolfcamp intervals in this study show high maturities. As source rocks mature and produce hydrocarbon products, kerogen becomes depleted in hydrogen. In later stages of maturity, during catagenesis and metagenesis, kerogen samples approach pure carbon (graphite) to the lower left side of the modified van Krevelen diagram, as seen with samples from the Thunder C20-13 #2H well. For most samples analyzed, maturity appears to increase with depth with the most mature samples from the Wolfcamp C and D.

The objective of thermal maturity assessments is to determine the type of product that will be generated. In unconventional reservoirs, thermal maturity and product type are directly related. A similar plot of HI vs. T_{max} shows that samples from this study plot primarily in the condensate wet gas window and late oil window (Fig. 4.6). T_{max} and R_o measurements, plotted as a function of depth, also show maturities dominantly in the condensate wet gas window (Fig. 4.1). T_{max} values from SRA range from 448 to 458 degrees. Seven samples of measured R_o , ranging from 1.16 to 1.36 % R_o , show maturities that all fall within the condensate wet gas window. Some T_{max} values fall below 453 deg

in the peak oil generation window as defined by Jarvie and others (2001). However, since T_{max} is dependent on the S2 peak from pyrolysis, samples with high maturities can have no peak or poorly resolved peaks. For high maturities, measured R_o is a more reliable indicator for thermal maturity. Measured R_o plots consistently in the condensate wet gas window. Looking at the overall gas-oil ratio (GOR) trend of the Delaware Basin, the location of the Thunder C20-13 #2H well is situated right in the middle of the condensate gas trend (Fig. 4.6). As an estimate, vitrinite reflectance data from the Permian Basin increases around 0.10 % R_o every 1,000 ft (Jarvie et al., 2017).

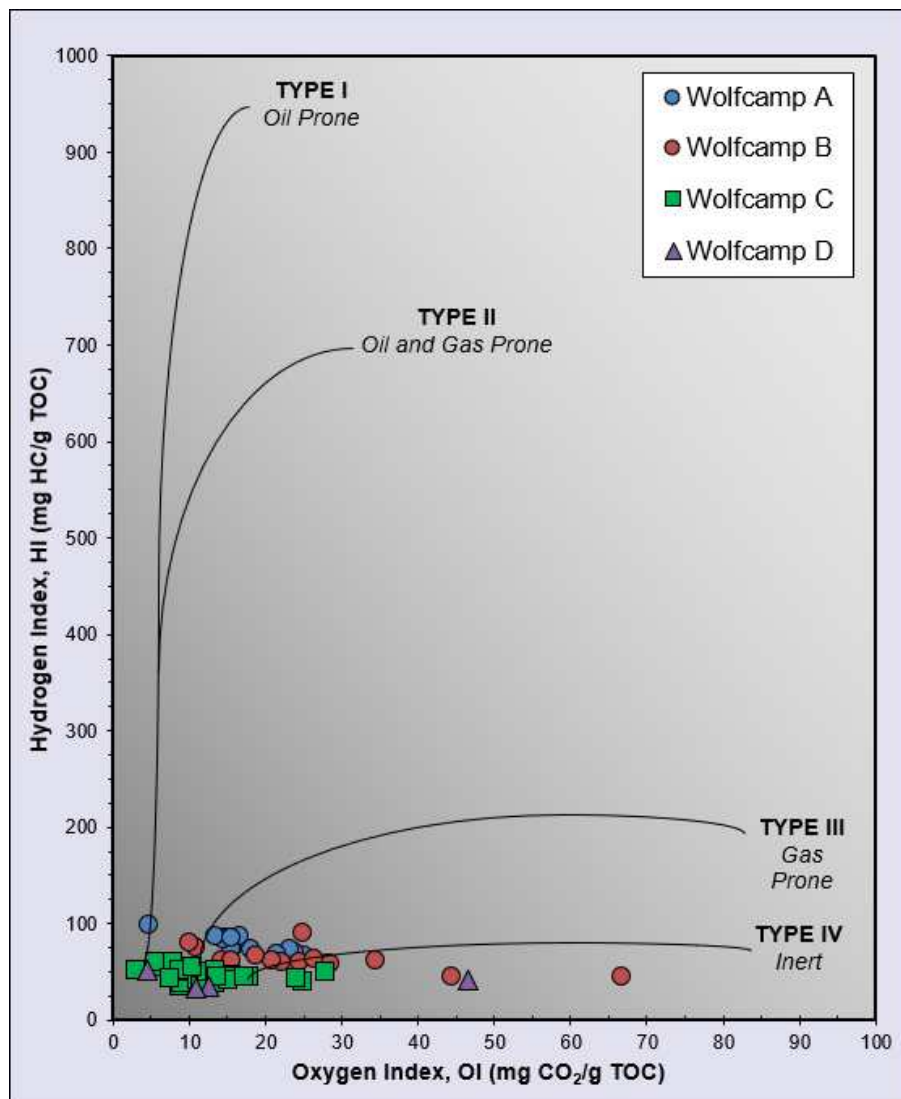


Figure 4.5—Modified van Krevelen diagram for hydrogen index (HI) vs. oxygen index (OI) showing the evolution pathways by kerogen type.

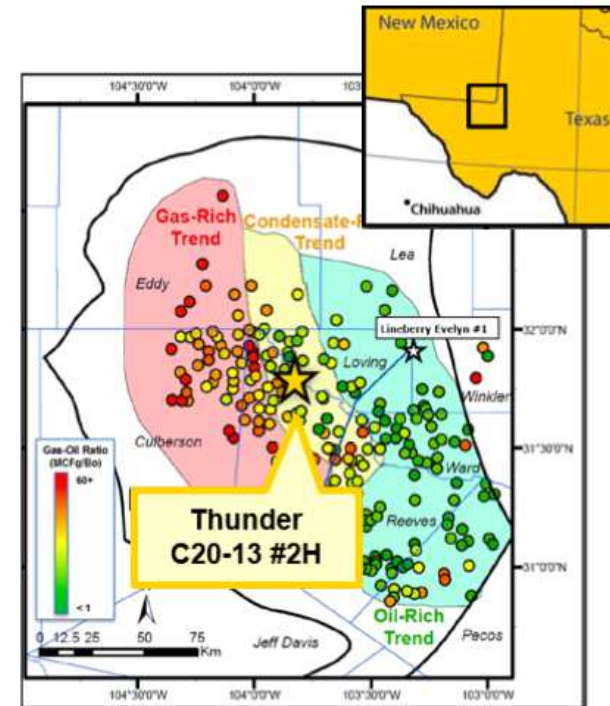
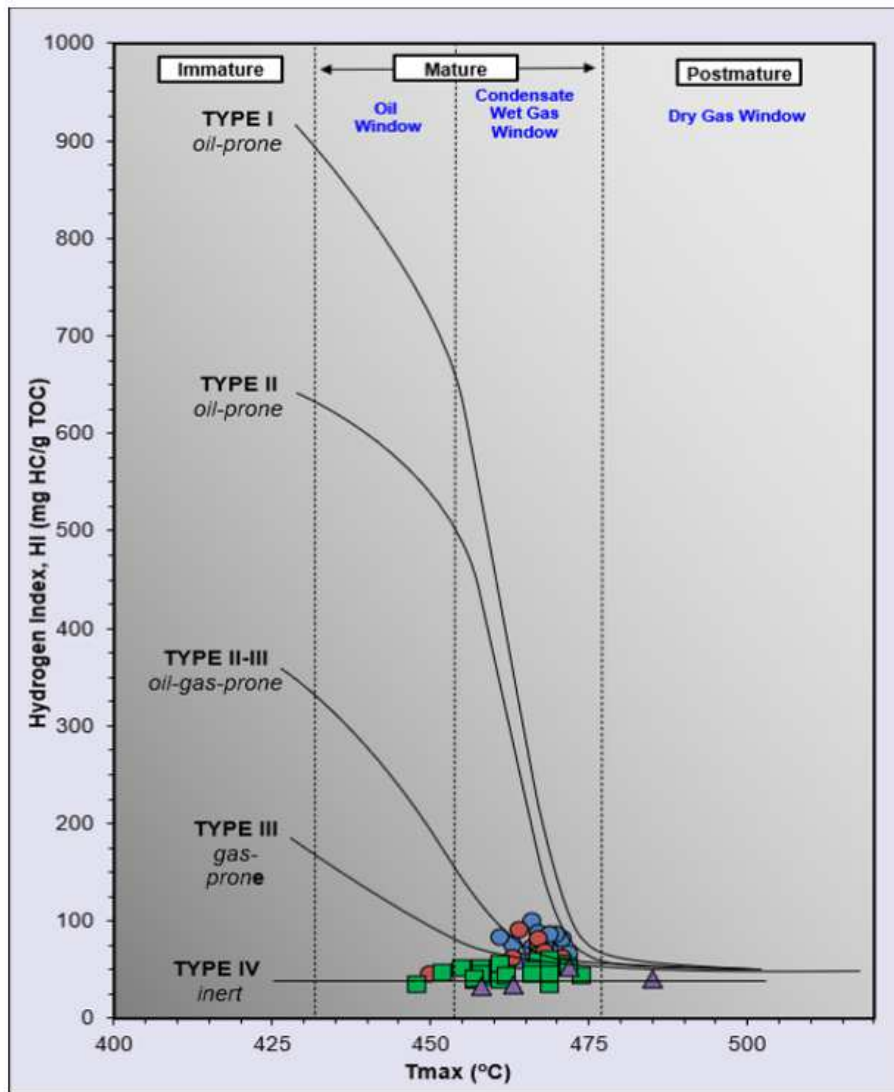


Figure 4.6—Crossplot of HI vs. Tmax showing that most SRA samples from the Thunder C20-13 #2H fall within the condensate wet gas window. Looking at the Delaware Basin gas-oil ratio (GOR) trend (modified from Mancos and Perez, 2018), the Thunder is situated in the middle of the condensate gas trend.

While pyrolysis data from SRA can determine that the thermal maturity for the Wolfcamp at this location is in the condensate gas window, it was too mature to identify kerogen type. Other studies have analyzed the kerogen type of the Wolfcamp from areas with lower maturities (Baumgardner et al., 2016; Kvale and Rahman, 2016; Gupta et al., 2017; Curtis and Zumberge, 2017; Kvale et al., 2020). These studies have shown that the oils generated from the Wolfcamp Formation are primarily attributed to Type II kerogen with contributions from Type III kerogen. Type II kerogen is derived mainly from marine phytoplankton cysts (acritarchs and dinoflagellates). Type II kerogen has moderately high amounts of hydrogen and can produce both oil and gas products. Type III kerogen is composed of vitrinite derived from woody components of plants on land (Jacobson, 1991). Kvale and others (2020) propose that sediment gravity flows are an essential transport mechanism for transporting detrital terrestrial organic matter into the deep basin.

4.2 Geomechanics

The assessment of geomechanical properties is important for unconventional reservoirs. Fracture stimulation, or hydraulic fracturing, is essential to produce economically from low permeability reservoirs, such as the Wolfcamp Formation. Geomechanical properties are used to inform frac models to understand fracture initiation, propagation, and geometry in the formation. Hydraulic fracturing models require a variety of inputs that can be subdivided into engineering parameters and geoscience parameters. Engineering parameters include stimulation designs and parent well analyses. Stimulation designs take into account the perforation design and pumping rate. Parent well analysis evaluates initial reservoir pressures, effective conductivity, and pump charts. Geoscience parameters include water saturation, porosity, permeability, geomechanical properties, and the thickness of units with similar attributes (Ramirez et al., 2012). These parameters are used to define the grid in a reservoir simulation model. These attributes are obtained either directly from core or indirectly from well logs (Murray, 2015). Rock properties such as water saturation, porosity, and permeability are discussed in the subsequent sections.

Geomechanical properties used to build geologic models are most often obtained from a sonic scanner, that for abundant, thin beds underestimates mechanical heterogeneity

(Sonnenfeld et al., 2015). A sonic scanner is a downhole logging tool that measures stress-dependent properties of the subsurface using acoustics from a series of transmitters and receivers. The tool provides quantitative rock mechanic properties such as Poisson's ratio (ν), Young's modulus (E), shear modulus (G), pore pressure gradient (P_{pore}), and unconfined compressive strength (UCS). Sonic log responses are used to calculate stress-dependent properties of the formation indirectly using empirical relationships (Bratton, 2014). These properties are essential for populating geologic and fracture stimulation models. The advantage of using a sonic scanner is that it provides continuous and rapid measurements of these properties downhole and is less expensive than procuring a core for direct measurements (Zahm and Enderlin, 2010). However, the vertical resolution of a sonic scanner is usually 2 to 5 ft. For beds under sub-log resolution, the signal will be observed but not fully developed (Glover, 2000). The thickness of Wolfcamp beds often falls below log resolution.

While the well log suite in this study did not include sonic scanner log data, it aims to provide measured geomechanical data from core, focusing on unconfined compressive stress and brittleness from the four Wolfcamp intervals. High-resolution measurements for unconfined compressive stress, taken every 2 to 6 inches, from the Wolfcamp core is used to (1) evaluate rock strength as a function of facies and (2) populate high-density rock strength data to understand the mechanical profile of the Wolfcamp that is below log resolution. Brittleness is calculated from XRD mineralogical data. Mineral-based brittleness is calculated from the ratio of minerals that are more brittle to the total minerals from the sample.

4.2.1 Unconfined Compressive Strength (UCS)

Rock strength is an important factor in fracture development for both natural and hydraulically induced fractures in the subsurface (Zahm and Enderlin, 2010). Unconfined compressive strength (UCS) is one of the most economical and practical ways of assessing rock strength in core (Zahm et al., 2014). UCS is the measure of material strength and is the maximum axial compressive strength determined at unconfined conditions, where confining stress is zero (Zoback, 2007). It is also referred to as uniaxial compressive strength because compressive strength is only applied along the longitudinal axis

(Schlumberger Glossary). UCS can be measured through mechanical stress tests performed in a laboratory using conventional core plugs (Zahm and Enderlin, 2010; Zahm et al., 2014). It can also be obtained indirectly through non-destructive techniques such as the use of a pointload penetrometer (Dimpler) or micro-rebound hammer. These hand-held tools are fast to obtain measurements, cheap to operate, repeatable, and non-destructive to the core. These tools provide reproducible and reliable results that are comparable to laboratory-based measurements of rock strength (Zahm and Enderlin, 2010).

An Equotip Bambino Piccolo 2 micro-rebound hammer was used to obtain UCS measurements from core throughout the Wolfcamp intervals. The hand-held device is easy to mobilize and quick to operate, allowing for high sampling resolutions from less than an inch or several feet, depending on the application. During data acquisition, the hammer is placed flat against the sample. The hammer is drawn back and released, which produces a striking impact through a spring and plunger within the device. The ratio between the rebound velocity (VREB) and impact velocity (VIMP) is calculated by the device and displayed on the screen. Harder rocks yield higher rebound velocities, resulting in higher magnitude readings. These rebound values, in units of Leeb Hardness (HLD), can be correlated to mechanical properties such as UCS.

To determine if an area of core is suitable for obtaining measurements, there are several criteria suggested by past studies to minimize sampling errors (Zahm and Enderlin, 2010; Murray, 2015; Zahm et al., 2014; Asiri, 2017). For example, measurements were taken avoiding fractures and partings that can lower HLD readings. Slabs of core that were thinner than 1.5 inches were also avoided. Measurements were obtained from the center of the core with greater thickness. Finally, samples must be stable when measurements are taken. A study by Asiri (2017) concluded through sampling 100 repeated measurements per sample of various lithologies that around 10 measurements per sample using an Equotip micro-rebound hammer is a good statistical representation of the true rock hardness.

For this study, at each sample depth, 10 measurements were obtained using the Equotip micro-rebound hammer. From these original 10 measurements, the minimum, maximum, average (mean), and standard deviation were determined. A trimmed mean is calculated by

taking the minimum and maximum values from the 10 individual readings out, producing a trimmed dataset. This practice is conducted to lower the standard deviation of the HLD readings. UCS is then calculated from the trimmed mean in HLD based on an empirical relationship developed by Zahm and Enderlin (2010). This empirical equation was produced from the analysis of HLD and UCS for lithologies of calcareous siliceous mudstones, lime grainstones, chalk, and other tight lime mudstone-wackestones detailed in the study. The equation for converting the trimmed mean HLD value to UCS is as follows:

$$UCS_{psi} = \frac{HLD-409}{0.0261} \quad (4.4)$$

$$UCS_{MPa} = USC_{psi} * \left(\frac{0.00689 MPa}{1 psi} \right) \quad (4.5)$$

A sample calculation for processing HLD readings to UCS can be seen in Table 4.1.

Table 4.1—Example calculation illustrating the workflow to calculate UCS. For each depth, 10 measurements taken with an Equotip Bambino micro-rebound hammer are recorded in Leeb Hardness (HLD). From the trimmed dataset (taking out the minimum and maximum values), the trimmed mean is used to calculate UCS (psi and MPa).

Unconfined Compressive Strength Sample Calculation										
Core Depth (ft)	Test Number	Leeb Hardness (HLD)	Minimum (HLD)	Maximum (HLD)	Standard Deviation	Trimmed Dataset	Trimmed Mean (HLD)	Trimmed STD	UCS (psi)	UCS (MPa)
10815	1	628	600	631	11.0	628	620.0	9.3	8084.3	56
10815	2	607				607				
10815	3	600				-				
10815	4	627				627				
10815	5	626				626				
10815	6	604				604				
10815	7	628				628				
10815	8	625				625				
10815	9	631				-				
10815	10	615				615				

This study measured and analyzed 1,277 sample depths for rock strength with the described methods. The two primary goals were to (1) evaluate changes in rock strength as a function of lithofacies, and (2) sample at sub-log resolution to obtain a high-resolution rock strength profile for the Wolfcamp intervals. An example of the sampling density and final calculated UCS results can be seen in an example of a core section in Figure 4.7.

Measurements were taken continuously at 2- to 6-inch increments to provide a high data density rock strength profile through the vertical section. Wolfcamp beds can range from a few inches or less to several feet in thickness. Core measurements aim to capture rock strength variations under the 2- to 5-foot vertical resolution of a sonic scanner logging tool. At each sampling location, the associated lithofacies defined from core description is noted. Looking at the variations in UCS (in MPa) in the cored section shown in Figure 4.7, higher rock strength is recorded in the lighter gray, carbonate-rich packstones and calcareous siltstones. Lower rock strength measurements are recorded with dark gray mudrocks. Changes in rock strength can be seen within short intervals as a function of facies.

Figure 4.7 also shows an example of the changes in rock strength within a sediment gravity flow deposit, indicated by the red arrow. The base of the hybrid event bed is composed of a packstone bed with rock strength of 67.4 MPa. Hybrid event bed deposits show stacking of fining upward beds that decrease in carbonate content and grain size as the flow wanes. The highest rock strength is observed to be at the base of the deposit. Even within the basal packstone lithofacies, rock strength decreases slightly towards the top of the packstone bed. As the beds fine upwards into a calcareous siltstone, followed by a mixed calcareous silty mudstone, carbonate-rich siliceous mudstone, and siliceous mudstone lithofacies, the UCS values decrease concurrently.

Analysis of rock strength by lithofacies, from the entire dataset, showed that the strongest rocks in the Wolfcamp are the skeletal packstone with an average UCS of 65.4 MPa (Table 4.2). Other carbonate-rich rocks, including the wackestone, dolostone, and calcareous siltstone, also exhibit high average rock strength ranging from 59.2 to 62.4 MPa. The mixed calcareous silty mudstones, carbonate-rich siliceous mudstones, and bioturbated mudstones show intermediate average rock strength from 50.9 to 56.5 MPa. The lowest rock strength was observed in the clay-rich facies, including the argillaceous mudstone and siliceous mudstone, with average UCS of 44.7 and 46.9 MPa, respectively. The box plot of UCS values for each facies is shown in Figure 4.8. The “x” is the average (mean) UCS value. The median is shown with the line in the box. UCS values that make up the lower quartile (Q_1) and upper quartile (Q_3) are shown as the box. The minimum and maximum values are shown by the whiskers.

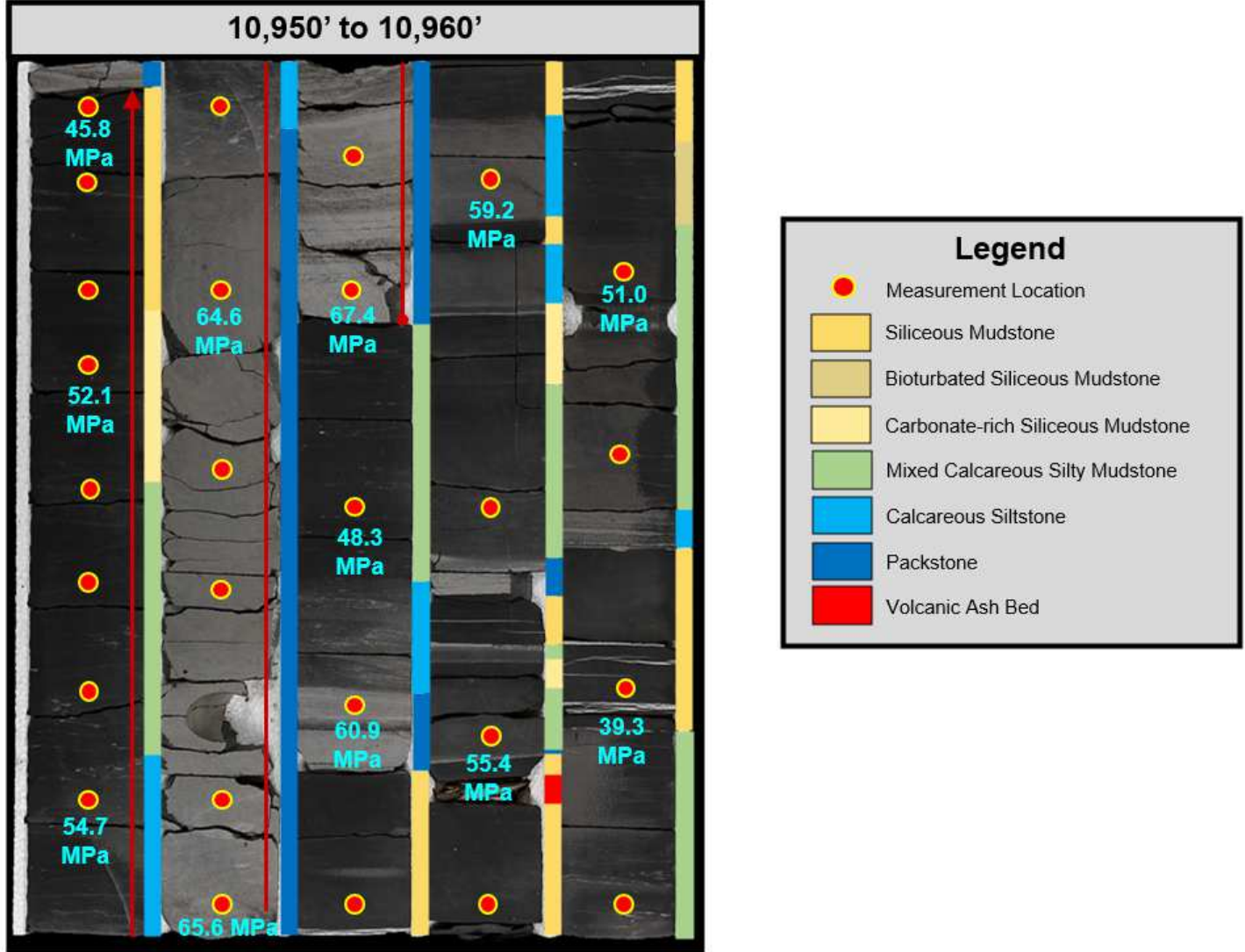


Figure 4.7—Calculated values for unconfined compressive strength (UCS in MPa) shown throughout a 10 ft core section with corresponding lithofacies. The red arrow indicates a single hybrid event bed (HEB) deposit showing decreasing rock strength as the HEB deposit fines upwards.

Table 4.2—Values for unconfined compressive strength (UCS) from core based on lithofacies.

Lithofacies	Unconfined Compressive Strength, UCS (Mpa)			Count, n (-)
	Minimum	Maximum	Average	
Argillaceous Mudstone	31.6	56.5	44.7	99
Siliceous Mudstone	27.1	59.9	46.9	197
Bioturbated Siliceous Mudstone	38.5	66.5	50.9	62
Carbonate-rich Siliceous Mudstone	33.1	69.3	53.0	327
Mixed Calcareous Silty Mudstone	39.8	70.6	56.5	228
Calcareous Siltstone	46.4	74.1	59.2	150
Dolostone	56.9	68.3	61.8	19
Wackestone	58.2	68.7	62.4	7
Packstone	51.5	79.9	65.4	188

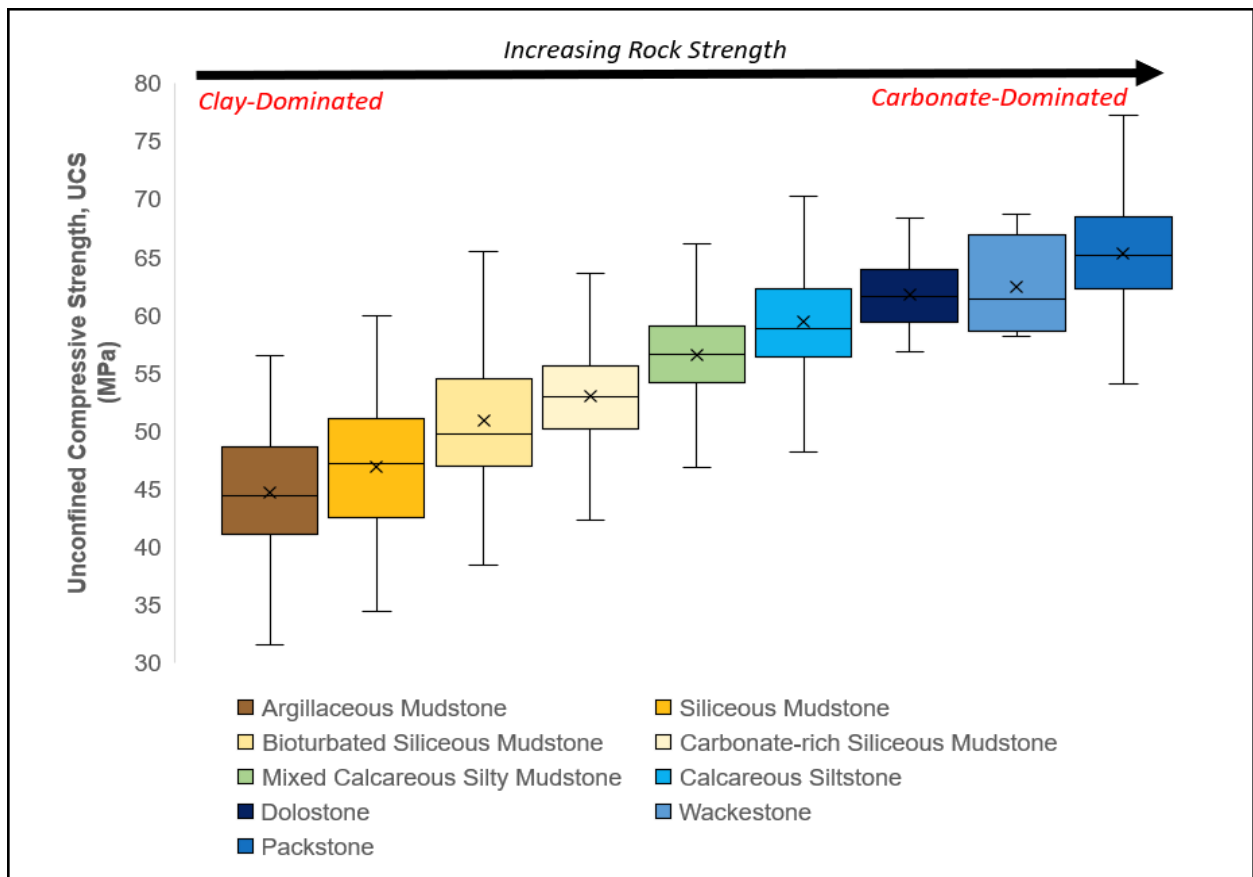


Figure 4.8—Box diagram of calculated unconfined compressive strength (UCS) based on lithofacies. Rock strength is highest in carbonate-dominated lithofacies and lowest in clay-dominated lithofacies.

Measurements of UCS in this study are comparable to those found in the Wolfcamp literature. An analysis of rock strength by Baumgardner and others (2016) showed that for the Wolfcamp Formation in the Midland Basin, the skeletal wackestone/packstone has an average UCS of 65.4 MPa and the siliceous mudrocks have an average UCS of 44.1 MPa. These values are very similar for the same facies observed in the Wolfcamp Formation in the Delaware Basin from this study. For the Wolfcamp in the Delaware Basin from the Thunder C20-13 #2H core, the skeletal packstone and siliceous mudstone have an average UCS of 65.4 MPa and 46.9 MPa, respectively.

The relationship between rock strength and lithology can also be seen stratigraphically. In Figure 4.9, core-derived UCS measurement was plotted as a function of depth for the Wolfcamp A, B, C, and D. The scale shows UCS ranging from 30 to 70 MPa. The color fill of the curves coincides with the lithofacies observed from core description at that depth. Higher rock strengths were primarily observed corresponding to the calcareous facies, shown in blue. Lower rock strength intervals are dominantly the siliceous and argillaceous facies, shown in yellow and brown. The abundant facies and rock strength changes seen from the 10 ft section in Figure 4.7 show that variations in rock strength can occur over short distances. The location of the 10 ft core in Figure 4.7 is noted in the pink rectangle in Figure 4.9.

In the Wolfcamp A, beds appear highly stratified and thinly bedded in both lithology and rock strength. The Wolfcamp A shows an abundance of high rock strength, carbonate intervals interbedded with intermediate to low rock strength beds. In the Wolfcamp B, UCS values are highly stratified, but thicker sections of moderate- to low-rock strength can be seen. Thin spikes showing higher rock strength beds are present throughout the interval from carbonate-rich beds. The rock strength profile for the top 40 ft of the Wolfcamp C looks comparable to the base of the Wolfcamp B. The lowest overall rock strength can be seen from 11,434 ft to 11,503 ft and is dominated by clay-rich lithofacies. The blocky nature of the UCS curve is due to the lower sampling resolution within this zone. The argillaceous mudstone that makes up a bulk of this interval often shows partings at contacts with other lithologies. These partings extenuated by dehydration cracks, limit sampling locations stable enough for UCS measurements. The enlarged section at the top of the

Wolfcamp D shows clay-rich, low rock strength strata with thin beds of high rock strength carbonate in between low rock strength argillaceous mudstone.

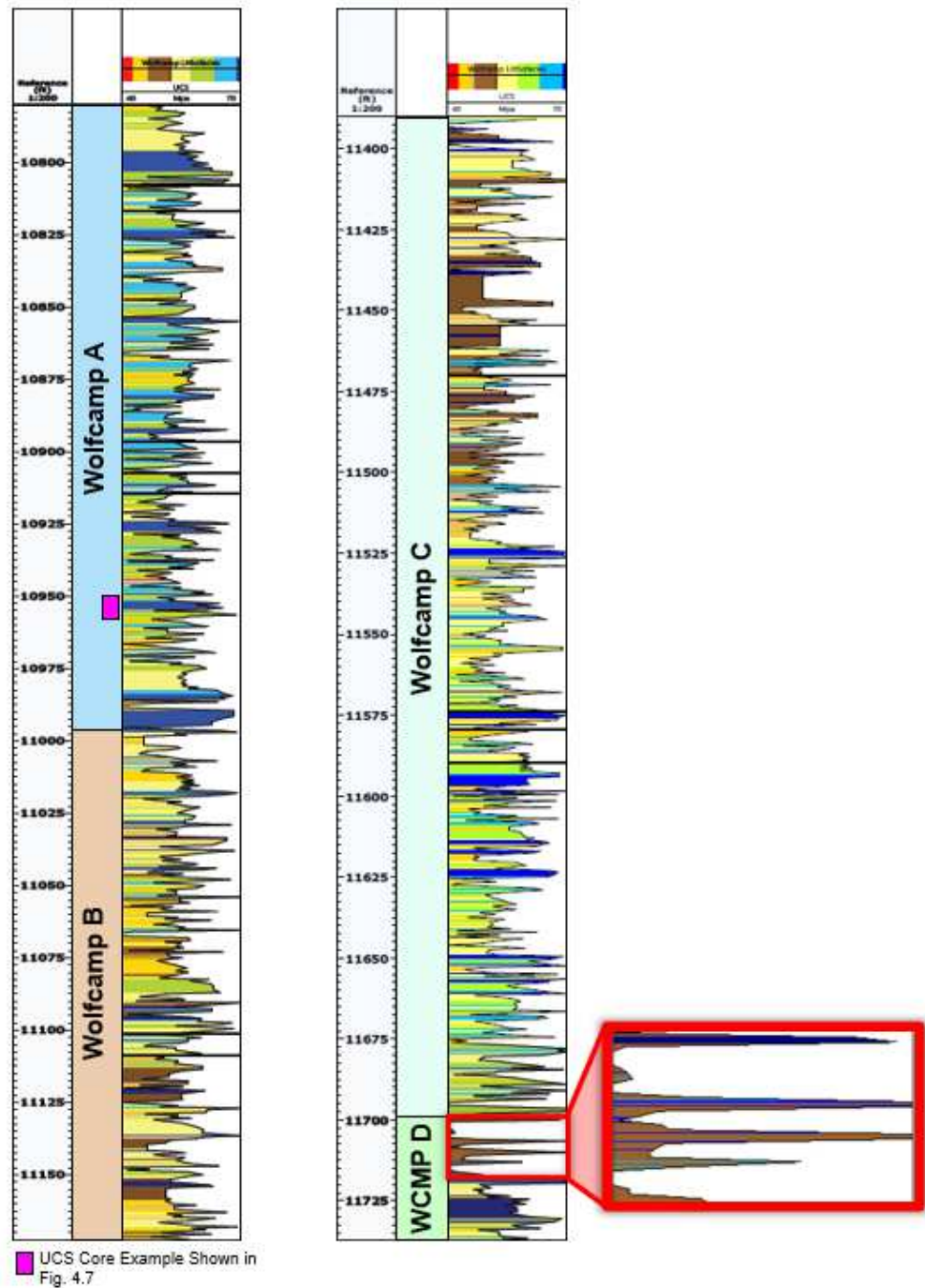


Figure 4.9—Unconfined compressive strength (UCS) calculated from core displayed stratigraphically as a function of depth for the Wolfcamp A, B, C, and D. UCS track ranges from 30 to 70 MPa. UCS curve is colored based on associated lithofacies from core description. The enlarged section from the Wolfcamp D shows subtle facies changes with contrasting high and low rock strength.

4.2.2 Brittleness

Brittleness is a material's tendency to fracture when subjected to stress with little to no deformation before rupture. Characteristics of brittle materials include high compressive strength, low tensile strength, low tendency to deform, and poor ability to resist impact and load. Conversely, ductile materials are more prone to bend with external stress (Zhang, 2011). The primary objective of fracture stimulation is to initiate and maintain a fracture network to improve conductivity and optimize well productivity and recovery. Ductile rocks are more prone to closing fracture networks and lower fracture conductivity. Furthermore, larger quantities of proppant are required as proppant embedment is more inclined to occur in ductile rocks (Britt, 2012).

The brittleness index (BI) is a parameter used to quantify brittleness based on examining brittle and ductile mineral content in a rock (Mathia et al., 2016; Buntoro et al., 2018). Quartz, feldspars, calcite, dolomite, and pyrite are minerals that are more prone to brittle behavior. Clays and organic matter in sediment are more prone to ductile behavior (Jin et al., 2015; Kang et al., 2020). The BI equation, originally proposed by Jarvie and others (2007), was further modified by authors including Diaz and others (2013) and Xu and Sonnenberg (2016), as seen in the following equation:

$$MBI = \frac{Quartz_{wt\%} + Kfeldspar_{wt\%} + Plagioclase_{wt\%} + Calcite_{wt\%} + Dolomite_{wt\%} + Pyrite_{wt\%}}{Quartz_{wt\%} + Kfeldspar_{wt\%} + Plagioclase_{wt\%} + Calcite_{wt\%} + Dolomite_{wt\%} + Pyrite_{wt\%} + Clays_{wt\%} + TOC_{wt\%}} \quad (4.6)$$

The mineral-based brittleness index was calculated using mineralogical data from XRD. To investigate the compositional controls on brittleness, MBI was crossplot against the three key mineral groups—QFM, carbonates, and clays (Fig. 4.10). The amount of total clay is the strongest driver on MBI calculated using this method. The highest brittleness index was shown in the samples with the lowest clay content. For example, the carbonate-rich facies have high brittleness due to the lack of ductile constituents, including clays and organic matter. Calcite cements, seen in thin section, also contribute to higher brittleness and rock strength. In contrast, an increase in clay content coincides with a decrease in brittleness. Clay-rich facies with the lowest brittleness index are more prone to ductile behavior. Carbonate content to MBI shows a moderate correlation ($R^2=0.43$). No relationship was observed between QFM and MBI ($R^2=0.01$).

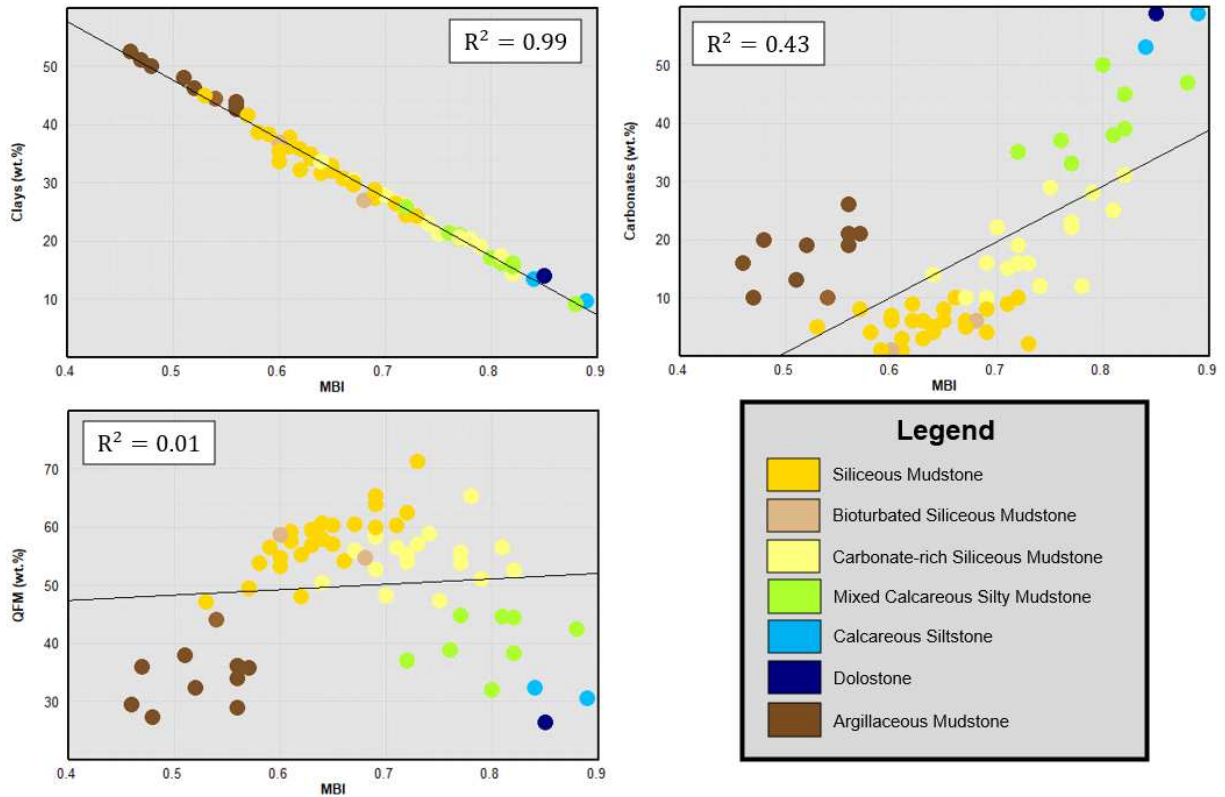


Figure 4.10—Crossplots of calculated mineral-based brittleness index (MBI) as a function of composition (clays, carbonates, and QFM).

4.2.3 Natural Fractures

Natural fractures were observed in all lithologies in the Wolfcamp through multiple scales. Three primary groups of fractures were identified, including vertical fractures, horizontal “beef” fractures, and faults (Fig 4.11.A-C). Vertical to near-vertical cemented fractures (Fig. 4.11.A) were the most common type of fracture observed throughout the Wolfcamp intervals. These fractures can range from less than 1 ft to several feet long, cutting through multiple beds with varying lithologies. Some terminate within the middle of beds or abruptly against a change in lithology or rock strength. Termination of vertical fractures were also seen against beef fractures. Near-vertical fractures occur the most in lithofacies associated with calcareous and siliceous facies groups and less common in thick (over several feet) sections dominated by clay-rich, argillaceous mudstone. Isotope analysis of fracture cements along with analysis of fluid inclusions by Gale and others (2017) suggested that the vertical fractures in the Wolfcamp were formed during the

Cenozoic uplift. Hydrocarbon-bearing fluid inclusions from both vertical and horizontal fractures suggest their occurrence formed during or after hydrocarbon generation.

Other fractures observed that are less pervasive than vertical fractures, but are still common, include beef fractures and microfractures. Beef fractures are found frequently throughout the Wolfcamp Formation. However, their occurrence appears to be related to the richest source rocks, the siliceous mudstone facies. Beef fractures are bedding parallel, fibrous, calcite-filled fractures associated with organic-rich, overpressured source rocks found worldwide (Al Duhailan et al., 2015; Ma et al., 2016; Larmier et al., 2018). In the Wolfcamp, beef fractures are found in the siliceous mudstones and are absent in other organic-lean facies (Fig. 4.11.C). Microfaults are primarily observed at lithology contacts between the argillaceous mudstone, with the overlying siliceous mudstone or underlying siltstone (Fig. 4.11.B). Both normal and reverse faults were observed and most have small offsets of less than 0.4 inches. Microfaults also occur in mass transport deposits. Cemented fractures can also be found in thin section from proprietary photomicrographs in the Thunder C20-13 #2H well. Similar microfractures were observed in siliceous mudstones with quartz-filled cemented fractures from the Wolfcamp Formation in Ward county (Fig. 4.11.D).

The Thunder C20-13 #2H well was part of a detailed core fracture characterization by Salem and others (2018) that evaluated over 6,500 ft of core from 16 wells throughout the Delaware Basin. From their study, fracture intensity appears to be lithology-related and most common in the brittle lithofacies. The relationship between fracture intensity to well production and water-oil ratio (WOR) was also investigated within the study. Implications of natural cemented fractures in the Wolfcamp show that fractures can be initiated and propagated in multiple intervals. While vertical fractures are common, they are likely undersampled in vertical cores with a 3-inch diameter. Fractures commonly found in the small diameter of the cored section suggest that the Wolfcamp likely contains extensive natural fracture networks.

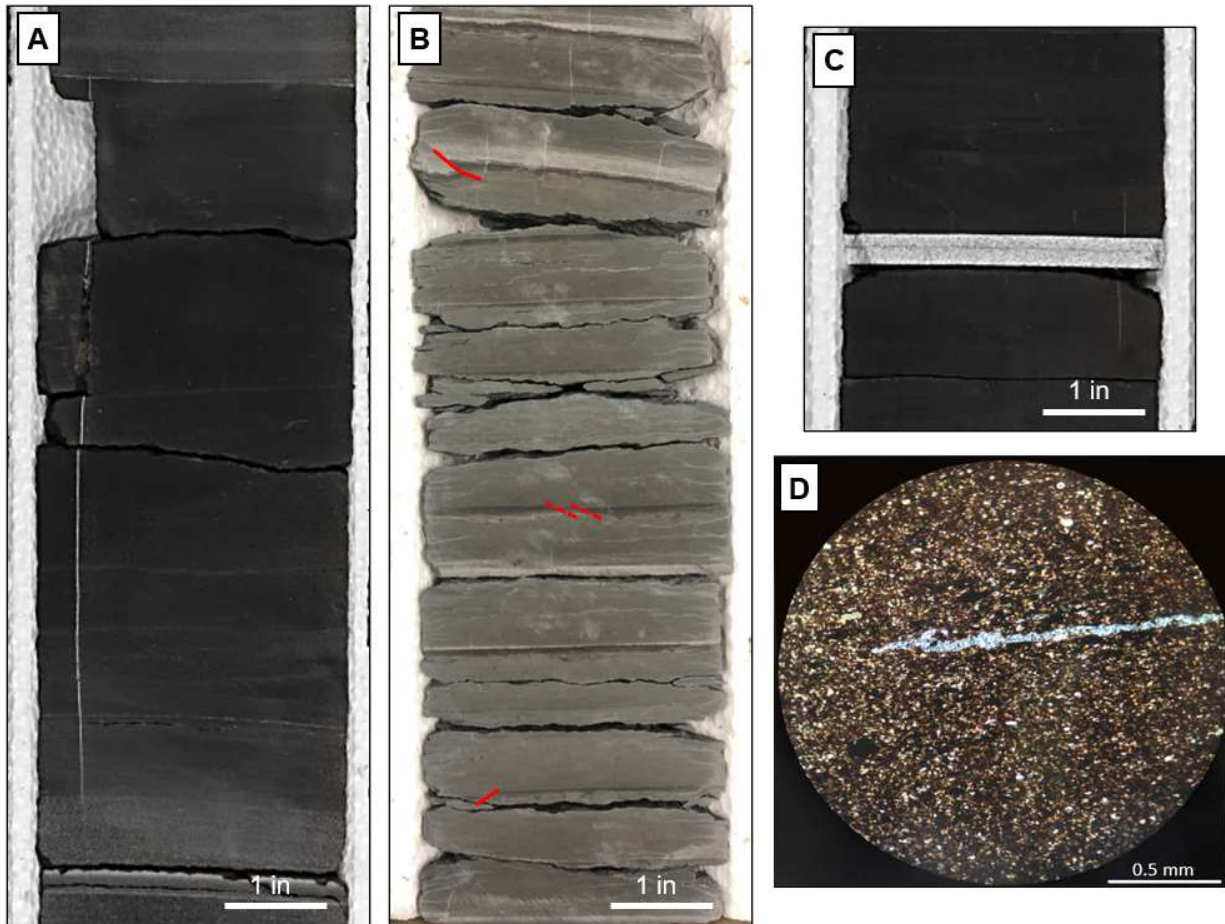


Figure 4.11—Types of natural fractures and microfaults observed in Wolfcamp core. A) vertical fracture through calcareous siltstone and mudstone facies, terminating at the base of a bed (top) and within a bed (bottom). B) Microfaults (shown in red), primarily found associated with the argillaceous mudstone. C) Horizontal “beef” fracture found in siliceous mudstone; small vertical fracture can be seen potentially propagating from beef fracture. D) Quartz-filled fracture in thin section from the siliceous mudstone (Wolfcamp) in Ward County.

4.3 Reservoir Properties (Porosity, Permeability, and Fluid Saturations)

The evaluation of reservoir properties is essential for reservoir characterization and in determining if facies are more prone to have reservoir or nonreservoir qualities. In this study, XRD was used to quantify mineral components of lithofacies. This is integrated with Routine Core Analysis (RCA) data, including TOC, porosity, permeability, and fluid saturations (Table 4.3). The addition of rock strength (UCS) data was also used to characterize and differentiate facies.

Table 4.3—Average mineral constituents and reservoir properties for the Wolfcamp lithofacies analyzed from X-ray Diffraction (XRD) and Routine Core Analysis (RCA).

Lithofacies	Mineral Groups (wt.%)				Reservoir Properties				Count, n (-)
	QFM	Clays	Carbonates	Others	Porosity, Φ (%)	Permeability, k (nD)	Total Organic Carbon, TOC (wt.%)	Water Saturation, S_w (%)	
Argillaceous Mudstone	35.6	45.9	16.1	2.5	9.9	1.3	0.4	83.5	11
Siliceous Mudstone	58.2	32.8	5.0	4.0	9.4	57.9	2.6	51.4	26
Bioturbated Siliceous Mudstone	54.7	26.9	5.3	13.1	8.5	108.0	1.7	35.8	1
Carbonate-rich Siliceous Mudstone	54.6	23.9	18.2	3.2	8.0	44.8	2.3	47.5	17
Mixed Calcareous Silty Mudstone	40.8	18.1	38.6	2.6	7.1	103.7	2.2	35.9	9
Calcareous Siltstone	31.4	11.6	54.1	3.0	5.7	59.7	1.8	37.3	2
Dolostone	26.4	14.0	58.3	1.3	6.1	11.2	0.7	41.3	1

From the evaluation of LECO TOC data in Chapter 4.1.1, TOC ranges from 0.15 to 6.30 wt.%. The most organic-lean facies analyzed include the argillaceous mudstone and dolostone lithofacies. The argillaceous mudstone has TOC ranging from 0.15 to 1.08 wt.%, with an average of 0.40 wt.%. Only one sample for dolostone was available for RCA, indicating TOC of 0.66 wt.%. Organic-rich facies, with average TOCs of greater than 2 wt.%, are the siliceous mudstone, carbonate-rich siliceous mudstone, and mixed calcareous silty mudstone lithofacies. The most organic-rich facies is the siliceous mudstone with TOC ranging from 1.48 to 6.30 wt.% and an average TOC of 2.59 wt.%. The carbonate-rich siliceous mudstone and mixed calcareous silty mudstone have TOC ranging from 1.12 to 3.59 wt.% (avg. 2.3 wt.%) and 1.40 to 2.74 wt.% (avg. 2.2 wt.%), respectively.

Porosity and permeability are microscopic-scale rock properties that control the storage and ability of flow in a reservoir rock. The porosities and permeabilities analyzed from the Wolfcamp range from 4.54 to 12.13 percent and 0.1 to 340 nD, respectively. Porosity refers to the percentage of pore or void space present within the total rock volume. The most

porous rocks from the Wolfcamp are the argillaceous mudstone, siliceous mudstone, bioturbated siliceous mudstone, carbonate-rich siliceous mudstone, and mixed calcareous silty mudstone with an average porosity of greater than seven percent. Porosity is the storage capacity for fluids. Permeability is a measure of a material's ability to transmit fluid through interconnected pore spaces or the flow capacity of a rock expressed in units of millidarcies (mD) or nanodarcies (nD). While the argillaceous mudstone has the highest average porosity at 9.9 percent, it also has extremely low permeabilities. The argillaceous mudstone has permeabilities ranging from 0.1 to 4.1 nD and an average permeability of 1.3 nD, which is unfavorable for a reservoir rock. The dolostone also has low permeability at 11.2 nD.

Fluid saturations are another important reservoir property considered for characterization. Hydrocarbon saturation is primarily attributed to gas saturation ranging from 7.3 to 70.2 percent. Oil saturation ranges from 0.1 to 34.1 percent. Water saturation is a geoscience parameter used in reservoir modeling. From RCA, water saturation ranges from 17.6 to 92.1 percent. The highest water-bearing facies is the argillaceous mudstone, with an average water saturation of 83.5 percent. Other lithofacies have significantly less average water saturation ranging from 35.8 to 51.4 percent.

Additional data collected for unconfined compressive strength to quantify rock strength was used for evaluation. As discussed in Chapter 4.2.1, the average rock strength is the hardest for carbonate-dominated rocks, including packstones (65.4 MPa), wackestones (62.4 MPa), dolostones (61.8 MPa), and calcareous siltstones (59.2 MPa). The lowest average rock strengths are associated with lithofacies that have higher clay content, including the argillaceous mudstone (44.7 MPa) and siliceous mudstone (46.9 MPa). From MBI calculations as a method to assess brittleness, clay content has the largest control on brittleness. MBI was the highest in carbonate-dominated rocks due to low ductile materials such as clays and organic matter. Clay-rich facies with low rock strength and low MBI are more prone to ductile behavior. Ductile rocks are more susceptible to closing fracture networks, lower fracture conductivity, and proppant embedment.

4.4 Reservoir and Nonreservoir Rocks

The objective of analyzing lithofacies and their properties is to examine their implications for oil and gas production. Reservoir properties discussed in the previous section were used to evaluate lithofacies that are more prone to be reservoir or nonreservoir rocks. Four reservoir and nonreservoir designations along with the associated lithofacies and average reservoir properties can be seen in Figure 4.12 below.

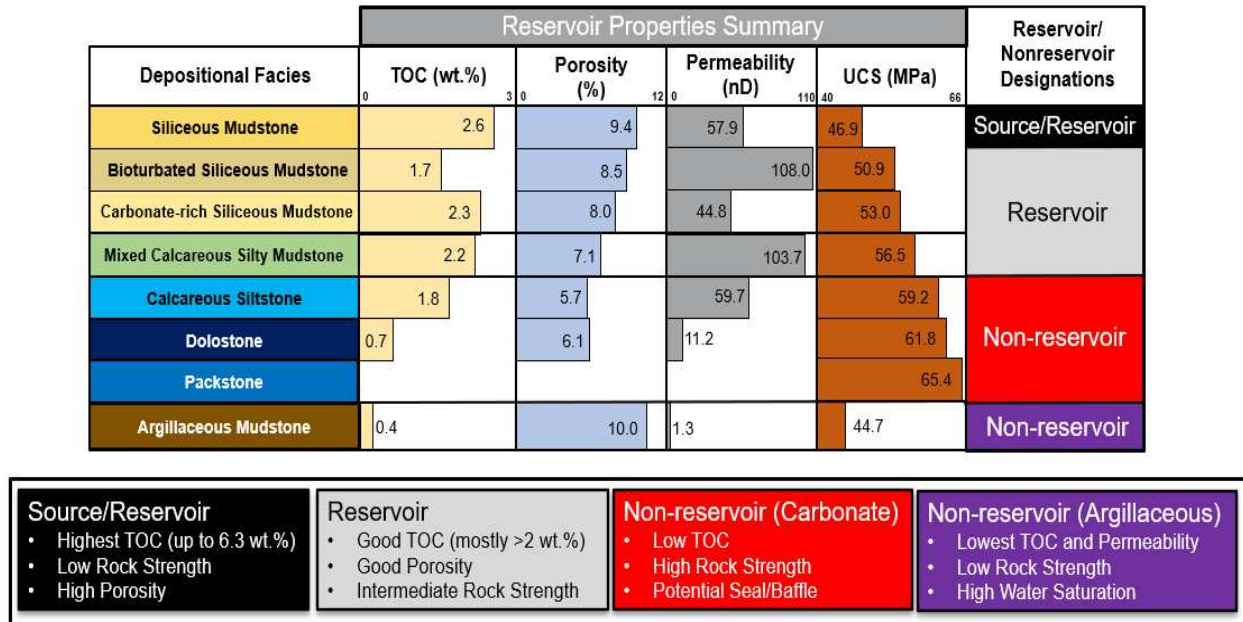


Figure 4.12—Summary of the average reservoir properties for the Wolfcamp lithofacies and interpreted reservoir/nonreservoir designation.

Two reservoir designations with favorable reservoir characteristics include the following: (1) source/reservoir and (2) reservoir. The source/reservoir designation is best represented by the siliceous mudstone lithofacies. The siliceous mudstone has the highest average TOC at 2.6 wt.%, up to 6.3 wt.%. It has one of the highest average porosity values at 9.4 percent and moderate average permeability at 57.9 nD. The siliceous mudstone has low rock strength at an average of 46.9 MPa for UCS. The reservoir designation is best represented by the bioturbated siliceous mudstone, carbonate-rich siliceous mudstone, and mixed calcareous silty mudstone. These lithofacies have the following qualities: generally good TOC (greater than 2 wt.%), high porosities, good permeabilities, and intermediate rock strength. The bioturbated siliceous mudstone has TOC of 1.7 wt.% from one RCA sample. However, the bioturbated siliceous mudstone is primarily found along with the

siliceous mudstone or carbonate-rich siliceous mudstone in a normal stacking pattern. These four lithofacies under the source/reservoir and reservoir designations have the most favorable reservoir properties.

Two nonreservoir designations can be seen in red and purple from Figure 4.12. While both nonreservoir designations have less favorable reservoir properties, the reservoir properties that characterize each designation differ from one another. The red nonreservoir carbonate facies is characterized by having low TOC (under 2 wt.%), low porosity, and high rock strength. It includes carbonate-rich lithofacies of the calcareous siltstone, dolostone, wackestone, and packstone. The purple nonreservoir argillaceous designation is best represented by the argillaceous mudstone lithofacies. Characteristics of the nonreservoir argillaceous designation are low TOC, high porosity, very low permeabilities, and low rock strength. The argillaceous mudstone also has the highest water saturation. Both nonreservoir designations can be detrimental as potential seals or baffles, depending on the thickness and frequency of units.

4.5 Core Analyses to Log Scale

This section aims to integrate core analyses, including lithofacies, reservoir properties, and reservoir/nonreservoir designations, to associated well log signatures. Wireline log data is the most common tool used to prospect, interpret lithology, and understand rock and fluid properties. A normal well log suite consisting of four tracks was used for this study, as seen in the following:

- 1) Track 1: Caliper (CALI), gamma ray (GR), and spectral gamma ray (SGR)
- 2) Track 2: Shallow to deep resistivity (RSHAL, RMED, RDEEP)
- 3) Track 3: Density porosity (DPHI) and neutron porosity (NPHI)
- 4) Track 4: Photoelectric factor (PEF)

Caliper logs are used to measure the diameter of the hole size continuously as a function of depth. Caliper logs are primarily used for volume calculations for cementing as well as a qualitative indicator for wellbore quality and hole condition throughout the borehole (Bratton, 2014). Track 1 typically contains the caliper and gamma ray logs.

Standard gamma ray logs are used for correlation and to differentiate between shale versus non-shale lithologies. The gamma ray tool measures the total count of natural radiation (U-K-Th) emitted from the formation. Clean, shale-free sandstones and carbonates have low concentrations of radioactive elements and will produce low gamma ray readings. As shale content increases, total gamma ray typically increases concurrently due to higher concentrations of radioactive elements. The color gradient used for total gamma ray in this study is aimed to be a quick look method to differentiate lithologies common to the Wolfcamp Formation based on cutoff recommendations from Kvale and others (2020).

The wireline total gamma ray cutoffs and corresponding lithology estimates used include the following:

- Light blue (<55°API): Calciclastics dominated by carbonate rock fragments and carbonate cement, including skeletal packstones, dolostones, and wackestones.
- Light gray (55 to 80°API): Intermediate calcareous and muddy facies, including muddy wackestones, siltstones, and calcareous silty mudstones to calcareous mudstones.
- Dark gray (>80°API): Slightly calcareous to noncalcareous mudstones.

The normal gamma ray log response is composed of a combination of naturally occurring radiation from elements of K, Th, and U. Since different isotopes have characteristic energy spectrums, the energy of the gamma ray emitted differs based on the elements that source them. A spectral gamma ray tool measures the number of natural gamma rays as a function of their energy spectrum (Asquith and Krygowski, 2004). As discussed in Chapter 4.1.1, the uranium component from spectral gamma ray can be used to approximate organic matter content as seen by the positive correlation between SGR_U to core-derived TOC. Corrected gamma ray, CGR or GR_{TK} , is the total gamma ray minus uranium (Bratton, 2014). By plotting corrected gamma ray along with total gamma ray, the separation between the two curves, shaded in orange, is the uranium concentration. The shaded orange uranium concentration is used as a proxy for organic content and approximating organic-rich to organic-lean intervals.

Resistivity is the ability of a material to resist the flow of electricity. Resistivity tools emit a current into the adjacent formation and measures the response of the formation to the current. The primary use of resistivity logs is for fluid identification to determine hydrocarbon-bearing versus water-bearing zones. Most minerals that make up the matrix and hydrocarbons are nonconductive. Therefore, the ability of a current to be transmitted through the subsurface is a function of water saturation within the pore space. When hydrocarbon saturation increases, formation resistivity increases. If the salinity within formation waters decreases, resistivity also increases (Asquith and Krygowski, 2004). Multiple resistivity curves, varying in depth of investigation, are used to understand the formation at different distances from the borehole. Shallow resistivity (RSHAL) measures the resistivity in the flushed zone. The flushed zone is directly adjacent to the borehole. Due to flushing, the volume of fluids within the flushed zone varies from the fractional volume of fluids in uninvaded zones (Bratton, 2014). Intermediate resistivity (RMED) measures resistivity in the zone of transition or annulus. Deep resistivity (RDEEP) measures resistivity in the uninvaded or undisturbed zone that is not affected by the drilling process. Deep resistivity is also the true formation resistivity (Asquith and Krygowski, 2004). To differentiate high and low resistivity units within the Wolfcamp Formation, cutoffs were applied. For values less than 20 ohm-m, solid red is applied to indicate low resistivities. Values of 20 ohm-m or more are colored in a spectrum to discern spikes in high resistivities.

Density and neutron logs are nuclear measurements that in combination provide good sources of porosity data, particularly in complex lithologies (Hartmann and Beaumont, 1991). Density tools emit gamma rays that collide with electrons in the formation that result in energy loss. These gamma rays are returned to detectors in the tool in two energy ranges. First, the number of higher energy range gamma rays that return to the tool is related to the formation bulk density (RHOB). The formation bulk density is a function of formation matrix density, fluid density, and density porosity. The formation matrix density is the density of the solid framework in a rock. Fluid density is the density of fluid within pores, which can differ based on saltwater mud, freshwater mud, or hydrocarbons. Density porosity (DPHI) is calculated from formation bulk density by a wellsite geologist or

engineer in the logging unit specifying the matrix and fluid densities for the location. A neutron log measures the concentration of hydrogen in a formation.

A neutron logging tool emits neutrons from a source continuously. Since a hydrogen atom is almost equivalent to the mass of a neutron, the collision between an emitted neutron to a hydrogen atom in the formation results in the largest energy loss. Hydrogen is primarily found in fluids within the pore space of a formation. As a result, the neutron log measures fluid-filled porosity (NPHI). DPHI and NPHI can be used concurrently to provide quick-look insights to lithology and gas saturations. In this study, DPHI is displayed in a red solid line and NPHI is shown in a blue solid line in Track 3. When there are high clays in the formation matrix, the detected NPHI values are inflated and greater than the actual formation porosity. In zones that have high clay content, the logging tool detects hydrogen within the pore space in addition to excess hydrogen within the clay structure and clay-bound water. Since the processing software for the neutron tool accounts for all hydrogen to be within the pore space, it elevates neutron porosity readings. The inflated neutron porosity due to the presence of clay is referred to as the “shale effect.” The separation between the elevated, high neutron porosity and density porosity is shown shaded in gray for the two curves ($NPHI > DPHI$). Since neutron porosity responses are affected by the volume of clays present in the formation, the degree of separation between neutron porosity and density porosity can be used to qualitatively estimate the amount of clay within an interval (Asquith and Krygowski, 2004).

Neutron porosity and density porosity curves are also affected by gas saturations. Gas has lower concentrations of hydrogen atoms compared to oil and water. As a result, gas in pore spaces lower neutron porosity measurements. Gas also has a lower density than oil and water, which affects density porosity. In gas prone zones, the neutron porosity curve is less than the density porosity curve, creating a porosity crossover. The crossover is shaded in red between the two porosity curves ($NPHI < DPHI$). For the Thunder C20-13 #2H well, the density porosity curves reference a limestone matrix. As a result, when neutron porosity and density porosity curves track closely and overlay one another ($NPHI \sim DPHI$), it shows that the predominant lithology is limestone within that interval.

The density tool that measures formation bulk density and quantifies density porosity, also concurrently detects a lower energy range. This lower energy range is affected by the photoelectric effect (Crain, 1986). The photoelectric factor (PEF) is related to the average atomic number (Z), which can be seen in the following equation:

$$PEF = \left(\frac{Z}{10}\right)^{3.6} \quad (4.7)$$

Measurements of PEF are in units of barns/electron (b/e). Photoelectric factor increases with an increase in the average atomic number, which is related to the lithology of the formation the logging tool encounters. As a result, PEF is strongly a function of the lithology of the rock matrix, negligible to pore fluids, and only very slightly affected by porosity (Asquith and Krygowski, 2004). The PEF curve is useful in identifying lithologies. For sandstones and clastics that have lower PEF values, a cutoff of 2 b/e or less is used (shaded in yellow). For carbonates, including limestone and dolostone, that have higher PEF values, a cutoff of 4 b/e or higher is used (shaded in blue). Using the log set up and analysis methods described above, the Thunder C20-13 #2H log suite was evaluated. The Wolfcamp Formation in the Delaware Basin shows distinct log characteristics in the normal logging suite for gamma ray, resistivity, porosity curves, and PEF. The discussion on reservoir characterization involves integrating core- to log-scale analyses for the various Wolfcamp intervals. The integrated core analyses to log can be seen in Figure 4.13 for the Wolfcamp A and B and Figure 4.14 for the Wolfcamp C and D.

4.5.1 *Wolfcamp A*

The top of the Wolfcamp Formation, equivalent to the top of the Wolfcamp A, is marked by a high gamma ray spike and high resistivities from the overlying Bone Spring Formation. The X- and Y-Sands are sandy to silty turbidite lobe packages that are found in the north-central region of the Delaware Basin (Driskill et al., 2018). The X- and Y-Sands are characterized by low to moderate gamma ray and low resistivities. During the Upper Wolfcampian to Lower Leonardian, waning icehouse conditions resulted in global relative sea level rise. As sea level rose, carbonate shelves were flooded, causing repeating platform failure that triggered the mobilization of shelfal debris down structurally steepened ramps into the basin (Playton and Kerans, 2002; Baumgardner et al., 2016; Kvale et al., 2020).

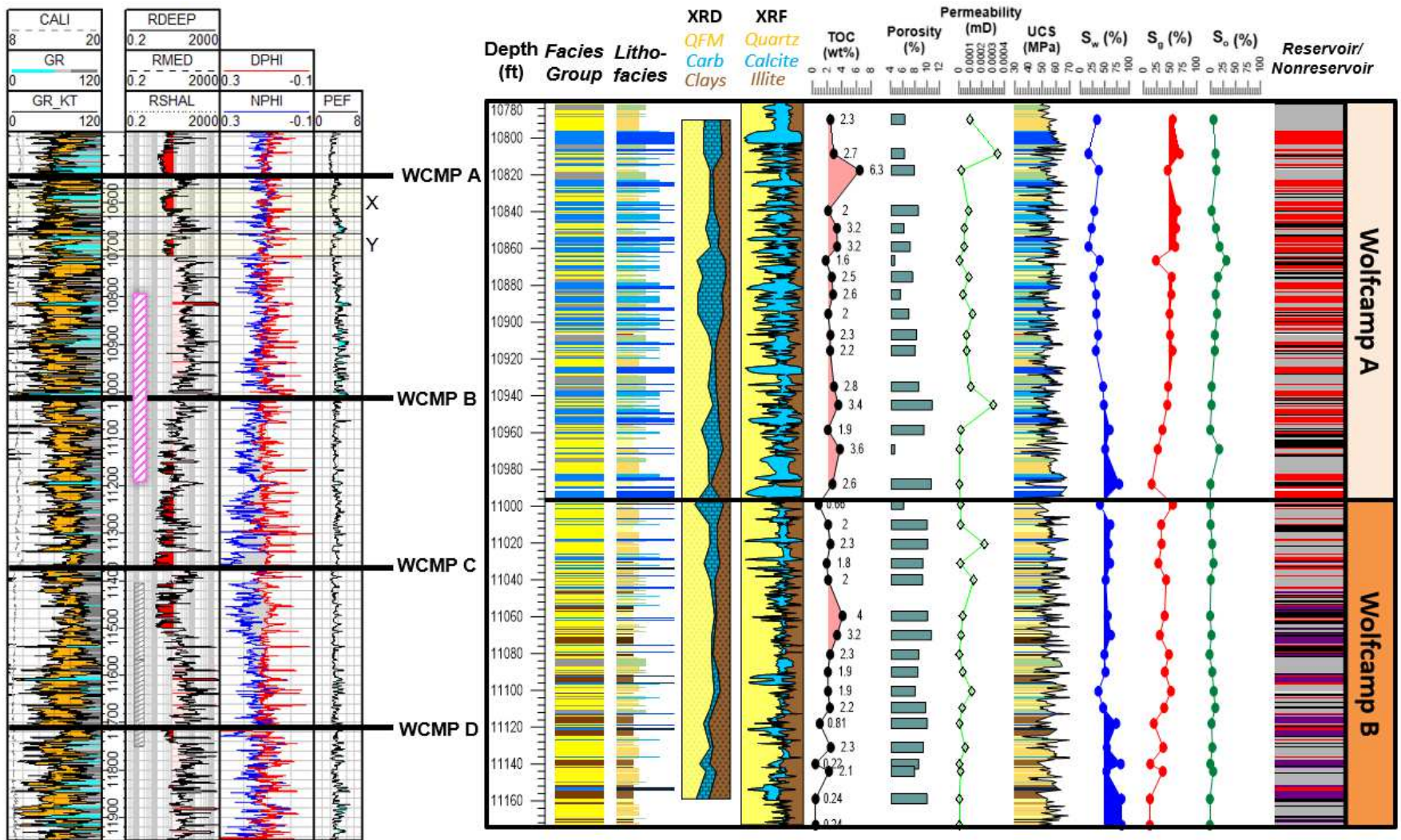


Figure 4.13—Integrated core analyses (including core description, XRD, XRF, RCA, UCS, and reservoir/nonreservoir designation) to associated well log curves for the Wolfcamp A and B.

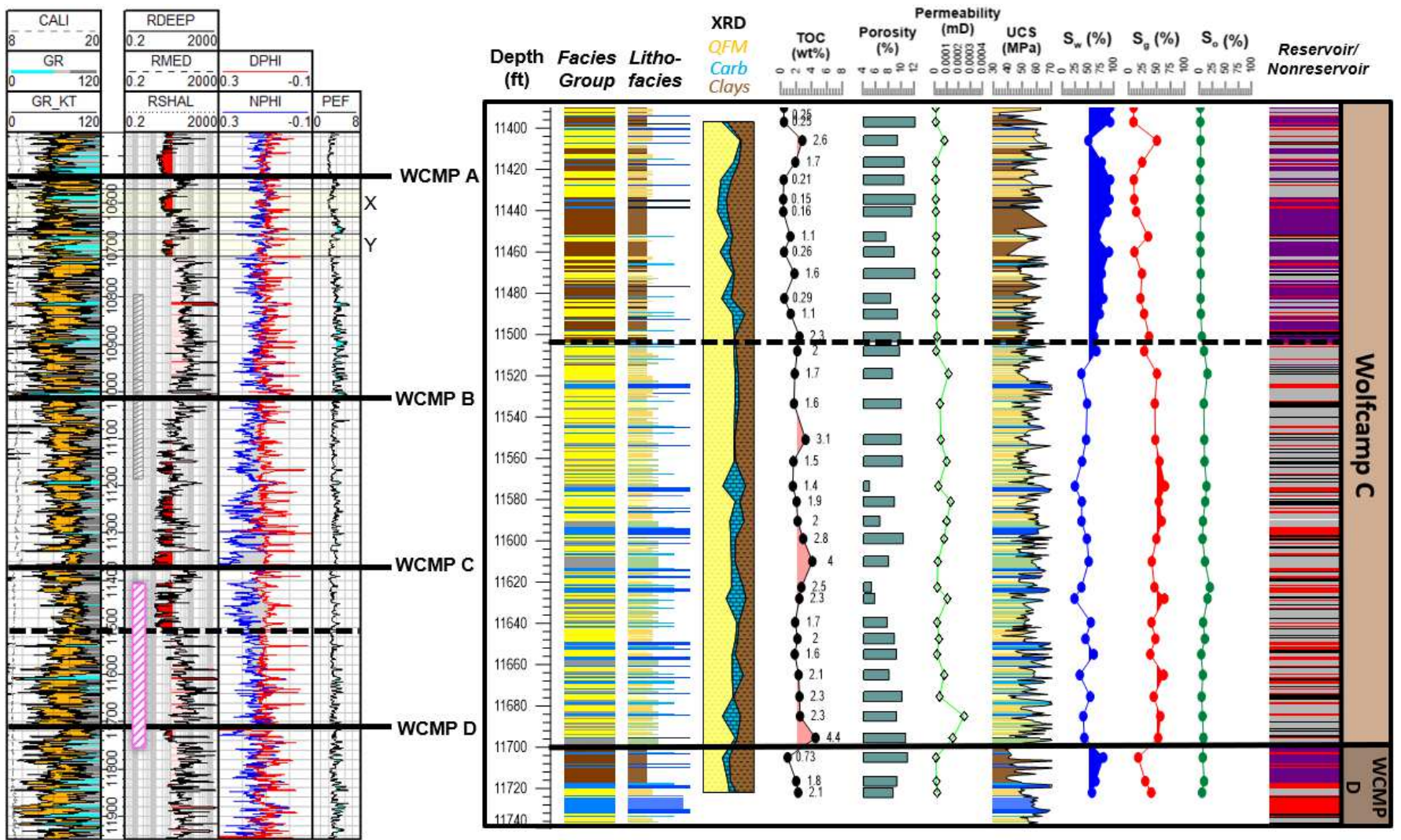


Figure 4.14—Integrated core analyses (including core description, XRD, RCA, UCS, and reservoir/nonreservoir designation) to associated well log curves for the Wolfcamp C and D.

From core analysis, cyclic sediment gravity flow deposits of upward fining sequences comprise a majority of the Wolfcamp A. These carbonate sediment gravity flow deposits vary in thickness (ranging from inch- to foot-scale) and are separated by thinner hemipelagic deposits. These hemipelagic deposits are enriched in organic matter with elevated paleoredox-sensitive elemental indicators, suggesting periods of suboxic to anoxic bottom conditions at the time of deposition. Dominant facies groups and lithofacies observed from core reflect the mentioned deposits. The Wolfcamp A is comprised of the calcareous facies group (38.5%), siliceous facies group (37.0%), and mixed facies group (24.5%). Lithofacies in the Wolfcamp A include the following: packstone (18.0%), calcareous siltstone (20.7%), mixed calcareous silty mudstone (24.5%), carbonate-rich siliceous mudstone (17.8%), and siliceous mudstone (17.7%).

Cyclic deposition of compositionally-stratified, carbonate sediment gravity flow deposits results in a higher overall influx of carbonate debris. The fining upwards nature of event beds, from calcareous facies to mixed and siliceous facies, result in the interbedded nature distinctive of the Wolfcamp A. This can be seen through facies distribution, XRF elemental-to-mineral calculations, and well log signature (Fig. 4.13). Subsequently, it also impacts the reservoir properties observed in the Wolfcamp A. The basal carbonate-rich beds in an event bed, the packstone lithofacies, has low TOC (<1 wt.%), low porosities (<4%), and high rock strength (avg. 65.4 MPa). As the event bed fines upward, the calcareous to noncalcareous mudstones of the mixed calcareous silty mudstone, carbonate-rich siliceous mudstone, and siliceous mudstone lithofacies can be seen. These lithofacies from intermediate to top of the event bed show more favorable reservoir properties, including higher average TOC (>2 wt.%) and higher average porosities (>7%).

RCA data, measured at approximately 10-foot intervals for the Wolfcamp A, shows porosities ranging from 4.5 to 10.7 percent, with an average of 7.4 percent. Permeabilities range from 1 to 340 nD, with an average of 83 nD. Compared to RCA from other Wolfcamp intervals, gas and oil saturations are highest in the Wolfcamp A, averaging 49.2 and 12.0 percent, respectively. Water saturation is lowest in the Wolfcamp A, with an average of 38.8 percent. Using the classification of reservoir to nonreservoir prone rocks interpreted for this study, the cored interval of the Wolfcamp A is comprised of 61.3 percent reservoir

rocks and 38.7 percent nonreservoir rocks (Fig. 4.15). Zones that are more prone to unfavorable reservoir properties in the Wolfcamp A are composed of nonreservoir carbonate rocks.

The wireline log characteristics of the Wolfcamp A are distinct. The total gamma ray log, shows thin beds of high to low gamma ray displayed in a “comb-like” signature. This reflects on the change in facies in an event bed or multiple event beds. Below the Y-sand base, the interval shows high resistivities with porosity curves that primarily overlay one another (NPHI ~ DPHI). The PEF curve shows an abundance of beds that have PEF greater than 4 b/e. The pervasive low gamma ray spikes, closely aligned porosity curves, and high PEF beds capture the overall high carbonate content from the high-frequency, cyclic carbonate sediment gravity flows that dominate the stratigraphic record of the Wolfcamp A. Looking at the uranium content from spectral gamma ray as a proxy for TOC, highlighted in orange (Track 1), uranium content in the Wolfcamp A is the highest in zones with high gamma ray, particularly in beds that have over 80 °API.

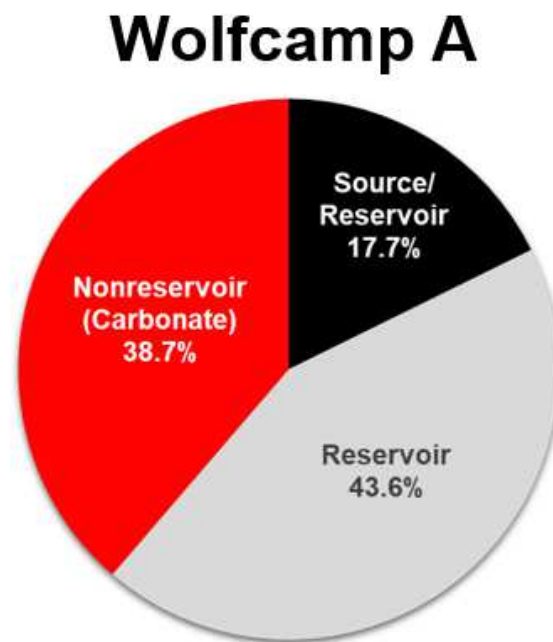


Figure 4.15—Pie chart of reservoir vs. nonreservoir prone rocks based on reservoir properties for the Wolfcamp A cored interval. The Wolfcamp A is comprised of 61.3% reservoir prone rock. Nonreservoir prone rock only includes nonreservoir (carbonate) rocks that represent 38.7% of the interval.

4.5.2 *Wolfcamp B*

Core examined from the Wolfcamp B, show that facies are comprised of the siliceous facies group (55.8%), argillaceous facies group (20.3%), mixed facies group (12.5%), and calcareous facies group (11.3%). Lithofacies in the Wolfcamp B include the following: siliceous mudstone (19.3%), carbonate-rich siliceous mudstone (29.6%), bioturbated siliceous mudstone (6.9%), mixed calcareous silty mudstone (12.8%), calcareous siltstone (4.1%), packstone (4.2%), and dolostone (3.9%). Both lithofacies distribution from core description and XRF elemental analysis show a significant decrease in carbonate lithofacies. Thin carbonate-rich beds are present at the top of the Wolfcamp B, as indicated by core description and the XRF mineral model. The siliceous facies group is dominant in the Wolfcamp B along with a substantial portion of strata from the argillaceous facies group. Both of these facies groups are composed of mudstones.

The overall higher proportions of mudstones with more minor contributions from carbonates in the Wolfcamp B influence the reservoir properties observed. The abundance of mudstones shows overall higher porosities seen in the Wolfcamp B. Water saturation is overall higher in the Wolfcamp B compared to the Wolfcamp A. The highest water saturations coincide with an increase in argillaceous mudstones seen towards the base of the Wolfcamp B cored interval. Argillaceous mudstones in the Wolfcamp B are characterized by high clay content (41.5 to 44.4 wt.%), high water saturations (74.9 to 85.6%), high porosity (8.5 to 9.9%), very low permeability (0.5 to 1.5 nD), and poor TOC (0.2 to 0.8 wt.%). Reservoir prone lithofacies make up 68.4 percent of the cored interval. RCA data shows that reservoir prone rocks have porosities ranging from 7.8 to 10.6 percent, permeabilities from 8 to 197 nD, TOC from 1.8 to 4.0 wt.%, water saturations from 38.1 to 63.8 percent, and hydrocarbon saturations from 36.2 to 62.0 percent. Potential seals or baffles found in the Wolfcamp B include nonreservoir carbonates and argillaceous rocks that make up 12.2 and 19.3 percent of the cored interval, respectively (Fig. 4.16).

The changes in lithofacies, mineral constituents, and fluid saturations impact the log signatures seen in the Wolfcamp B. Well logs from the top of the Wolfcamp B show high resistivities and porosity logs that align (NPHI ~ DPHI). The log signature at the top of the Wolfcamp B is similar to the log characteristics seen in the more carbonate-rich Wolfcamp

A. The lower two-thirds of the Wolfcamp B is characterized by high gamma ray, low resistivities with areas that show separation in the porosity curves (NPHI > DPHI). Periodic spikes of low gamma ray, high resistivity, and no porosity separation are episodic carbonate beds. The lower half of the Wolfcamp B, beyond the cored interval, shows thick sections of low resistivity and large porosity separations (NPHI >> DPHI), indicating higher clay proportions within those intervals. The degree of separation between neutron porosity and density porosity is proportionate to higher clay content from the shale effect. This suggests that the clay proportion in the lower portion of the Wolfcamp B (not cored) is likely higher in clay content than what was seen in the cored interval of the Wolfcamp B from this study. While total gamma ray is high in the Lower Wolfcamp B, the low uranium concentration from spectral gamma ray suggests that these are likely organic-lean, high clay intervals.

Wolfcamp B

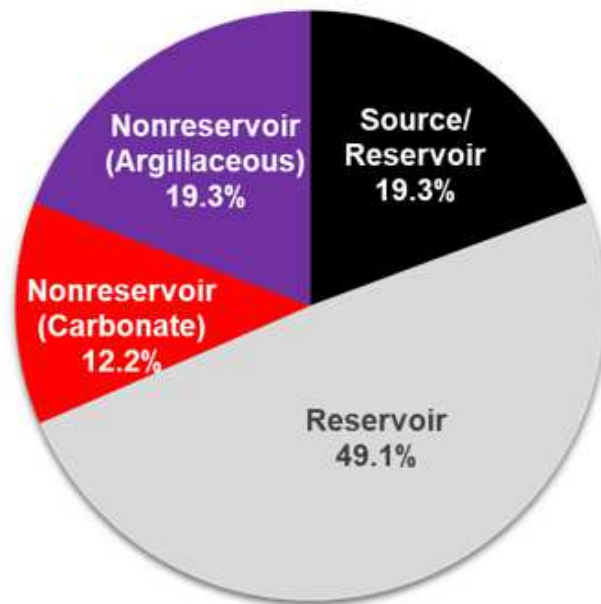


Figure 4.16—Pie chart of reservoir vs. nonreservoir prone rocks based on reservoir properties for the Wolfcamp B cored interval. The Wolfcamp B is comprised of 68.4% reservoir prone rock. Nonreservoir prone rocks encountered in the Wolfcamp B include nonreservoir (argillaceous) and nonreservoir (carbonate) rocks.

4.5.3 *Wolfcamp C*

Almost 90 percent of the Wolfcamp C was available for core analysis from this study. The Wolfcamp C is subdivided into the Upper and Lower Wolfcamp C. The Upper Wolfcamp C consists of lithofacies from the argillaceous facies group (52.5%), siliceous facies group (35.5%), calcareous facies group (10.8%), and mixed facies group (1.1%). Of the cored intervals analyzed for this study, the argillaceous mudstone is most abundant in the Upper Wolfcamp C. The Upper Wolfcamp C is characterized by low carbonate content, low overall TOCs, high porosities, low permeabilities, high water saturations, low hydrocarbon saturations, and lower rock strength. RCA data available at 10-foot increments show porosity ranging from 7.4 to 12.1 percent, with an average of 10.1 percent. Permeability ranges from 0.1 to 73.8 nD, with an average of 8.2 nD. TOC from both core and uranium concentration from logs (as a proxy for TOC), suggests a primarily organic-lean interval. Core LECO TOC ranges from 0.2 to 2.7 wt.%, with an average of 0.9 wt.%. The normal log suite of the Upper Wolfcamp C shows high total gamma ray, low uranium concentration from spectral gamma ray, low resistivities, and large porosity separation (NPHI >> DPHI).

The log signatures of the Upper Wolfcamp C are similar to log responses in the lower half of the Wolfcamp B. The Upper Wolfcamp C is comprised primarily of nonreservoir prone rock, that make up 63.3 percent of the cored interval of the Wolfcamp C (Fig. 4.17). Potential seals or baffles encountered in the Upper Wolfcamp C include nonreservoir argillaceous facies (52.5%) and nonreservoir carbonate facies (10.8%). The cored section of the Upper Wolfcamp C is comprised of 36.7 percent reservoir prone rock, which is the lowest of all of the Wolfcamp cored intervals evaluated. Factors including low spectral gamma ray uranium concentrations (SGR_u), low overall core TOC, low permeabilities, high water saturations, and the abundance of nonreservoir prone rock suggest that the Upper Wolfcamp C has overall lower reservoir quality. The similarities between log signatures of the Upper Wolfcamp C to the lower half of the Wolfcamp B indicate that the Wolfcamp B likely has poor reservoir qualities, as seen in the Upper Wolfcamp C.

The entire Lower Wolfcamp C was cored for this study, showing variations in facies distribution, reservoir properties, and log signatures compared to the Upper Wolfcamp C. The Lower Wolfcamp C consists of the siliceous facies group (53.3%), mixed facies group (22.7%), calcareous facies group (21.3%), and argillaceous facies group (2.7%). Lithofacies in the Lower Wolfcamp C include the following: carbonate-rich siliceous mudstone (27.7%), mixed calcareous silty mudstone (22.7%), siliceous mudstone (19.0%), packstone (12.2%), calcareous siltstone (8.2%), bioturbated siliceous mudstone (6.5%), argillaceous mudstone (2.7%), and wackestone (1.0%).

Reservoir properties of the Lower Wolfcamp C, show higher overall TOC, higher permeabilities, high rock strength, lower water saturation, and higher hydrocarbon saturation, compared to the Upper Wolfcamp C. LECO TOC from the Lower Wolfcamp C ranges from 1.4 to 4.0 wt.%, with an average of 2.2 wt.%. Looking at uranium concentration from the spectral gamma ray log as a proxy for organic matter content, the higher uranium concentrations that make up the total gamma ray in Lower Wolfcamp C are consistent with the higher TOCs observed from core-derived TOC. This suggests that the Lower Wolfcamp C has higher overall TOC compared to the Upper Wolfcamp C. Porosities in the Lower Wolfcamp C range from 4.9 to 10.1 percent, with an average of 8.4 percent. Permeability ranges from 4 to 240 nD, with an average of 60 nD. The Lower Wolfcamp C has higher overall rock strength compared to the Upper Wolfcamp C, due to the higher proportions of harder carbonate-dominated lithofacies. Water saturation ranges from 22.3 to 65.4 percent, with an average of 43.4 percent. Hydrocarbon saturation ranges from 34.6 to 77.7 percent, with an average of 56.6 percent. The cored interval of the Lower Wolfcamp C is comprised of 75.9 percent reservoir prone rock (Fig. 4.17). Potential seals and baffles in the Lower Wolfcamp C include both nonreservoir carbonate (21.3%) and nonreservoir argillaceous (2.7%) rocks.

Looking at the log characteristics, the Lower Wolfcamp C, shows high and low gamma ray signatures from the contrasting, interbedded calcareous and noncalcareous lithofacies. Resistivity curves are higher than the Upper Wolfcamp C and similar to those in the Wolfcamp A. Porosity curves show small to moderate separation in the top section of the Lower Wolfcamp C, attributed to a higher abundance of mudstone lithofacies from the

siliceous facies group. Porosity curves align with one another at the base as the thickness and frequency of carbonate beds increase.

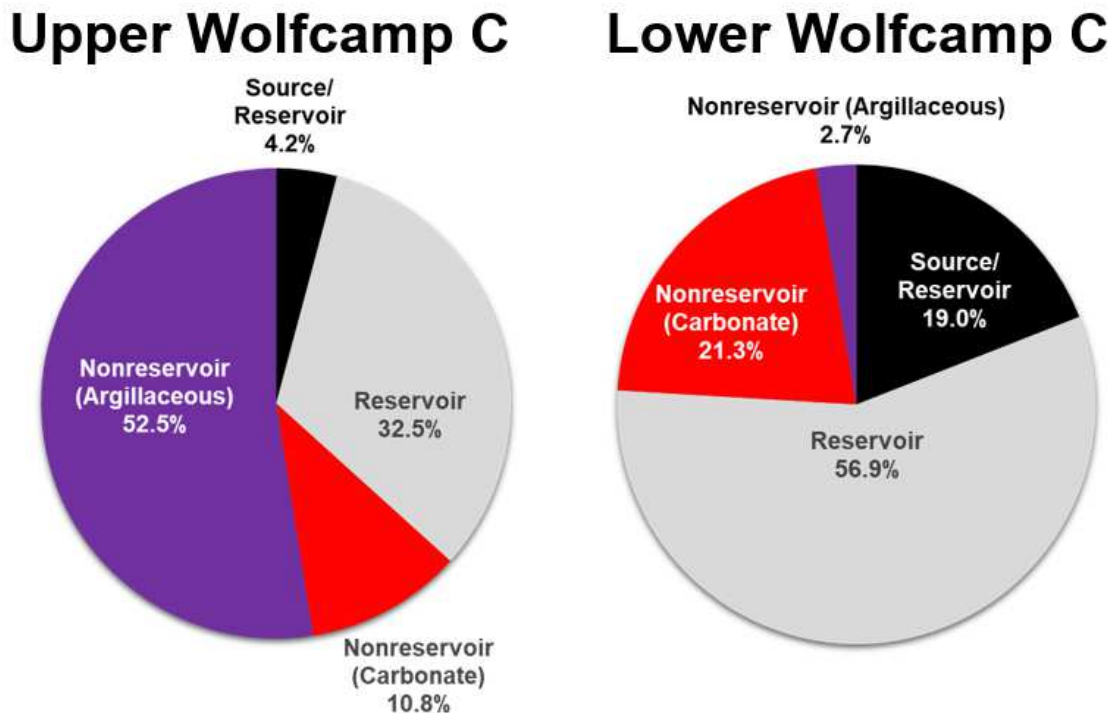


Figure 4.17—Pie charts of reservoir vs. nonreservoir prone rocks based on reservoir properties for the Upper Wolfcamp C and Lower Wolfcamp C cored interval. The Upper Wolfcamp C is composed of 36.7% reservoir prone rock. Primary nonreservoir rock in the Upper Wolfcamp C is nonreservoir (argillaceous) that makes up 52.5% of the cored interval. Nonreservoir (carbonate) rocks represent 10.8% of the interval. Reservoir potential is more favorable in the Lower Wolfcamp C. The Lower Wolfcamp C is comprised of 75.9% reservoir rock. Nonreservoir rock makes up 24% of the Lower Wolfcamp C. The primary type of nonreservoir rock in the Lower Wolfcamp C are carbonates that make up 21.3% of the Wolfcamp C.

4.5.4 Wolfcamp D

Around 40 ft of the Wolfcamp D was cored with the well log ending in Wolfcamp D. Analysis of the cored interval shows deposition of siliciclastic- and carbonate-dominated lithofacies. The cored interval is comprised of the following: argillaceous facies group (39.3%), calcareous facies group (35.1%), siliceous facies group (23.4%), and mixed facies group (2.1%). Lithofacies in the Wolfcamp D include the following: argillaceous mudstone (39.3%), wackestone (16.1%), carbonate-rich siliceous mudstone (15.4%), packstone (13.7%), siliceous mudstone (8.1%), calcareous siltstone (5.3%), and mixed calcareous silty mudstone (2.1%).

A thorough core analysis for the Wolfcamp D interval could not be completed due to the short, cored section and limited RCA samples. Reservoir properties associated with the siliciclastic-dominated, argillaceous mudstone interval show higher water saturations and lower rock strength. Within the siliciclastic interval, the carbonate lithofacies show high rock strength spikes. No RCA data was available for the carbonate-rich, basal portion of the cored section.

From the well logs, the top of the Wolfcamp D shows high gamma ray, low resistivity, and porosity separation ($\text{NPHI} > \text{DPHI}$) as a result of the argillaceous mudstone lithofacies present at the top of the interval. The rest of the Wolfcamp D interval (beyond the cored unit) shows highly interbedded low to high gamma ray, high resistivities, aligned porosity curves with small to no separations ($\text{NPHI} \sim \text{DPHI}$), and thin spikes of PEF greater than 4 b/e. These log signatures of the Wolfcamp D are similar to those observed in the Wolfcamp A (below the Y-Sand) and the Lower Wolfcamp C, in which core data was available. This suggests that the uncored portion of the Wolfcamp D likely has similar characteristics with calcareous lithofacies interbedded with mixed and siliceous lithofacies that are mudstones.

Looking at the mud log of the Wolfcamp D (below the cored section), the mud log description indicates shale and limestone cuttings. Descriptions of shale include dark gray, medium gray to black color, slightly calcareous to very calcareous, calcite inclusions, calcite-filled veins, and slightly massive, among other descriptors. Limestones were described as white, light gray cream to tan in color, slightly laminated, microcrystalline to crystalline, moderately hard, and slightly dolomitic in some sections. While core was not available for the bulk of the Wolfcamp D section, the combination of log signatures and cuttings description from mud logs suggests that the Wolfcamp D interval consists of interbedded limestone and shales.

CHAPTER 5: CONCLUSIONS AND RECOMMENDATIONS

5.1 Conclusions

1. Four facies groups and nine lithofacies were identified from 738.4 feet of core from the Wolfcamp A, B, C, and D. Facies groups were first determined based on composition. Lithofacies were subdivided from facies groups, based on core observations, including grain size, grain type, and key sedimentary structures.
2. Depositional processes examined from core show deposits of carbonate- and siliciclastic-dominated sediment gravity flows with intermittent background sedimentation. These deposits cause highly stratified, heterogeneous strata throughout the Wolfcamp Formation that contain beds often below log resolution.
3. A mineral model was used to approximate mineral components of quartz, calcite, and illite using high-resolution XRF elemental data from elements of silicon (Si), calcium (Ca), and potassium (K). The mineral model was applied to visualize and understand changes in mineralogy in the Wolfcamp intervals. The interbedded nature and high carbonate content in the Wolfcamp A were highlighted. The Wolfcamp B shows higher siliciclastic proportions.
4. A synthetic gamma ray (GRsyn) log was calculated, using XRF elemental data for thorium (Th), potassium (K), and uranium (U), to produce a high-resolution gamma ray curve. GRsyn was compared to the wireline gamma ray (GR). GRsyn captures a more realistic gamma ray curve, showing changes in gamma ray below log resolution without influences of “shoulder effects.”
5. Principal component analysis (PCA) was used to process the extensive XRF dataset (n=799) considering 41 elements. PCA was completed for the Wolfcamp A and B, to evaluate elemental relationships in each interval.
6. K-means clustering was implemented to define four chemofacies with similar elemental signatures. The Wolfcamp A primarily consists of Chemofacies 1, 2, and 3. The Wolfcamp B is comprised dominantly of Chemofacies 3 and 4.

7. Terrigenous and carbonate elemental indicators were evaluated using crossplots and elemental profiles. Terrestrial influx is highest in the lower two-thirds of the Wolfcamp B. Carbonate indicators are highest in the Wolfcamp A, particularly in elements calcium (Ca) and strontium (Sr) which are proxies for calcite.
8. Silica source was investigated using silicon (Si) versus aluminum (Al) for the Wolfcamp A and B. The Wolfcamp A shows a strong positive detrital trend ($R^2=0.80$). The Wolfcamp B shows authigenic/biogenic influences ($R^2=0.31$) on silica source.
9. Paleoredox-sensitive elements examined with core TOC, showed the strongest relationship with nickel (Ni) with R^2 of 0.79. Moderate relationships with uranium (U), copper (Cu), and molybdenum (Mo) were also observed.
10. A high abundance of paleoredox-sensitive indicators was found interbedded in both the Wolfcamp A and B. Corresponding core locations show that beds with high concentrations are associated with the siliceous mudstone lithofacies. Elevated paleoredox-sensitive indicators, phosphatic nodules, very fine grain size, and high TOC of the siliceous mudstone, independently support periods of suboxic to anoxic conditions at the time of deposition.
11. Source Rock Analysis (SRA) indicates that the Wolfcamp A through D in the Thunder C20-13 #2H well is in the condensate gas window with 1.15 to 1.36 %Ro.
12. Unconfined compressive strength (UCS), as a method to evaluate rock strength from core, was measured throughout the Wolfcamp A through D. Rock strength was seen to be a function of lithofacies. Carbonate-dominated lithofacies have higher rock strength, while clay-dominated facies have lower rock strength. The rock strength profile throughout the Wolfcamp intervals is influenced by facies distribution.
13. Mineral-based brittleness index (MBI) calculations evaluating the mineral controls on brittleness, showed that carbonate-dominated rocks are more prone to brittle behavior. Clay-dominated rocks are more inclined to ductile behavior.

14. Reservoir and fluid properties from Routine Core Analysis (RCA) were evaluated for each lithofacies to assess reservoir quality. Properties taken into consideration were total organic carbon (TOC), porosity, permeability, fluid saturations, and rock strength. Based on reservoir properties, four designations of reservoir and nonreservoir prone rocks were determined. These include the following: 1) source/reservoir, 2) reservoir, 3) nonreservoir (carbonate), and 4) nonreservoir (argillaceous).
15. Detailed core analyses (lithofacies, mineral components, and reservoir properties) were compared to the corresponding log responses. The controls of rock and fluid properties on well log responses were discussed. These were used to evaluate zones without cored intervals.
16. Reservoir prone rocks are abundant in the Wolfcamp Formation. The highest abundance of reservoir prone facies are found in the following intervals of Wolfcamp A (61%), Wolfcamp B (70%), and Lower Wolfcamp C (76%).
17. Intervals with low proportions of reservoir prone rocks include the Upper Wolfcamp C (36.7%) and Lower Wolfcamp B (not cored). High proportions of nonreservoir rock within these intervals suggest higher potential of seals or baffles.

5.2 Recommendations

1. Obtain cores, core associated data, and well logs in the nearby Reeves County region to investigate the lateral heterogeneity of the Wolfcamp Formation.
2. Collect additional XRD and RCA data for undersampled lithofacies, including the calcareous siltstone, skeletal packstone, wackestone, bioturbated siliceous mudstone, and dolostone. A more robust XRD and RCA dataset would allow more accurate characterization of composition, delineation of facies type, and analysis of reservoir properties.
3. Prepare thin section and FE-SEM samples to evaluate diagenetic features, understand pore morphology, define petrographic facies, and investigate other micro- to nano-scale effects on reservoir quality.

4. Collect additional XRF data for further elemental analysis for the Wolfcamp C and D intervals.
5. Include a more detailed analysis of geomechanical trends in the Wolfcamp. Collect laboratory rock strength measurements to compare to unconfined compressive strength (UCS) data calculated from the Equotip Bambino micro-rebound hammer. Compare UCS data to sonic scanner log elastic parameters.
6. Use integrated lithofacies distribution and geoscience parameters (water saturation, porosity, permeability, and geomechanical properties) to upscale facies into grids (i.e., 2, 5, and 10 ft) for fracture stimulation modeling in order to investigate the controls on fracture propagation and geometry (width and length).
7. Analyze petrophysical methods to predict mineralogy and fluid saturations through multimaterial analysis by utilizing matrix mineralogy data from XRD or XRF.

REFERENCES

- Adams, J.E., 1965, Stratigraphic-tectonic development of Delaware Basin, American Association of Petroleum Geologists Bulletin, v. 49, p. 2140-2148.
- Al Duhailan, M.A., Sonnenberg, S.A., Longman, M., 2015, Analyzing beef fractures: Genesis and relationship with organic-rich shale facies: Unconventional Resources Technology Conference: 2151959.
- Algeo, T.J., Lyons, T.W., 2006, Mo-total organic carbon covariation in modern anoxic marine environments: implications for analysis of paleoredox and paleohydrographic conditions: *Paleoceanography*, v. 21, p. 1-23.
- Arthur, M.A. and Dean, W.E. 1991. An holistic geochemical approach to cyclomania: examples from Cretaceous pelagic limestone sequences in Einsele, G., Ricken, W. and Seilacher, A., *Cycles and Events in Stratigraphy*: Springer Verlag Berlin, p. 126-166.
- Asquith, G., Krygowski, D., 2004, Basic well log analysis: American Association of Petroleum Geologists Methods in Exploration Series, n. 16, p. 31-81.
- Baumgardner, R.W., Hamlin, H.S., Rowe, H.D., 2016, Lithofacies of the Wolfcamp and Lower Leonard Intervals, Southern Midland Basin, Texas: Bureau of Economic Geology, Report of Investigation, no. 281, p.12.
- Baumgardner, R.W., Hamlin, H.S., Rowe, H.D., 2014, High resolution core studies of Wolfcamp/Leonard basinal facies, Southern Midland Basin, Texas: American Association of Petroleum Geologists Search and Discovery, #10607.
- Bievenour, A., 2019, Reservoir characterization of the Bone Spring and Wolfcamp Formations, Delaware Basin, Ward County, West Texas: Colorado School of Mines, p. 44-45.
- Blakey, R.C., 2019, Deep Time Maps: Greater Permian Basin Series.
- Blomquist, P.K., 2016, Wolfcamp Horizontal Play, Midland Basin, West Texas: American Association of Petroleum Geologists Pacific Section and Rocky Mountain Joint Meeting.
- Boggs, S.J., 2001, Principles of sedimentology and stratigraphy, third edition, Merrill publishing company, p. 46-55.
- Bouma, A.H., 1962, Sedimentology of some Flysch deposits: A graphic approach to facies interpretation: Elsevier, p. 168.
- Britt, L., 2012, Fracture stimulation fundamentals: *Journal of Natural Gas Science and Engineering*, p. 34-51.

- Buntoro, A., Prasetyadi, C., Wibowo, R.A., Suranto., Lukmana, A.H., 2018, Validation of shale brittleness index calculations from wireline log of well BETRO-001 by using XRD test results and uniaxial test as parameters for determining potential of shale hydrocarbon - brown shale of Pematang Group Formation, Central Sumatra Basin, Bengkalis Trough: IOP Conference Series: Earth and Environmental Science. DOI: 10.1088/1755-1315/212/1/012069.
- Candelaria, M.P., Sarg, J.F., and Wilde, G.L., 1992, Wolfcamp sequence stratigraphy of the Eastern Central Basin Platform *in* Mruk, D.H., and Curran, C., eds., Permian Basin exploration and production strategies: application of sequence stratigraphic and reservoir characterization concepts: West Texas Geological Society Publication 92-91, p. 27-44.
- Craigie, N., 2018, Principles of elemental Chemostratigraphy—A practical user guide *in* Advances in Oil and Gas Exploration and Production Series, Springer, <http://doi.org/10.1007/978-3-319-71216-1>.
- Crain, E.R., 1986, Logging tool theory: Density logs *in* Crain, E.R., The log analysis handbook: Pennwell Books, p. 24.
- Curtis, J.B., and J.E. Zumberge, 2017, An applied geochemical look at the Delaware Basin petroleum systems: Delaware Basin Playmaker's Forum, Midland, Texas, February 22, 2017, http://www.searchanddiscovery.com/abstracts/pdf/2017/90293dpa/abstracts/ndx_curtis.pdf.
- Dancy, J.R., 2018, From the Drake well to the Santa Rita #1: The history of the U.S. Permian Basin: a miracle of technology innovation: Oil and Gas, Natural Resources, and Energy Journal, v.3 p. 1183-1213.
- Dembicki, H.J., 2009, Three common source rock evaluation errors made by geologists during prospecting or play appraisals: American Association of Petroleum Geology Bulletin, v. 93, n. 3, p. 341-356.
- Driskill, B., Pickering, J., Rowe, H., 2018, Interpretation of high resolution XRF data from the Bone Spring and Upper Wolfcamp, Delaware Basin, USA: Unconventional Resources Technology Conference: 2901968, p. 1-21.
- Dunham, R.J., 1962, Classification of carbonate rocks according to depositional texture *in* Ham, W.E., Classification of carbonate rocks, American Association of Petroleum Geologists Bulletin Memoir, p. 108-121.
- Ece, O.I., 1990, Geochemistry and occurrence of authigenic phosphate nodules from the Desmoinesian cyclic Excello epeiric sea of the Midcontinent, USA: Istanbul Technical University, v. 7, p. 298-312.
- U.S. Energy Information Administration (EIA), 2018, Permian Basin: Wolfcamp Shale Play geology review: U.S. Department of Energy, p. 2-11.

- U.S. Energy Information Administration (EIA), 2021, Drilling productivity report for tight oil and shale gas regions (January 2021): U.S. Energy Information Administration, p. 9.
- Emerson, S.R., Heusted, S.S., Ocean anoxia and concentrations of molybdenum and vanadium in seawater: Elsevier Science Publishers, v. 34, p. 177-196.
- Engle, M.A., Reyes, F.R., Varonka, M.S., Orem, W.H., Ma, L., Ianno, A.J., Schell, T.M., Xu, P., Carroll, K.C., 2016, Geochemistry of formation waters from the Wolfcamp and Cline shales: Insights into brine origin, reservoir connectivity, and fluid flow in the Permian Basin, USA: *Chemical Geology*, v. 425, p. 76-92.
- Ewing, T.E., Christensen, H., 2016, Texas through time: Lone star geology, landscapes and resources: Bureau of Economic Geology Udden Series, v. 6.
- Fairhurst, B., Hanson, M.L., 2012, Evolution and Development of the Wolfbone Play, Southern Delaware Basin, West Texas: An emerging Frontier, An Oil-Rich Unconventional Resource: American Association of Petroleum Geologists Search and Discovery, #10411.
- Fielding, C.R., Frank, T.D., Isbell, J.L., 2008, The Late Paleozoic ice age—A review of current understanding and synthesis of global climate patterns *in* Fielding, C.R., Frank, T.D., Isbell, J.L., Resolving the Late Paleozoic Ice Age in time and space: Geological Society of America Special Paper, no. 441, p. 343-354.
- Gale, J., Nicot, J.P., Davari, R., Mickler, P., Eichhubl, Reedy, B., Scanlon, B., Liu, J., 2017, SUTUR2 Wolfcamp Project, Annual Report (June 2017): Bureau of Economic Geology, p. 298.
- Gamero Diaz, H., Miller, C., Lewis, R., Fuentes, C.C., 2013, Evaluating the impact of mineralogy on reservoir quality of organic shale plays: American Association of Petroleum Geologists Search and Discovery, article #41221.
- Gaswirth, S.B., French, K.L., Pitman, J.K., Marra, K.R., Mercier, T.J., Leathers-Miller, H.M., Schenk, C.J., Tennyson, M.E., Woodall, C.A., Brownfield, M.E., Finn, T.M., Le, P.A., 2018, Assessment of undiscovered continuous oil and gas resources in the Wolfcamp shale and Bone Springs Formation of the Delaware Basin, Permian Basin province, New Mexico and Texas: U.S. Geological Survey Fact Sheet 2018-3073.
- Glover, P., 2000, The sonic of acoustic log: University of Leeds, ch. 16, p. 172-197.
- Gupta, I., Rai, C., Sondergeld, C., & Devegowda, D., 2017, Rock typing in Wolfcamp Formation, Society of Petrophysicists and Well-Log Analysts: https://www.onepetro.org/conference-paper/SPWLA-2017-D?sort=&start=0&q=total+organic+carbon+wolfcamp+&from_year=&peer_reviewed=&published_betw_eeen=&fromSearchResults=true&to_year=&rows=25#.
- Handford, C.R., 1981, Sedimentology and genetic stratigraphy of Dean and Spraberry formations (Permian), Midland Basin, Texas, American Association of Petroleum Geologists Bulletin, v. 65, p. 1602-1616.

- Handford, C.R., Loucks, R.G., 1993, Carbonate depositional sequences and systems tracts—responses of carbonate platform to relative sea-level changes *in* Loucks, R.G., Sarg, J.F., Carbonate sequence stratigraphy: Recent developments and applications: American Association of Petroleum Geologists Memoir 57, p. 3-41.
- Hartmann, D.J., Beaumont, E.A., 1991, Predicting reservoir system quality and performance *in* Beaumont, E.A., Foster., N.H., Treatise of petroleum geology/handbook of petroleum geology, ch. 9, p. 9-49.
- Haughton, P., Davis, C., McCaffrey, W., Barker, S., 2009, Hybrid sediment gravity flow deposits—Classification, origin and significance: *Marine and Petroleum Geology*, v. 26, p. 1900-1918.
- Heckel, P.H., 1986, Sea-level curve for Pennsylvanian eustatic marine transgressive-regressive depositional cycles along midcontinent outcrop belt, North America: *Geological Society of America*, v. 14, p. 330-334.
- Hennenfent, G., Hegmann, M., Harris, C., Schwartz, K., 2015, From core analysis to log-based pay identification in the Delaware Basin Wolfcamp Formation: *Society of Exploration Geophysicists and American Association of Petroleum Geologists Interpretations*, v. 3, no. 3 (August 2015), p. SV35-SV44.
- Hill, C., 2006, Geology of the Delaware Basin Guadalupe, Apache, and Glass Mountains New Mexico and West Texas: *Society for Sedimentary Geology Permian Basin Section*, no. 96-39, p. 32-48.
- Hills, J.M., 1963, Late Paleozoic tectonics and mountain ranges, western Texas to southern Colorado: *American Association of Petroleum Geologists Bulletin*, v. 27, no. 9, p. 1709-1725.
- Hill, R.J., D.M. Jarvie, B.L. Claxton, J.D. Burgess, and J.A. Williams, 2003, An Investigation of Petroleum Systems of the Permian Basin, USA: 21st IMOG Meeting, Krakow, Poland September 8-12, 2003.
- Hills, J.M., 1984, Sedimentation, tectonism, and hydrocarbon generation in Delaware Basin, West Texas and Southeastern New Mexico: *American Association of Petroleum Geology Bulletin*, v. 69, no.3, p. 250-267.
- Hobson, J.P., Caldwell, C.D., Toomey, D.F., 1985a, Early Permian deep-water allochthonous limestone facies and reservoirs, west Texas: *American Association of Petroleum Geologists Bulletin*, v. 69, p. 2130-2147.
- Hobson, J.P., Caldwell, C.D., Toomey, D.F., 1985b, Sedimentary facies and biota of Early Permian deep-water allochthonous limestone, southwest Reagan County, Texas *in* Crevello, P.D., Harris, P.M., Deep-water carbonates: Buildups, Turbidites, Debris Flows and Chalks, Core Workshop Notes 6: *Society of Economic Paleontologists and Mineralogists*, Tulsa, p. 56-92.

- Horak, R.L., 1985, Tectonic and hydrocarbon maturation history in the Permian Basin: Oil and Gas Journal, v. 83, no. 21, p. 124-129.
- Jacobs, T., 2013, Cracking the cline: A new shale play develops in the Permian Basin: Journal of Petroleum Technology, v. 65, no. 11, p. 70-77.
- Jacobson, S.R., 1991. Petroleum Source Rocks and Organic Facies: Chapter 1: Petroleum Generation and Migration *in* Source and Migration Processes and Evaluation Techniques, American Association of Petroleum Geologists Special Volumes, p. 3-11.
- Jarvie, D.M., J.D. Burgess, A. Morelos, R.K. Olson, P.A. Mariotti, and R. Lindsey, 2001, Permian Basin Petroleum Systems Investigations: Inferences from Oil Geochemistry and Source Rocks: American Association of Petroleum Geologists Bulletin, v. 85, p. 1693-1694.
- Jarvie, D.M., Prose, D., Jarvie, B.M., Drozd, R., Maende, A., 2017, Conventional and unconventional petroleum systems of the Delaware Basin: American Association of Petroleum Geology Annual Convention and Exhibition.
- Kang, Y.S., Shang, C.J., Zhou, H., Huang, Y., Zhao, Q., Deng, Z., Wang, H.Y., Ma, Y.Z., Ma, Y.Z., 2020, Mineralogical brittleness index as a function of weighting brittle minerals— from laboratory tests to case study: Journal of Natural Gas Science and Engineering, v. 77.
- Katz, A., Sass, E., Holland, H.D., Starinsky A., 1972, Strontium behavior in the aragonite-calcite transformation: An experimental study at 40-98 degC: Geomechemica et Cosmochemica Acta, v. 36, no. 4.
- Kidder, D.L., 1985, Petrology and origin of phosphate nodules from the Midcontinent Pennsylvanian epicontinental sea: Journal of Sedimentary Research, v.55, no. 6, p. 809-816.
- Kvale, E.P., Rahman, M.W., 2016, Depositional facies and organic content of Upper Wolfcamp Formation (Permian) Delaware Basin and implications for sequence stratigraphy and hydrocarbon source: Unconventional Resources Technology Conference: 2457495.
- Kvale, E.P., Bowie, C.M., Flentrophe, C., Mace, C., Parrish, J.M., Price, B., Anderson, S., DiMichele, W.A., 2020, Facies variability within a mixed carbonate-siliciclastic sea-floor fan (upper Wolfcamp Formation, Permian, Delaware Basin, New Mexico: AAPG Bulletin, v. 104, no. 3, p. 525-563, doi: 10.1306/06121917225.
- Larmier, S., Zanella, A., Lejay, A., Mourgues, R., Gelin, F., 2018, Distribution of natural hydraulic fractures (beef veins) within the Vaca Muerta Formation, Neuquen Basin, Argentina: American Association of Petroleum Geologists Annual Convention and Exhibition, Utah, May 20-13, 2018.
- Law, C.A., 1999, Evaluating source rocks *in* Foster, N.H., Beaumont E.A., Handbook of petroleum geology: Exploring for oil and gas traps: American Association of Petroleum Geology, ch. 6, pg. 6-41.

- Lazar, O.R., Bohacs, K.M., Macquaker, J.H.S., Schieber, J, Demko, T.M., 2015, Capturing key attributes of fine-grained sedimentary rocks in outcrops, cores, and thin sections: Nomenclature and description guidelines: *Journal of Sedimentary Research*, v. 85, p. 230-246.
- Loucks, R., 2005, Review of the Lower Ordovician Ellenburger Group of the Permian Basin, West Texas: Bureau of Economic Geology.
- Loucks, R.G., Brown, A.A., Achauer, C.W., Budd, D.A., 1985, Carbonate gravity-flow sedimentation on low angle slopes off the Wolfcampian northwest shelf of the Delaware Basin: *Society of Sedimentary Geologists*, no. 6, p. 56-92.
- Lowe, D.R., 1982, Sediment gravity flows: II depositional models with special reference to the deposits of high-density turbidity currents: *Journal of Sedimentary Petrology*, v. 52, p. 279-297.
- Ma, C.F., Dong, C.M., Luan, G.Q., Lin, C.Y., Liu, X.C., Elsworth, D., 2016; Types, characteristics and effects of natural fluid pressure fractures in shale: A case study of the Paleogene strata in Eastern China: *Petroleum Exploration and Development*, v.43, p. 634-643.
- Masoudi, P., Memarian, H., Aifa, T., Tokhmechi, B., 2017, Geometric modeling of the volume of investigation of well logs for thin-bed characterization: *Journal of geophysics and engineering*, v. 14, p. 426-444.
- Matchus, E.J., Jones, T.S., 1984, East-west cross section through Permian Basin of West Texas: West Texas Geological Society.
- Mathia, E., Ratcliffe, K., Wright, M., 2016, Brittleness index - A parameter to embrace or avoid: Unconventional Resources Technology Conference, San Antonio, TX. DOI:10.15530/URTEC-2016-2448745.
- Mazzullo, S.J., Reid, A.M., 1989, Lower Permian platform and basin depositional systems, norther Midland Basin, Texas *in* Crevello, P.D., Wilson, J.J., Sarg, J.F., Read, J.F., Controls on carbonate platform and basin development: *SEPM Special Publication*, no. 44, p. 305-320.
- McGlue, M.M., Baldwin, P.W., 2015, Preliminary geologic and chemostratigraphic analysis of the Wolfcamp D Shale, Midland Basin, West Texas: Unconventional Resources Technology Conference: 2172122.
- Meissner, F.F., 1972, Cyclic sedimentation in the Middle Permian strata of the Permian Basin *in* Elam, S.G., Chuber, S., Cyclic sedimentation in the Permian Basin, 2nd ed, West Texas Geological Society, p. 203-232.
- Middleton, G.V., Hampton, M.A., 1973. Sediment gravity flows: mechanics of flow and deposition *in* Middleton, G.V., Bouma, A.H. (Co-Chairmen), Turbidites and deep-water sedimentation: *Societ of Economic Paleontologists and Mineralogists*, p. 1-38.

- Michael, N.A., Craigie, N.W., 2021, Application of principal component analysis on chemical data for reservoir correlation: A case study from Cretaceous carbonate sedimentary rocks, Saudi Arabia: American Association of Petroleum Geology Bulletin, v. 105, no. 4, p. 785-807.
- Morgan, W.A., Clopine, W.W., Kokkoros, G.F., Wiley, G.H., 1996, Sequence stratigraphic framework and exploration potential of lower Permian (Wolfcampian) gravity-flow deposits, eastern Midland Basin, Texas: AAPG-SEPM Annual Meeting, v. 5., p. 101.
- Murray, C.D., 2015, Mechanical stratigraphy and sonic log relationships using the Proceq Bambino in the Niobrara Formation, Denver Basin: Colorado School of Mines.
- Murphy, R.J., 2015, Depositional systems interpretation of early Permian mixed siliciclastics and carbonates, Midland Basin, Texas, Theses and Dissertations—Geological Sciences, p. 99, <https://scholarworks.iu.edu/dspace/handle/2022/19695>.
- Nance, H.S., Rowe, H., 2015, Eustatic controls on stratigraphy, chemostratigraphy, and water mass evolution preserved in a Lower Permian mudrock succession, Delaware Basin, West Texas, USA, Interpretation, v. 3, no. 1., p. SH11-SH25.
- Nesse, W.D., 2014, Introduction to optical mineralogy: Oxford University Press, eds. 4, p. 263, 267, 311, 316.
- Perlman, Z.S., 2017, Stratigraphic, geochemical, and geochronological analysis of the Wolfcamp-D interval, Midland Basin, Texas: University of Kentucky, p. 39-67.
- Peters, K.E., Xia, X., Pomerantz, A.E., Mullins, O.C., 2016, Geochemistry applied to evaluation of unconventional resources *in* Ma, Y.Z., Holditch, S.A., Unconventional oil and gas resources handbook: Gulf Professional Publishing, p. 71-126.
- Peter, K.E., Cassa, M.R., 1994, Applied source-rock geochemistry *in* Magoon, L.B., Dow, W.G., The petroleum system: From source to trap: American Association of Petroleum Geologists, p. 93-120.
- Playton, T., Kerans, C., 2002, Slope and toe of slope deposits shed from a late Wolfcampian tectonically active carbonate ramp margin: Gulf Coast Association of Geological Society Transactions, v. 52, p. 811-820.
- Ramirez, K.M., Cuba, P.H., Miskimins, J.L., Anderson, D.S., Carr, M.M., 2012, Integrating geology, hydraulic fracturing modeling, and reservoir simulation: Society of Petroleum Engineers, SPE-151931, p. 1-5.
- Rider, M., Kennedy, M., 2011, The geological interpretation of well logs, third edition: Scotland, Rider-French Consulting Limited, p. 432.
- Robinson, K., 1988, Petroleum geology and hydrocarbon plays of the Permian Basin petroleum province West Texas and Southeast New Mexico, U.S. Geological Survey Open-File Report 88-450-Z, 53, p. 1-51 <https://doi.org/10.3133/ofr88450Z>.

- Ross, C.A. 1963. Standard Wolfcampian Series (Permian), Glass Mountains, Texas. Geological Society of America, v. 88. doi: 10.1130/MEM88.
- Ross, C.A., Ross, J.R., 1987, Late Paleozoic sea levels and depositional sequences: Cushman Foundation for Foraminiferal Research, Special Publication, v. 24, p. 137-149.
- Ross, C.A., Ross, J.R., 1997, Nealian and Lenoxian (Wolfcampian Lower Permian) Depositional Sequences, Fusulinid Facies and Biostratigraphy, Glass Mountains, Texas: Western Washington University Geology Faculty Publications, v. 64, p. 125-128.
- Ruppel, S.C., 2001, Stratal architecture and facies development a Middle Wolfcampian Platform Carbonate Reservoir: University Block 9 Field, Andrews County, Texas: Applications for Wolfcampian Exploration and Development, Permian Basin SEPM Field Trip and Core Workshop, p. 1-23.
- Ruppel, S.C., Ward, W.B., 2013, Outcrop-based characterization of the Leonardian carbonate platform in West Texas: Implications for sequence-stratigraphic styles in the Lower Permian: AAPG Bulletin, v. 97, no. 2, p. 226.
- Sageman, B.B., Lyons, T.W., 2009, Geochemistry of fine-grained sediments and sedimentary rocks *in* Holland, H.D., Turekian, K.K., Readings from the treatise on geochemistry: Elsevier, p. 115-158.
- Salem, A., Solum, J., Naruk, S., Minisini, D., Desjardins, P., Hnat, J., 2018, Integration of core fracture and lithofacies descriptions in the Wolfcamp Shale: Implications for mechanical stratigraphy and production: Unconventional Resources Technology Conference: 2889846, p. 1-10.
- Schenk, C.J., Pollastro, R.M., Cook, T.A., Pawlewicz, M.J., Klett, T.R., Charpentier, R.R., Cook, H.E., 2007, Assessment of undiscovered oil and gas resources of the Permian Basin province of west Texas and southeast New Mexico: U.S. Geological Survey Fact Sheet 2007-3115.
- Schlumberger Oilfield Glossary, <https://www.glossary.oilfield.slb.com/en/terms/u/unconfinedcompressivestrength.aspx>. Access date: July 14, 2020.
- Seilacher, A., 1977, Chapter 11 Evolution of Trace Fossil Communities: Developments in Palaeontology and Stratigraphy, v. 5, p. 359–376.
- Selley, R.C., Sonnenberg, S.A., 2015. Generation and migration of petroleum *in* Elements of Petroleum Geology: San Diego, Elsevier, p. 208-209.
- Shumaker, R.C., 1992, Paleozoic structure of the Central Basin Uplift and adjacent Delaware Basin, West Texas: American Association of Petroleum Geologists Bulletin, v. 76, no 12, p. 1804-1824.
- Sieminski, A., 2014, Implications of the U.S. Shale Revolution: U.S. Energy Information Administration, US-Canada Energy Summit, October 17, 2014.

- Silver, B.A., Todd, R.G., 1969, Permian cyclic strata, northern Midland and Delaware basins, West Texas and southeastern New Mexico: *American Association of Petroleum Geologists Bulletin*, v. 53, no. 11, p. 2223-2251.
- Silvis, D., 2001, Examples of Wolfcampian debris flow deposits from the Eastern Shelf of the Midland Basin, Glasscock County, Texas *in* Stoudt, E.L., Silvis, D.J., Wolfcampian of West Texas (Permian Basin, Sierra Diablo and Hueco Mountains) shelfal and periplatform carbonate reservoirs and outcrop analogs: SEPM Publication 2001.
- Sinclair, T.D., 2007, The generation and continued existence of overpressure in the Delaware Basin, Texas: Ph.D. dissertation, Durham University, Durham, England.
- Sonnenfeld, M., Ohlson, C., Zahm, C., Odegard, M., 2015, The impact of multiple, thin bentonites on proppant placement and effective fracture continuity within the Niobrara Formation, Weld County, Colorado: Unconventional Resources Technology Conference, p. 1-8, DOI: 10.15530/urtec-2015-2171548.
- Tabor, N.J., Montanez, I.P., Scotese, C.R., Poulsen, C.J., Mack, G.H., 2008, Paleosol archives of environmental and climatic history in paleotropical western Pangea during the latest Pennsylvanian through Early Permian *in* Fielding, C.R., Frank, T.C., and Isbell, J.L., Resolving the Late Paleozoic ice age in time and space: *The Geological Society of America Special Paper* 441, p. 291-303.
- Tarka Resources, 2020, Permian Basin Oil Exploration and Operations, <http://tarka.com/permian-basin/>
- Talling, P.J., Masson, D.G., Sumner, E.J., Magesini, G., 2012, Subaqueous sediment density flow: Depositional processes and deposit types: *Sedimentology*, V.59, p. 1937-2003.
- Thompson, M.L., 1954, American Wolfcampian Fusulinids: *University of Kansas Paleontological Contributions*, Article 14, Protozoa 5: The Paleontological Institute, University of Kansas, Lawrence, p. 225.
- Thompson, M., Desjardins, P., Pickering, J., Driskill, B., 2018, An integrated view of the petrology, sedimentology and sequence stratigraphy of the Wolfcamp Formation, Delaware Basin, Texas: Unconventional Resources Technology Conference: 2901513.
- Tissot, B.P., 1997. The application of the results of organic chemical studies in oil and gas exploration *in* Hobson, G.D., *Developments in Petroleum Geology*: London, Applied Science Publishers, v. 1, p. 53-82.
- Udden, J.A., Baker, C.L., Bose, E., 1916, Review of the geology of Texas: *University of Texas Bulletin*, no. 44, p. 164.
- Van Sieten, D.C., 1958, Depositional topography—examples and theory: *American Association of Petroleum Geologists Bulletin*, p. 1897-1913.

- Waite, L., Lindner, P., Sinclair, S., Damman, A., 2019, Lithostratigraphic framework of the Wolfcamp and Spraberry of the Midland Basin, A: American Association of Petroleum Geologists Southwest Section Annual Convention, Dallas, Texas, p. 1.
- Ward, Z.D., 2013, Depositional processes and environments in Wolfcampian-Leonardian strata, southern Midland Basin, Texas: Master's thesis, Oklahoma State University, Stillwater, Oklahoma.
- Wahlman, G.P., Tasker, D.R., 2013, Lower Permian (Wolfcampian) carbonate shelf-margin and slope facies, Central Basin Platform and Hueco Mountains, Permian Basin, West Texas, USA, *in* Verwer, K., Playton, T.E., Harris, P.M., Deposits, architecture and controls of carbonate margin, slope and basinal settings: SEPM Special Publication No. 13, p. 305-333.
- Wignall, P.B., Newton, R., 1998, Pyrite framboid diameter as a measure of oxygen deficiency in ancient mudrocks: *American Journal of Science*, v. 26, p. 537.
- Wilde, G.L., 1990, Practical fusulinid zonation: the species concept with Permian Basin emphasis: *West Texas Geological Society Bulletin*, v. 29, n. 7, p. 5-33.
- Yang, K.M., Dorobek, S., 1995, The Permian Basin of West Texas and New Mexico: Tectonic history of a composite foreland basin and its effects on stratigraphic development Mexico *in* Stratigraphic evolution of foreland basins: Society of Sedimentary Geology Special Publication No. 52, p. 149-174.
- Zahm, C.K., Enderlin, M., 2010 Characterization of rock strength in Cretaceous strata along the Stuart City trend, Texas: *Gulf Coast Association of Geological Societies*, v. 60, p. 693-702.
- Zahm, C.K., Sonnenfeld, M., Foorester, J., Odegard, M., 2014, High-resolution rock property variability within the Niobrara: comparison between Equotip, Scratch Index and logs.
- Zhang, H.M., 2011, Building materials in civil engineering: Woodhead Publishing.
- Zoback, M.D., 2007, Reservoir geomechanics: Cambridge University Press. ISBN 978-0-521-77069-9.

APPENDIX

Permission statement “AAPG Fair Use Rule” provided in a supplemental file to the publisher that allows the use of a single figure from an AAPG publication. AAPG Fair Use applied to Figure 2.13.